Universitat Autònoma de Barcelona

Thermal transport and thermoelectricity in organic and inorganic thin films

Gustavo Gonçalves Dalkiranis Pereira

Universitat Autònoma de Barcelona

Thermal transport and thermoelectricity in organic and inorganic thin films

Gustavo Gonçalves Dalkiranis Pereira

Universitat Autònoma
de Barcelona

Thermal transport and thermoelectricity in organic and inorganic thin films

Doctoral Thesis submitted by

Gustavo Gonçalves Dalkiranis Pereira

To apply for the degree of Doctor in Physics

Supervised by

Prof. Javier Rodríguez Viejo

Dr. Aitor Lopeandia Fernández

Nanomaterials and Microsystems Group

Physics Department

June 2019

El Prof. Javier Rodríguez Viejo, catedràtic d'universitat numerari del Departament de Física de la Facultat de Ciències de la Universitat Autònoma de Barcelona i el Dr. Aitor Lopeandía Fernández, professor agregat interí del Departament de Física de la Facultat de Ciències de la Universitat Autònoma de Barcelona,

CERTIFIQUEN que en Gustavo Gonçalves Dalkiranis Pereira ha realitzat sota la direcció d'ambdós el treball que porta com a títol *Thermal transport and thermoelectricity in organic and inorganic thin films* el qual recull en aquesta memòria per tal d'optar al Títol de Doctor en Física per la Universitat Autònoma de Barcelona.

Prof. Javier Rodríguez Viejo

Bellaterra, Juny 2019

Dr. Aitor Lopeandía Fernández

Bellaterra, Juny 2019

"Porque na muita sabedoria há muito enfado;
e quem aumenta ciência aumenta tristeza"
Ec 1:18

Agradecimientos

Gostaria de agradecer primeiramente ao meu Senhor e salvador, a quem todos os dias restaura meu ser. Por todos as orações e súplicas escutadas durante todos os anos da minha vida, seja com sins ou nãos, tenho a certeza do caminho que o Senhor me faz trilhar, não o que eu quero, mas o que Senhor tem para mim. Ao Senhor seja toda a honra e glória para todo o sempre.

Me gustaría agradecer muchísimo a Javier Rodríguez Viejo, que me haya dado la oportunidad de desarrollar este trabajo. Por su excelente trato desde el primero contacto cuando yo estaba todavía en Brasil. Por siempre exigir el mejor trabajo, sin dejar de ser amable en su trato. Por comprender todas mis debilidades y por todo el empeño para que este trabajo pudiese ser finalizado. A Aitor Lopeandia por todas sus enseñanzas durante estos años. Por los muchos sistemas desarrollados con sus ideas, que me hicieron aprender un motón. Por las discusiones y construcciones para la mejora del trabajo. A Llibertat Abad, por contribuir con el trabajo de manera tan efectiva, por la agilidad en resolver todos los problemas, por los *Runs* y por la colaboración. A todos del GNaM que de alguna manera han participado de este trabajo, sea animándome, o ayudándome con el trabajo. A la coreana Ana Vila por las bromas, risas y todos los dramas de la física experimental. A Antonio Pablo Pérez por compartir su arsenal de chistes y refranes. A Cristian Rodríguez, el polaco belga catalán más complicado de comprender en todos los sentidos, por las graciosas peleas jejeje “la culpa no es mía tampoco de Cristian” Dziękuję Ci. A Claudia Grimal por los buenos momentos compartidos y también los malos, aún recuerdo el factor 2. A Ivan Álvarez por el buen tiempo compartido. A Joan Ràfols moltes gràcies per tots els ànims que has enviat i per les teves ajudes sempre molt importants. A Pablo Ferrando, sabes como has contribuido para que este trabajo fuese el mejor posible, muchísimas gracias por compartir tus conocimientos, por las correcciones y por la amistad. A Marta González por todos los consejos y ánimos sin los cuales yo no hubiera llegado hasta aquí “eres la mejor”. A Marta Rodríguez, “la Júnior”, por las risas y conversaciones que hacen el ambiente del lab sea muy bueno. A Michele Pigliapochi por su disponibilidad en ayudarme siempre que lo necesité y por los buenos momentos compartidos. A Noa Varela, por el proyecto cafetera que ha sido muy importante para el trabajo y también por los turrones. A Julio César Martínez con quien pude compartir un poco de mi pasión por futbol y sin dudas por los cargamentos de chocolates. A Tony

Pardo por las incontables horas compartidas en la sala blanca. A Gemma Garcia por las cenas, comidas y bares que siempre fueron momentos muy agradables.

A Francesc Pi por hacer los experimentos realizados en su laboratorio.

A Alejandro Goñi por la colaboración en las medidas, por ayudarme en todo lo que necesité.

A Sebastián Reparaz por los comentarios e ideas que contribuyeron para la mejora del trabajo.

A todos del departamento de Física. A Dori Pacho por toda la eficiencia y el buen humor mientras trabajas. A todos los de la secretaria por su disponibilidad. A Francesc Poblet por todos los documentos y dudas resueltas. A los técnicos que siempre ayudaron en todo lo que necesité, Ernesto, Jordi, Rafa, Manel y Ramón.

Ao Grupo de Espectroscopia de Materiais por contribuírem em minha formação durante a graduação e mestrado.

Ao Conselho Nacional de Desenvolvimento Científico e Tecnológico (CNPq-Brasil) pela bolsa de estudos do Programa Ciência sem Fronteiras que permitiu que esse trabalho fosse realizado.

Aos amigos que compartiram momentos durante essa jornada. A Murilo e Nathália por estarem conosco desde o aeroporto até o final da jornada, e por nossas despedidas de até logo. À Mariana pela generosa amizade. A la Iglesia Bautista de Cerdanyola que con amor nos acogió. Em especial aos brasileiros, Leo e Tainã, Rô, Dani e Evinha, Sérgio e Vivi, Lídia, Sheila e Arthur pelos momentos bons compartilhados. À Deise, Edu e Juju pela recente e boa amizade.

Às amizades mantidas apesar de toda distância. A Fernando Rodrigues e Matheus Paiva pelas conversas frequentes que dão ânimo ao dia a dia. Ao Cosme e Daniel, Mah e André, Macedo e Carol, e Miguelzinho, compartilhamos alegrias, dores e tudo mais, até jantares, muito obrigado pela verdadeira amizade.

À minha segunda família. A Sérgio e Cida, por enfrentarem longas viagens para nos ver e por serem apoio durante esse tempo. A Lígia, Claudinho e Filipinho por encararem o frio e por todo carinho em forma de Havaianas.

Aos meus pais, Alcides e Marta que fizeram o possível e impossível para que eu concluísse todas as etapas, por serem um exemplo inigualável em minha vida. Ao meu irmão Vinícius e minha cunhada Priscila, pelas conversas de domingo que trazem alegria ao coração. A Marcos por seu amor mais puro e simples, o titio te ama. À Cecília, o melhor presente que poderia receber esse ano.

Em especial à minha princesa Bruna, que comprou meu sonho para um destino incerto. Por todos os sacrifícios feitos para que eu pudesse chegar a esse objetivo, sei que são incontáveis. Por todo amor demonstrado diariamente em cada detalhe do dia a dia. Por todo “força guerreiro”, “vai ficar tudo bem”, “vamos amor, falta pouco” que me fortaleceram para chegar até aqui. Sem você nada disso seria possível, te amo.

A todos que de alguma maneira contribuíram durante essa jornada muito obrigado/moltes gràcies/muchas gracias.

Thesis Contents

Dedicada a
minha esposa
Bruna Romero

1. Thesis summary

The increase in energy consumption worldwide has not been complemented by the development of clean energy sources, hindering the adoption of effective measures to mitigate the adverse effects of global warming and the degradation of air quality [1]. The rise of power consumption in the Communication and Information Technologies, ICT, is no exception. However, considering that near 60% of the total energy is lost in the form of waste heat during combustion or equivalent processes, it would be possible to adopt energy harvesting strategies, based on waste heat recovery and improved thermal management, to achieve a more rational use of energy [2]. This solution could benefit a large number of potential applications in the areas of sensing and intelligent monitoring for medical, biomedical or energy efficiency and related applications. Thermoelectric (TE) materials can convert heat into electric energy, opening the possibility to recover this lost energy in an efficient way. The main drawback for the widespread commercialization of TE-based devices for generation and/or sensing comes from their low conversion efficiency that makes this technology not competitive with other alternative energy sources such as solar cells and fuel cells. The efficiency of a TE material is related to the figure of merit, ZT, defined as the ratio of three physical quantities that account for the transport of electrons and phonons, the carriers of electricity and heat respectively. Since $ZT = (\frac{\sigma \cdot S^2}{k} \cdot T)$ the goal is to decrease the thermal conductivity while simultaneously increasing the Seebeck coefficient (S) and/or the electrical conductivity (σ) to achieve high values of ZT in the adequate temperature range.

In this context, the aim of this thesis is twofold. In a first part, this work is devoted to find and characterize efficient thermoelectric organic and inorganic materials with a good potential for energy harvesting applications. Thereunto, characterization techniques previously implemented in our group as well as new techniques are used. Also, one of these materials is used in a prototype thermoelectric generator. On the second part, a Si-membrane-based microthermoelectric generator (μTEG) is evaluated as photosensor. These measurements show an unexpected enhancement of the Seebeck coefficient produced through the interaction with light. To better evaluate this photothermoelectric effect, a new device is designed, microfabricated, tested and characterized.

This thesis is divided into following chapters:

- In Chapter 2 the theoretical framework required to understand the experimental results of chapters 4-6 is presented. Heat transport is discussed using the Classical Irreversible Thermodynamics framework. Also, the Boltzmann Transport Equation is applied to phonons and electrons in order to derivate the thermoelectric effects. Moreover, the Seebeck coefficient, the electrical and the thermal conductivities are shown in the context of thermoelectricity showing the possibilities to improve the Figure of Merit. In the last part, photothermoelectricity is described and a general discussion about the effects caused by photocarriers in the thermoelectric properties is discussed.
- In Chapter 3 the main experimental techniques used in this thesis in relation to the thermoelectric properties are shown. The principle of 3ω-Völklein method for measuring the in-plane thermal conductivity of thin films is explained, as well as the sensor shape and the electronic setup required to perform highly precise measurements. To determine the Seebeck coefficient and electrical conductivity, a homemade system and device are built. The electronic setup and vacuum system used in this work are also described in this chapter.
- The photothermoelectric effect in Si thin films is studied in Chapter 4. The photoresponse of a Si-based membrane μTEG is evaluated. The high thermal insulation and low thermal mass achieved through the reduction of the Si thickness leads to a quick and efficient response of the sensor. During these measurements, an unexpected photothermoelectric effect that leads to an enhancement of the thermopower is evidenced. In order to better understand this effect, a new device is designed and microfabricated. The photothermoelectric measurements present an improvement of the Seebeck coefficient caused by the photocarriers, suggesting that photoexcited states can be used to improve the Figure of Merit of doped Si very thin films and opening a new line of future research.
- In Chapter 5 MgAgSb films containing a small amount of Ni are grown using the sputtering technique. Morphological, structural and thermoelectric characterization of the MgAgNiSb films are performed. Finally, a prototype of a planar thermoelectric generator based on *p*-type material is designed, microfabricated and characterized.

- In Chapter 6 we verify the applicability of the 3ω-Völklein technique to determine the in-plane thermal conductivity of polymeric thin films. The in-plane thermal conductivity obtained for reference samples are in good concordance with previous literature works. Moreover, a full thermoelectric characterization of PEDOT:PSS thin films doped with DMSO in several concentration is performed, showing the capability to obtain the true *ZT* value in the in-plane direction. The results show that in thin films, the lattice component of the in-plane thermal conductivity does not obey a linear behavior in function of the DMSO concentration as reported previously for thicker samples.
- In the last chapter we present the general conclusion about the results obtained in this PhD thesis.

2. Introduction

2.1 Heat Transport Theory

Classical Irreversible Thermodynamics (CIT) provides the theoretical framework to explain most of the transport phenomena in nature. Although transport by definition requires non-equilibrium situation in many of the processes the phenomenology observed can be approximated by local equilibrium scenarios at the different points of the system out of the equilibrium. Of course, this is only true when driven forces (electric fields, temperature gradients) are moderated. Nevertheless, phenomena like ballistic transport, second sound of He or the evolution of the system under high heating rates (high fluxes) requires a more complex theoretical framework like that proposed by the extended irreversible thermodynamics. In this thesis, we mainly used the CIT to describe the phenomena studied. In that framework, we will show how the Boltzmann Transport Equation can be solved under the relaxation time approximation (RTA) to describe the thermodynamic evolution of a system out of equilibrium. Applying such a solution for electrons and phonons we will calculate the transport properties of materials and the thermoelectrical derivate properties.

2.1.1 Heat equation

We start the discussion considering the general energy balance equation of a system with an internal energy u, constant density ρ, which can be written as:

$$\rho \frac{\partial u}{\partial t} + \nabla \boldsymbol{q} = q_i \tag{2.1}$$

being $\boldsymbol{q}$ the heat flux per unit area and q_i the heat power generated internally per unit volume. The internal energy can be defined as a function of the heat capacity c_P, thus:

$$\left(\frac{\partial u}{\partial T}\right)_{p=cte} = c_P \tag{2.2}$$

and considering local equilibrium criteria the heat flux can be assumed by the Fourier law:

$$\boldsymbol{q} = -k\nabla T \tag{2.3}$$

where *k* is the thermal conductivity, an intrinsic property of a material.

Combining equations 2.1, 2.2 and 2.3, and considering the thermal conductivity isotropic and homogeneous in the medium, the following equation is obtained:

$$\rho c \frac{\partial T}{\partial t} - k\nabla^2 T = q_i \tag{2.4}$$

Equation 2.4 is usually known as the heat equation and describes the heat transported through a system when a temperature gradient is applied. This equation can be used to obtain the behavior of a solid connected to a thermal bath at temperature T_0 through a thermal conductance G, as presented in Figure 2.1. If the heat equation is integrated over the volume *V* of the solid:

$$\int_V \rho c \frac{\partial T}{\partial t} dV - \int_V k\nabla^2 T dV = \int_V q_i dV \tag{2.5}$$

And using Gauss' theorem, the integral of the divergence of magnitude over a volume $\int_V \nabla(k\nabla T)\, dV$, can be assimilated by the flux of this magnitude over the area surrounding such a volume $\oint_A k\nabla T \cdot dA$, and therefore the following equation is obtained:

$$\mathrm{C}\frac{\partial T}{\partial t} + kA\nabla T = Q \tag{2.6}$$

with $\mathrm{C} = \rho c V$ and $Q = q_i V$. If the temperature gradient is linear, $\nabla T = (T - T_0)/L = \Delta T/L$, and we obtain:

$$\mathrm{C}\frac{\partial T}{\partial t} + G\Delta T = Q \tag{2.7}$$

where $G = kA/L$ is the thermal conductance between the hot and cold sides of a material (at temperatures T and T_0, respectively). Equation 2.7, describes the energy conservation in the material. When heat is dissipated inside the material (whichever the source), part of this energy contributes to the internal heat capacity, and part is released towards the surroundings through the material surface. If the heat generated is zero (Q=0), the equation can be reorganized as:

$$\frac{dT}{\Delta T} = -\frac{dt}{\tau} \tag{2.8}$$

being $\tau = C/G$ the thermal relaxation time of a system, like the one described in figure 2.1. This parameter is of prime importance for many applications, including thermal sensing or ac measurements, and should be properly characterized. In steady state, the $t \gg \tau$ relation must be obeyed, being t the waiting time to perform the measurement.

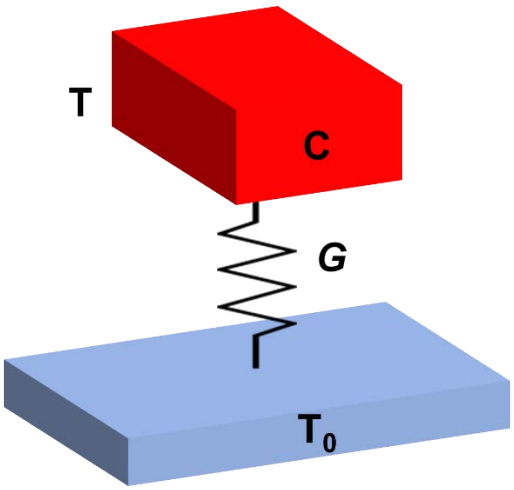

Figure 2.1 Solid at temperature T connected to a thermal bath at temperature T_0 through a thermal conductance G.

2.1.2 Boltzmann Transport Equation

The Boltzmann Transport Equation (BTE) describes the thermodynamics of a system out of equilibrium and its time evolution. In the discussion performed previously, the microscopic behavior of the heat and the thermal transport were not directly considered, whereas the BTE allows to observe the contribution of particles, such as phonons and electrons to the heat transport.

The BTE is defined in its general form as:

$$\frac{\partial f}{\partial t} + \frac{d\boldsymbol{r}}{dt} \cdot \nabla_{\boldsymbol{r}} f + \frac{d\boldsymbol{p}}{dt} \cdot \nabla_{\boldsymbol{p}} f = \left(\frac{\partial f}{\partial t}\right)_{col} \quad (2.9)$$

where f is the distribution function of a collectivity of particles, $\boldsymbol{r}$ and $\boldsymbol{p}$ are the position vector and the momentum, respectively. Therefore, for each particle the r and p vector define its state in the phases space. The BTE permits to determine how the distribution function evolves in time inside a given phase space volume $d\boldsymbol{r} \times d\boldsymbol{p}$ as a consequence of: i) the drift term, $\frac{d\boldsymbol{r}}{dt} \cdot \nabla_{\boldsymbol{r}} f$, related to the motion of the distribution function, ii) the external forces term, $\frac{d\boldsymbol{p}}{dt} \cdot \nabla_{\boldsymbol{p}} f$, that modifies the momentum of the distribution function, and the collisions term, $\left(\frac{\partial f}{\partial t}\right)_{col}$.

In the next sections, the BTE will be applied to phonons and electrons in order to define the thermal conductivity and the current generated by a temperature gradient (Seebeck effect).

2.1.2.1 Phononic and Electronic Transport

In the microscopic picture, heat inside matter can be transported by phonons and electrons.

BTE with phonons

First, the BTE will be applied to phonons to obtain the lattice contribution to the thermal conductivity. To consider phonons, we will use the Bose-Einstein equilibrium distribution function with energy equal to $\hbar\omega$, where ω is the phonon frequency. Therefore, in equilibrium (referred as f_0), the distribution function can be written as:

$$f_0(\omega) = \frac{1}{e^{\frac{\hbar\omega}{k_B T}} - 1} \quad (2.10)$$

In the case of phonons, the external force term, $\frac{d\boldsymbol{p}}{dt} \cdot \nabla_{\boldsymbol{p}} f$, can be removed since no external force can interact with them. Under the assumption of the diffusive approximation, and moderated temperature gradients, the drift term can be simplified since the distribution function is expected to vary softly in space and time, and the gradient of the distribution function in space can be assumed as: $\nabla_{\boldsymbol{r}} f = \frac{df}{dT} \cdot \nabla_{\boldsymbol{r}} T$.

Assuming local equilibrium, approximation that essentially means that $f - f_0$ is very small compared to f_0, the first term can be neglected $\left(\frac{\partial f}{\partial t}\right) \cong 0$. Under the relaxation time approximation, the collision term $(\frac{\partial f}{\partial t})_{col}$ can be further approximated by $(f - f_0)/\tau$ where τ is the relaxation time associated to the various scattering events, τ_i. The relaxation time can be written within the Matthiessen rule as: $\frac{1}{\tau} = \sum_i \frac{1}{\tau_{i_0}}$. The out of equilibrium distribution function can be re-expressed as:

$$f(\omega) - f_0(\omega) = \frac{\partial f_0(\omega)}{\partial T} \tau(\omega) v_g(\omega) \cdot \nabla T \tag{2.11}$$

where v_g is the group velocity. .The BTE permits to stablish the evolution of the distribution function considering the product of the temperature derivative of the equilibrium distribution, the relaxation time, the group velocity and the temperature gradient in the system.

Therefore, a temperature gradient generates a heat flux that can be written as:

$$dq_x = \hbar\omega \cdot v_{gx}\big(f(\omega) - f_0(\omega)\big) D(\omega) d\omega \tag{2.12}$$

Combining Equations 2.11 and 2.12, integrating and using the Fourier law we obtain, after some algebra, an expression for the lattice thermal conductivity:

$$k_l = \frac{1}{3} \sum_\lambda \int_0^{\omega_{max}} v_g(\omega)\, l(\omega) C(\omega) d\omega \tag{2.13}$$

where λ is the phonon branch polarization, $l = \tau(\omega) v_g(\omega)$ is the mean free path (MFP) of the phonons (the average distance traveled by a phonon between two scattering events), and C is the spectral heat capacity. The mean free path typically depends on the scattering mechanisms presents in the system, and the Matthessien's rule determines how they should be added $\frac{1}{l(\omega)} = \sum_i \frac{1}{l_i(\omega)}$. The most common scattering mechanisms are:

- *The phonon-phonon scattering*: when two phonons are recombined they can conserved momentum if the addition falls into the first Brillouin Zone (BZ) or interact with the net, releasing momentum, if the resulting phonon falls outside of this 1st BZ. In the first scenario, also called normal scattering, the phonon

momentum is conserved and cannot be considered as an inelastic term (it is non-resistive), nevertheless this type of collisions contribute to repopulate the different modes of the phonon distribution, and indirectly affect the heat conduction, and should be considered. In the last situation, the phonon momentum is not conserved evidencing a resistive behavior that is dominant at high temperatures. This scattering processes are called Umklapp events. Therefore, the probability of the Umklapp scattering process depends on the population of high energy phonons and, for that reason, the related mean free path decreases exponentially with temperature, $l_{Uk} = T^3 e^{-A/T}$.

- *Impurity scattering* considers the scattering events between a phonon and an impurity in the crystal e.g. a doping atom or an interstitial atom. Usually it is modeled as the Rayleigh scattering of light, i.e. with a ω^4 dependence: $l_{Imp}^{-1} \propto \omega^3$.
- *Boundary scattering*: is produced when a phonon reaches the boundary of a material and is reflected, either in a specular or diffusive way. In polycrystalline materials, it appears when phonons reach a grain boundary. The MFP associated to the boundary scattering is $l_B = L \cdot S$, where L is the size of the material/grain and S is the specularity parameter (S=∞ for completely specular and S=1 for a completely diffusive). In nanomaterials, the boundary scattering typically becomes the dominant scattering source because of the reduced sample dimensions. Nevetherless, for highly crystalline bulk materials it can also become an important scattering source especially at low temperatures.

As a result of the different scattering processes, the broad family of phonons contributing to thermal transport can selectively be targeted. For instance, mass isotope scattering that is especially relevant in alloys will heavily impact short wavelength (high frequency) phonons. Interfaces between acoustic dissimilar materials as occurs in superlattices or grain boundaries in polycrystalline solids may impact medium range wavelength phonons while thin film boundaries block long-wavelength phonons. Figure 2.2 shows as an example how the spectral mean free path is affected for different silicon-based materials. When alloying with Ge, the high frequency phonons become preferentially scattered. In thin film, SiGe superlattices, the low frequency phonons (large wavelengths) that typically can see the alloying as an effective media, scatter inevitably with the interfaces, and combining both types of features in a single sample the complete family (phononic spectra) is targeted [3].

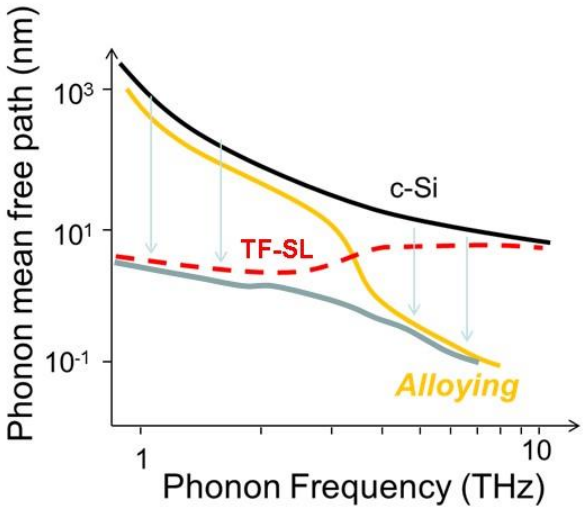

Figure 2.2 Modification of the phonon mean free path due to different scattering centers, from atomic defects or impurities to thin film boundaries. TF stands for thin film and SL for superlattice.

BTE with electrons

Now, we will apply the BTE formalism to electrons. Since electrons do transport both energy and charge, the analysis will serve to verify the participation of the electrons in the thermal conductivity, to evaluate the electrical conductivity and also to derive the thermoelectric properties. We first consider that electrons obey Fermi-Dirac statistics and therefore the distribution function can be written as:

$$f_0 = \frac{1}{e^{\frac{\varepsilon-\mu}{k_B T}}+1} \tag{2.14}$$

where ε is the electron energy and μ is the chemical potential considered from the conduction band edge. Under a similar analysis than the proposed to solve the BTE for phonons, in the case of electrons, we should considered the presence of an arbitrary electric field (E_x), as an external force term, together with temperature gradient in steady state. The analysis retrieve that the evolution of the distribution function now follows:

$$f - f_0 = -\tau v_x \left(\frac{\partial f_0}{\partial x} + \frac{\partial f_0}{\partial v_x}\right) = \tau v_x \left(\frac{\partial \mu}{\partial x} + \frac{\varepsilon-\mu}{T}\frac{dT}{dx} + eE_x\right)\frac{\partial f_0}{\partial \varepsilon} \tag{2.15}$$

Like in the previous case, with this expression we can determine the number of particles flowing through the system, and therefore, considering either the charge or the energy the particles carry, the charge current density (J_x^{-e}) and the heat current density (q_x^{-e}) can be determined.

Charge flux due to electrons

For electrons (e^- charged), only those with energies around the chemical potential, will present a thermodynamic force to contribute to the particle flux. Typically, those with energies higher than the chemical potential will flow toward the external force or against the temperature gradient, while those below the chemical potential will have the reverse direction. To evaluate the flux, the total number of electrons contributing should be accounted and, that requires, the integration over the whole density of states weighted by the distribution function difference along the system and considering the velocity for each energetic level:

$$J_x^{-e} = \int_0^{\infty} -ev_x D(\varepsilon)\,(f - f_0)d\varepsilon \tag{2.16}$$

Combining Equation 2.15 in Equation 2.16 we get:

$$J_x = L_{11}\left(\frac{1}{e}\frac{d\mu}{dx} + E_x\right) + L_{12}\left(-\frac{dT}{dx}\right) \tag{2.17}$$

being

$$L_{11} = -\frac{e^2}{3}\int_0^{\infty} \upsilon^2 \tau D(\varepsilon)\frac{\partial f_0}{\partial \varepsilon}d\varepsilon \tag{2.17a}$$

$$L_{12} = \frac{e}{3T}\int_0^{\infty} \upsilon^2 \tau D(\varepsilon)\frac{\partial f_0}{\partial \varepsilon}(\varepsilon - \mu)d\varepsilon \tag{2.17b}$$

Taking Equation 2.17 and considering that there is not temperature gradient, it is possible to obtain the electrical conductivity:

$$J_x = L_{11}\left(\frac{1}{e}\frac{d\mu}{dx} + E_x\right) \equiv \sigma E_x' \tag{2.18}$$

where E_x' is the effective electric field that takes in consideration the gradient in chemical potential. But, if we impose in Equation 2.17 the open circuit condition, in the absence of current density, the Seebeck coefficient is obtained as:

$$E'_x = \frac{L_{12}}{L_{11}}\frac{dT}{dx} = S\frac{dT}{dx} \tag{2.19}$$

thus

$$S = -\frac{1}{eT}\frac{\int_0^\infty v^2\tau D(\varepsilon)\frac{\partial f_0}{\partial \varepsilon}(\varepsilon-\mu)d\varepsilon}{\int_0^\infty v^2\tau D(\varepsilon)\frac{\partial f_0}{\partial \varepsilon}d\varepsilon} = \frac{1}{eT}\frac{\int_0^\infty v^2\tau D(\varepsilon)\frac{\partial f_0}{\partial \varepsilon}(\varepsilon-\mu)d\varepsilon}{\sigma} \tag{2.20}$$

As this demonstration was performed considering electrons, the Seebeck coefficient has a negative sign, which will be positive if we consider holes. In most cases *S* has the sign of the free carriers, however *S* can be positive even in metals with negative charge carriers such as Li or Ag due to the strong dependence of the density of states across de Fermi energy in those materials [4].

Through Equation 2.20 we can note that the Seebeck coefficient is a relation between the average energy of an electron above the Fermi level at open circuit and the differential electrical conductivity at each energy level. In addition, the $(\varepsilon - \mu)$ term indicates that *S* is related to the heat carried per electron [5].

Heat flux due to electrons

Following the same procedure, we can consider now the amount of heat transported per charge $(\varepsilon - \mu)$, to be evaluated with a similar integration of the heat flux:

$$q_x = \int_0^\infty v_x D(\varepsilon)(f - f_0)(\varepsilon - \mu)d\varepsilon = L_{21}E'_x + L_{22}\left(-\frac{dT}{dx}\right) \tag{2.21}$$

where

$$L_{21} = \frac{e}{3}\int_0^\infty v^2\tau D(\varepsilon)\frac{\partial f_0}{\partial \varepsilon}(\varepsilon - \mu)d\varepsilon = TL_{12} \tag{2.21a}$$

$$L_{22} = -\frac{1}{3T}\int_0^\infty v^2\tau D(\varepsilon)\frac{\partial f_0}{\partial \varepsilon}(\varepsilon - \mu)^2 d\varepsilon \tag{2.21a}$$

Combining equation (2.17) and (2.21), yields:

$$q_x = \frac{L_{21}}{L_{11}}J_x + \left(L_{22} - \frac{L_{21}L_{12}}{L_{11}}\right)\left(-\frac{dT}{dx}\right) \tag{2.22}$$

Without temperature gradient, we find the Peltier coefficient Π.:

$$q_x = \frac{L_{21}}{L_{11}} J_x \equiv \Pi J_x \tag{2.22a}$$

And imposing a negligible current density, we find the electrical component of the thermal conductivity

$$q_x = \left(L_{22} - \frac{L_{21}L_{12}}{L_{11}}\right)\left(-\frac{dT}{dx}\right) \equiv k_e \left(-\frac{dT}{dx}\right) \tag{2.22b}$$

To consider the total thermal conductivity of a material, both phononic (lattice) and electrical component should be sum: $k = k_l + k_e$.

Combining equations (2.17), and Equation (2.21), we obtain the Wiedemann-Franz law that provides a direct relation between the electrical σ and thermal k_e conductivities, due to electrons:

$$\frac{k_e}{\sigma T} = \frac{\pi^2 k_B^2}{3e} \equiv L \tag{2.23}$$

where *L* is the Lorentz number that is nearly constant for many materials.

Phonon drag

In the above derivation, we did not consider the interaction between phonons and electrons, thus, we only took into account the diffusive component of the Seebeck coefficient. However, if the electron-phonon coupling is strong an additional component of the Seebeck coefficient should be considered. In certain condition and materials, the electrons (holes) can be dragged by the phonon flux increasing the Seebeck coefficient. This effect is known as phonon drag. The phononic component of the Seebeck coefficient can be described by [6]:

$$S_{ph} = \pm \frac{c^2 \tau}{\mu T} f_{pe} \tag{2.24}$$

where τ is the relaxation time for the dissipation of the phonon's momentum due to the interaction with the atoms, c is the sound velocity, μ is mobility of the charge carriers, *T* the temperature and f_{pe} is the fraction of crystal momentum taken from the lattice by the charge carriers.

2.2 Thermoelectricity

In the next section, the Seebeck coefficient, the electrical and the thermal conductivity will be discussed in the context of thermoelectricity. The possibilities of enhancing the Seebeck coefficient and the electrical conductivity maintaining, or reducing, the thermal conductivity of a material will be further analyzed.

2.2.1 Introduction

Thermoelectricity is the capacity of a material to couple thermal and electrical phenomena. Specifically, thermoelectricity is determined through the direct conversion of a *temperature* difference into an *electric* potential or an *electric* current into a *temperature* difference. These phenomena are known as Seebeck and Peltier effects respectively. The Seebeck effect is related to the capacity of a material under open circuit conditions to generate an output voltage in response to a temperature gradient. This voltage is known as Seebeck voltage in honor to its discoverer, Thomas Johann Seebeck, in 1822 [7,8]. If the material is formed by two solids with different (positive and negative) charge carriers an electrical current can be generated and therefore the system is able to transform heat into electrical power. The Seebeck effect can be described by the following equation:

$$V = S \cdot (T_1 - T_2) \tag{2.25}$$

where V is the voltage generated at open circuit, S the Seebeck coefficient of the material and T_1 and T_2 the temperatures at both extremes. If the system is formed by two materials with Seebeck voltages S_A and S_B, the above relation is rewritten as:

$$V = S_{AB} \cdot (T_1 - T_2) \tag{2.26}$$

where S_{AB} is the difference between the Seebeck coefficients of the A and B materials. The joint of two different materials connected electrically in series and thermally in parallel is named thermocouple.

The second (and related) effect was discovered by Jean Charles Athanase Peltier in 1852 [9]. He observed that, when an electric current was applied to a metallic junction, a variation of temperature occurred, which depending on the direction of the electric

current, could reverse the temperature difference. This effect, known as the Peltier effect, can be mathematically written as:

$$Q = (\Pi_1 - \Pi_2)I \tag{2.27}$$

where Q is the heat flux, Π_1 and Π_2 are the Peltier coefficients of each material and I is the current applied to the thermocouples. In figure 2.3, both Seebeck and Peltier phenomena are depicted.

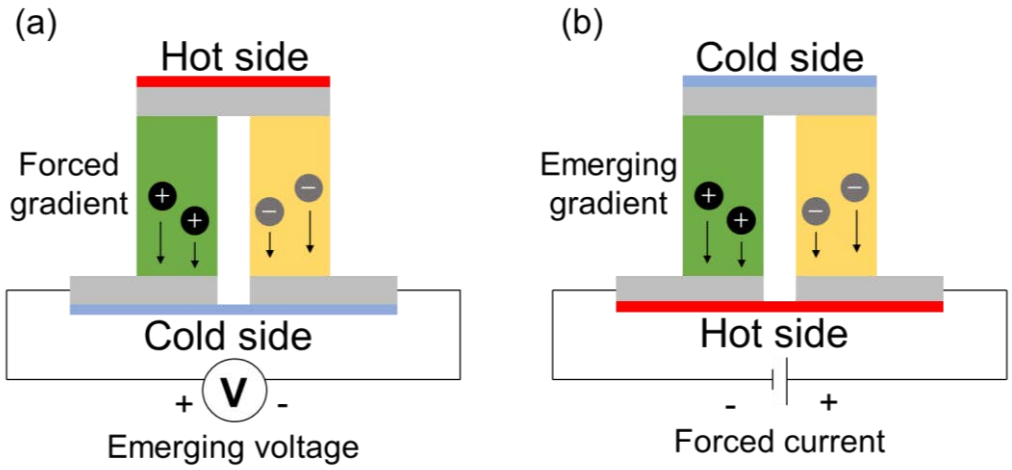

Figure 2.3 Visual description of the Seebeck effect **(a)** and the Peltier effect **(b)** In the first case, a temperature gradient produces a voltage along the thermocouple, while in the second case a current flowing through the thermocouple generates a heat flux.

Thermoelectric materials can be used to build a thermoelectric generators (TEG), that is a heat engine that converts waste heat into electricity and usable work. As a thermal engine, it obeys the thermodynamic laws and the maximum efficiency of a TEG is also limited by the Carnot efficiency, i.e. the ratio between the cold (heat sink) and hot (heat source) temperature sides, as shown in equation 2.28:

$$\eta_C = 1 - \frac{T_C}{T_H} \tag{2.28}$$

However, real engines and processes never attain the maximum efficiency. For a TEG, the efficiency is related to the ability of a material to conduct electricity while preserving the temperature gradient. Maximizing the efficiency of thermoelectric

machine, arises parameter *ZT* as the Figure of Merit. In *ZT* the Seebeck coefficient (S), the electrical (σ) and the thermal (k) conductivity of a thermoelectric material are related through the following equation:

$$ZT = \frac{S^2\sigma}{k}T \tag{2.29}$$

where T is the mean temperature of the system. It can be shown that the efficiency of a thermoelectric generator obeys the following equation:

$$\eta_{TE} = \eta_C \frac{\sqrt{1+ZT_M}-1}{\sqrt{1+ZT_M}+\frac{T_C}{T_H}} \tag{2.30}$$

where ZT_M is the average Figure of Merit of the materials of the TEG at the mean temperature, $T_M = \frac{T_H+T_C}{2}$.

It is obvious from 2.29 and 2.30 that enhancing *ZT* of the materials will increase the efficiency of any TEG. The great challenge to improve *ZT* is to simultaneously increase the Seebeck coefficient and electrical conductivity while decreasing the thermal conductivity. This is in fact a great challenge that has engaged many scientists for decades because the parameters of the *ZT* equation are interrelated and it is not trivial to manipulate each parameter individually. The Seebeck coefficient and the electrical conductivity are related through the Pisarenko relationship (eq 2.20). Thus, the increase of the electrical conductivity by, for instance, doping in a semiconductor leads to a decrease of the Seebeck coefficient. Moreover, in metals and degenerated semiconductors the electronic contribution to the thermal conductivity can be very high as can be easily deduced from the Wiedemann-Franz law (Equation 2.17). In Figure 2.4 we can observe the relations defined before, the improvement of the Figure of Merit is very challenging, since the rise of σ decreases *S* and increases k.

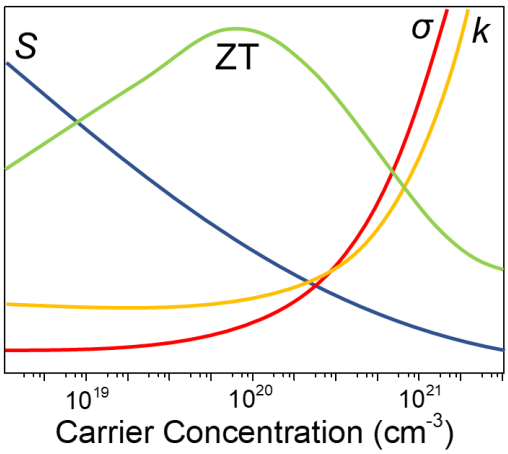

Figure 2.4 Plot of Figure of Merit, Seebeck coefficient, electrical and thermal conductivities as a function of carrier concentration.

In the next sections, several strategies to independently modify the values of the Seebeck coefficient and the electrical and/or thermal conductivities will be discussed individually, exploring the possibilities of *ZT* enhancement.

2.2.2 Enhancing *ZT* by tailoring the thermal conductivity

The main goal of the thermal conductivity is to reduce its value independently of the electrical conductivity and/or Seebeck coefficient, thus improving the *ZT*. As explained before, the thermal conductivity has two contributions, one related to the charge carriers and another related to lattice vibrations. Decreasing the electronic component of thermal conductivity implies reducing its electrical conductivity, thus, the main strategy used to improve *ZT* is to decrease the lattice contribution. One useful concept is the one introduced by Slack, the so-called phonon-glass electron-crystal (PGEC) [10–12]. A thermoelectric material that behaves as a PGEC is a material with crystal structures that permit the electronic transport as in a single-crystal while the heat flux due to phonons is blocked by the lattice like in a glass. There are many possibilities to alter the thermal transport in a material without much affecting its electrical properties. The lattice component of the thermal conductivity is described by Equation 2.13. In practice it is possible to reduce either the heat capacity, the sound velocity or the mean free path of the phonons: i) using materials constituted by heavy mass atoms with low elastic modulus and therefore lower sound velocity and k [13–19]; ii) using alloys in which mass differences between the atoms create additional scattering mechanism reducing the mean free path of the phonons [3,20–24]; iii) taking advantage of anharmonicity in solids [25,26]; iv) decreasing the grain size in polycrystals will strongly enhance grain boundary scattering decreasing

k; v) decreasing the size of the material in any of its dimensions will increase the boundary scattering with the surface/interface reducing k. This last methodology has been largely used in the past 20 years leading to strong reductions of the thermal conductivity approaching or even having *k* values below the amorphous limit.

Another mechanism that has been recently invoked to produce a reduction of the thermal conductivity is the weak chemical bonding of some materials in one of its crystallographic directions. Recent examples include WSe2 [27] and other layered materials [12,28,29].

2.2.3 Enhancing ZT by tailoring the electrical conductivity

The enhancement of the electrical conductivity in a semiconductor can be easily realized by increasing the doping level. However, as shown in Figure 2.4, the rise of the doping level leads to a reduction of the Seebeck coefficient, Equation 2.20. In relation to the thermal conductivity, two processes occur simultaneously: On one hand, the increment of the doping level increases the contribution of the electronic component, while on the other hand, it decreases the contribution of the lattice component owing to the scattering caused by the random location of impurities. Doping optimization is the most common method to improve the electrical conductivity of a semiconductor. A maximum power factor ($PF = S^2\sigma$) is attained at a specific carrier concentration. In general, the ideal doping level is between 10^{19}-10^{20} cm^{-3} [30]. Another strategy used to increase the electrical conductivity is the modulation doping, which consists in to separate spatially the charge carriers from their parent impurity atoms. This separation reduces scattering caused by the impurity and consequently, increases the electrical conductivity [31,32].

2.2.4 Enhancing ZT by tailoring Seebeck coefficient

The Seebeck coefficient is the parameter that quantifies the generated voltage for a material when its edges are submitted to a temperature difference. This parameter can be related to diffusive and phononic process. The most significant originates due to the energy received by the charges, starting a diffusion from the hot to the cold side. The second process is known as phonon drag effect and is due to a strong electron/hole-phonon interaction by which phonons transfer momenta to the charge carriers. The effect is a net force that pushes the charge carriers in the same direction of the heat flux

contributing to the charge carrier rise in the cold side. This dual contribution to S can be written as:

$$S = S_d + S_{ph} \tag{2.31}$$

where S_e is the diffusion contribution and S_{ph} is the phononic one. Generally, the phonon drag component increases at low temperatures, fact associated to a reduction of the scattering mechanisms at low temperatures. In nanostructures, strong phonon drag effect are not expected since the MFP of the phonons decreases [33–35]. Nevertheless, there is some controversy in relation to this, since Boukai et. al. recently reported the existence of phonon drag effect in nanowires [36]. They explained the observation by considering that the MFP is suppressed in two dimensions while it remains equal in the propagation direction. Moreover, it is known that the doping level modifies the contribution of the phonon drag effect to the Seebeck coefficient. At low doping levels, up to 10^{17} cm^{-3}, the phonon drag effect remains constant because the total momentum transferred depends on the electronic states available that can couple to phonons, while when the doping level value exceeds 10^{17} cm^{-3}, the carrier concentration begins to saturate the electronic states and induces a reduction in the momentum gain per electron, producing a decrease of the phonon drag effect. Despite that, as described by Zhou et al. the phonon drag effect still exists in doped silicon with 10^{19} cm^{-3} carrier concentration [37]. In this same work, Zhou proposes the manipulation of the phonon drag effect as a possible way to improve the *ZT*, owing to the fact that phonons that contribute to the phonon drag effect have a MPF and a frequency different from phonons that contribute to the heat transport [37].

As explained before, in semiconductors, the *S* is related to σ by the Pisarenko relation (Equation 2.20), which can also be written as [38]:

$$S = \frac{8\pi^2 k_B T}{3qh^2} m_d^* \left(\frac{\pi}{3n}\right)^{2/3} \tag{2.31}$$

here k_B is the Boltzmann constant, *T* is the temperature, *q* is the charge carrier, m_d^* is the DOS of the effective mass and *n* is the charge concentration. Through this relation, it is possible to verify that the rise of the doping level decreases the Seebeck coefficient. Also, through Equation 2.23 it is possible to note that the Seebeck coefficient depends on the Fermi level position in relation to the DOS, which can be used to improve the Seebeck

coefficient by causing a high variation on the DOS around the Fermi energy level. In this way, the improvement of *S* can be reached through: i) resonant energy levels caused by impurities into bulk-band structure [39]; ii) quantum size effect in low-dimension materials [40,41]; iii) introducing a potential scattering that causes an energy filtering of minority carriers or hot carriers [42,43] and iv) increasing the energy dependence of the relaxation time or mobility.

2.3 Photothermoelectric effect

In our previous analysis of thermoelectricity, we have always assumed that the charge carrier population is defined by the doping and charge movement is driven by temperature differences. Temperature gradients are typically imposed by Joule heating of a resistive metal or by other external sources. Now we introduce a new process: the presence of photo-excited carriers, both electrons and holes, due to light absorption in certain regions of the device. Our aim (see chapter 4 for the experimental realization) is to explore the impact of photogeneration together with the existence of large thermal gradients in the thermoelectric response of the device.

There is some confusion in the literature about the use of the word photothermoelectric. Some authors refer to a purely thermoelectric effect that is originated by the temperature gradient induced by light absorption. That is upon illumination with a focused laser beam on a thermoelectric material a temperature gradient can be established between the hot illuminated area and a heat sink, and an open circuit voltage difference will be stablished between hot and cold sides. Since the temperature difference, and therefore the voltage output, is driven by light absorption this phenomenon has been called by some authors as photo-thermoelectricity. While this may sound reasonable this effect may not contain new physics with respect to standard thermoelectric effects. However, light absorption produces photo-excited carriers in semiconductors, i.e. electron-hole pair generation. Therefore, we aim to find a photothermoelectric effect (PTE) that is in fact a true combination of thermoelectric and photovoltaic effects in which the charge carriers generated by light result in a positive influence to the thermoelectric properties. Therefore, we understand photo-thermoelectricity as the combined effect by which light locally heats and induces new charge carriers in a spatial region of the sample. It is not clear yet the true impact of light

irradiation on the thermoelectric conversion, since electron-hole carrier generation could modify both the Seebeck coefficient and the electrical conductivity.

At first sight the Seebeck coefficient in a semiconductor may not be modified much or even should decrease if photocarriers are generated since ambipolar conduction by electrons and holes is often negative to thermoelectricity. To understand the modification of the Seebeck coefficient under illumination, we need to remember that the Seebeck effect is related to the heat transported by charge carriers from high to low temperature surfaces. The $(\varepsilon - \mu)$ term of Equation 2.20 can also be related to the entropy, as explained by Chen [5]. Thus, the entropy difference between the hot and cold sides yields the diffusive part of the Seebeck coefficient. In addition, the phonon drag effect may contributes to the Seebeck effect, being an additional term of the Seebeck coefficient caused by the electron-phonon interaction.

Now, knowing that an incident photon generates an electron-hole pair, a question that arises is how the Seebeck coefficient can be modified if the same amount of electrons and holes are generated by photoexcitation process, and both charge carriers will flow from hot to cold side. In a doped semiconductor, the majority charge carriers have higher lifetime and diffusion lengths than the minority charge carriers. Therefore, an unbalanced between the population of electrons and holes may exists and reach the contacts if electron-hole pairs are produced at distances from the contact shorter than the diffusion length. In addition, photoinjection will produce hot carriers (electrons/holes) with average energies above/below the quasiFermi level of the doped semiconductor. The small fraction of majority charge carriers created by photoexcitation (hot carriers) that survive and are injected into the contact can a-priori positively influence the Seebeck coefficient. Besides that, as explained by Hu et al. in polymers the phonon drag effect leads to a polarization difference between the high and low temperature surfaces, producing an additional force (through an Electric field) that is applied to the charge carriers and improves the Seebeck effect [44].

Figure 2.5 shows several processes that may be involved in the modification of the Seebeck effect caused by the photogeneration of charge carriers. In this case, a *p*-type semiconductor is illuminated by light with a wavelength λ_{exc} , which generates an electron-hole pair. The l_{h^+} and l_{e^-} represent the diffusion length of majority and minority carriers, respectively, being $l_{h^+} > l_{e^-}$. CS and HS are the cold and hot sides, respectively. If the distance at which photocarriers are generated is lower than the diffusion length

those hot carriers may reach the electrode and contribute to rise the thermovoltage and the Seebeck coefficient.

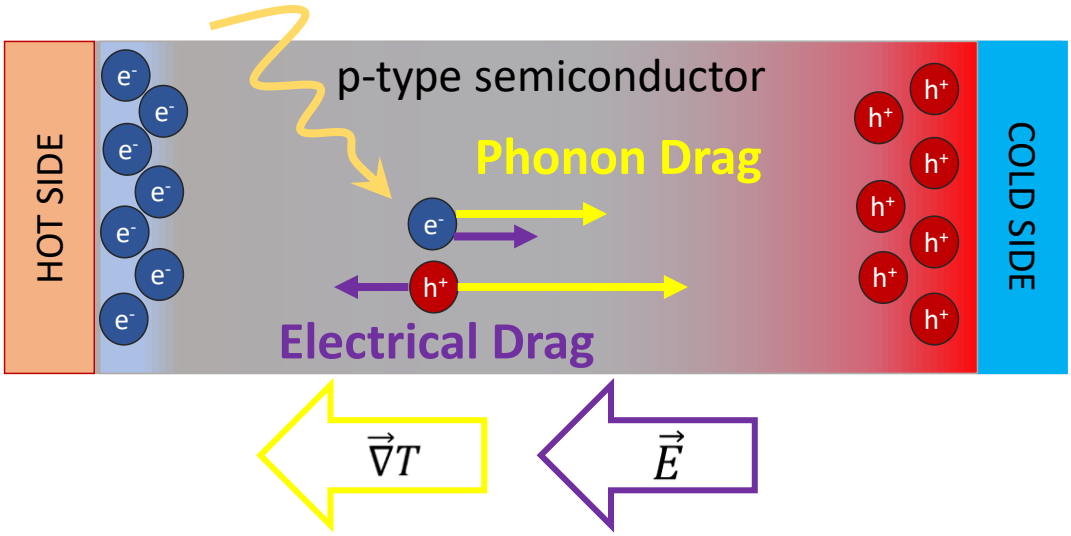

Figure 2.5 Enhancement of the Seebeck effect in a *p*-type semiconductor.

3. Experimental Methods

In this chapter, we will describe the measuring techniques and experimental setups used along this work. To measure the in-plane thermal conductivity of ultrathin films, that have been obtained by spin-coating or sputtering techniques, we use an adapted 3ω-Völklein method. The method requires the use of vacuum environments, to control heat leakages and guarantee a high thermal stability, to minimize thermal associated noises during the measurement. We will present a custom-built thermostatic holder that has been design to hots the devices inside the high vacuum chamber and the high resolution power compensation temperature controller. To measure the electrical conductivity and the Seebeck coefficient of the thin films, we have designed and develop a specific device based on a microfabricated chip structure, where the temperature gradients are stablished with the aid of a set (a couple) of twin Peltier cells.

3.1 3ω-Völklein method

The thermal conductivity is a physical parameter that relates the heat flux transported through a material when a temperature gradient is stablished. This is material property of key importance for thermal management and, in particular, to determine the thermoelectric performance, since having a low thermal conductivity allows preserving a high temperature difference between the hot and cold junction in a thermoelectric device.

Thermal conductivity has been classically considered as an intrinsic property of materials, it means independent of the body size and volume. However, with the advent of nanotechnology, the study of nanomaterials has shown that phonon boundary scattering can reduce the thermal conductivity of the material, provided that the size of one of its dimensions is of the order of the phonon mean free path. Due to the geometrical anisotropy inherent to many nanomaterials and nanostructures, the thermal conductivity can become highly anisotropic too. In the case of superlattices, ultrathin films or 2D materials, the in-plane $(k_{\parallel})$ (parallel to the sample surface) and out-of-plane $(k_{\perp})$ (perpendicular to the sample surface) thermal conductivities can be different. This usually happens with single-crystalline or polycrystalline materials, where the bulk phonon mean free path is much higher than the layer thickness.

To determine the thermal conductivity of a material, the technique used should allow to measure the temperature difference along the sample and the heat transported in this process. Many techniques have been developed to study the thermal conductivity of thin films, superlattices or even membranes. They can be classified according to the type of sensing and heating used: electrical and optical. Electrical techniques are based on the Joule heating of a metallic strip to produce a temperature gradient and the associated heat flux through the sample. In these techniques, the temperature difference is measured using either the same or another metallic strip as temperature probe. Analogously, optical techniques use a light beam as heat source and probe, or separate beams for heating and sensing (pump-probe configuration) [45–47]. In these cases, the thermal conductivity is obtained by the difference observed in optical phenomena such as diffraction, reflectance and others. There are also some hybrid methods that combine both electrical and optical signals. For example, K. E. Goodson et al. developed a technique that uses an electrical signal to heat the sample and obtains thermal signal by the reflectance change of the sample [48]. The main techniques used to determine the thermal conductivity are listed in Table 3.1:

Techniques to measure the thermal conductivity		
Electrical Heating	**Optical Heating**	**Hybrid**
AC	**Time Domain**	
3ω ‖ 2 strips 3ω ⊥‖	Photoreflectance ⊥ Thin-Film Laser Flash Analysis ⊥ Transient Grating ‖	AC calorimetry ⊥‖ Photo-thermoelectric ⊥‖
DC	**Frequency Domain**	
Steady State ‖ Membrane ‖ Bridge ‖ Spreader ‖	Photoreflectance ⊥‖ Emission ⊥ Displacement ⊥ Deflection ⊥‖ Photo-acoustic ⊥	Electric- reflectance ⊥ Electric-emission ⊥

Table 3.1 Summary of the experimental methods to measure the thermal conductivity [49].

The main difficulty to measure the effective thermal conductivity of a thin film is to limit the heat to be transported only through the sample without the influence of the support substrate and surrounding structures. Moreover, one should minimize the impact of thermal interface resistances with the rest of materials that heat will pass through. Some optical techniques with a pump-probe configuration can measure the thermal conductivity without the impact of thermal interface resistances, however, these techniques many times possess difficulties to determine the in-plane thermal. In order to reduce the contribution of the substrate in the measurements, the membrane-based methods were developed, providing high sensitivity.

The 3ω-Völklein method is one of these membrane-based techniques, which is used to measure the in-plane thermal conductivity in thin films. The great advantage of this technique developed initially by Völklein in DC and subsequently by Sikora in the frequency domain is its high sensitivity and resolution, around 10 nW/K and $\Delta G/G=10^{-3}$, respectively [50]. To understand the 3ω-Völklein method, it is important to consider the combination between lock-in strategies linked to 3ω measurements and Völklein geometry. The development of the 3ω method to measure the thermal conductivity was realized by Cahill in the 1990s and it has now become a standard technique to evaluate the out-of-plane thermal conductivity of films and bulk materials [51]. In this method, a single longitudinal metallic strip is defined by lithography onto the sample. The strip is fed with alternating-current (AC) at ω frequency and serves simultaneously as heater and sensor. The 3ω component of the voltage generated by Joule effect can be related to the temperature gradient across the film and consequently with its thermal conductivity. Later on, the technique was further developed to measure the in-plane and out-of-plane thermal conductivity of thin films [52,53]. By using heater/sensors of different widths it is possible to change the relative contribution of the in-plane and through-plane components of k and by comparing with a 2D modelling extract $k_{\parallel}$ and $k_{\perp}$. However, this methodology is complex and far from being well stablished. On the other hand, Völklein and Starz developed a membrane-based method with a metallic strip operating in direct-current (DC) mode to directly measure the in-plane thermal conductivity of metallic thin films with thicknesses larger than 1 µm [54]. Subsequently, Sikora et al. evolved this methodology by combining the membrane-based geometry of the Völklein method with the 3ω-method attaining exceptional sensitivity. In the next sections the generation of 3ω voltage signal, the device and set-up built at GNaM for in-plane thermal conductivity measurements is described.

3.1.1 Generation of 3ω voltage

When metallic strip is fed with an AC current such as:

$$I = I_0 \sin(\omega t) \tag{3.1}$$

where I_0 is the amplitude of the current wave and $\omega = 2\pi f$ is the angular frequency.

The power dissipated in the strip by Joule effect is:

$$Q = I^2 R = {I_0}^2 R \sin^2(\omega t) = \frac{{I_0}^2 R}{2}(1 - \cos(2\omega t)) = Q_0(1 - \cos(2\omega t)) \tag{3.2}$$

Equation 3.2 contains two terms: the first one is a constant component, $Q_0 = \boldsymbol{\frac{{I_0}^2 R}{2}}$, due to self-heating and tends to a constant temperature for time $t \gg \tau$, where τ is the thermal characteristic time of the system. The second term oscillates at frequency 2ω. The temperature rise related to the two components can be written as:

$$\Delta T_{DC} \equiv \frac{Q_0}{G} \tag{3.3a}$$

and

$$\Delta T_{2\omega} \equiv \frac{Q_0}{G_{2\omega}} \tag{3.3b}$$

where $G_{2\omega}$ is the apparent thermal conductance. The apparent thermal conductance is smaller than the real thermal conductance since part of the heat is spent in the dynamic heating of the sensor. Moreover, the temperature oscillation can to be out of phase in relation to the heating wave. The total temperature variation is:

$$\lim_{t \to \infty} \Delta T = \Delta T_{DC} - |\Delta T_{2\omega}| \cos(2\omega t + \phi) \tag{3.4}$$

The oscillation of the temperature leads to an oscillation in the resistance, thus:

$$R = R_0 + \frac{dR}{dT}\Delta T = R_0 + \frac{dR}{dT}(\Delta T_{DC} - \Delta T_{2\omega} \cos(2\omega t + \phi)) \tag{3.5}$$

Applying equations 3.1 and 3.5 and the Ohm's law, the voltage measured in the strip is:

$$V = I_0 \sin(\omega t)\left(R_0 + \frac{dR}{dT}(\Delta T_{DC} - \Delta T_{2\omega}\cos(2\omega t + \phi))\right) \quad (3.6)$$

using trigonometric identities, we can rewrite equation 3.6 as:

$$V = I_0\left(R_0 + \frac{dR}{dT}\Delta T_{DC}\right)\sin(\omega t) + I_0\frac{dR}{dT}\frac{\Delta T_{2\omega}}{2}\sin(\omega t + \phi) - I_0\frac{dR}{dT}\frac{\Delta T_{2\omega}}{2}\sin(3\omega t) \quad (3.7)$$

A selective measurement of the third term of the equation $(V_{3\omega})$, which oscillates at 3ω, yields the temperature oscillation $\Delta T_{2\omega}$:

$$\Delta T_{2\omega} = \frac{2V_{3\omega}}{I_0\frac{dR}{dT}} \quad (3.8)$$

As further shown below the temperature oscillation can be related to the thermal conductance of the sample, thereunto the temperature coefficient of resistance (TCR) of the heater must be measured in the temperature range of measurement.

3.1.2 3ω-Völklein sensor

The device consists in a free-standing membrane of SiN_x on top of which a Pt strip with 4-wire configuration is deposited. The geometry of the device was optimized by Finite Elements Modeling (FEM) using COMSOL Multiphysics, which permits that the heat flows linearly from the central strip to the frame. Figure 3.1 shows a scheme of the device used in the 3ω-Völklein method.

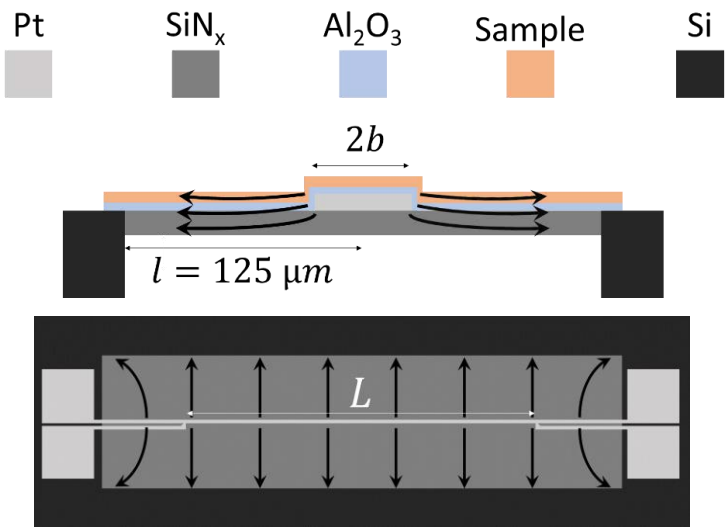

Figure 3.1 Scheme of the device used in the 3ω-Völklein measurements. The side and top view, the arrows represent the direction of the heat flux in the membrane/sample.

The membrane has an area of 3mm x 250µm and a thickness of 180 nm, the Pt strip has dimensions of 3mm x 5µm, 100 nm thick and the distance between the voltage probes is 2 mm. Figure 3.2 presents the optical image of the 3ω-Völklein device.

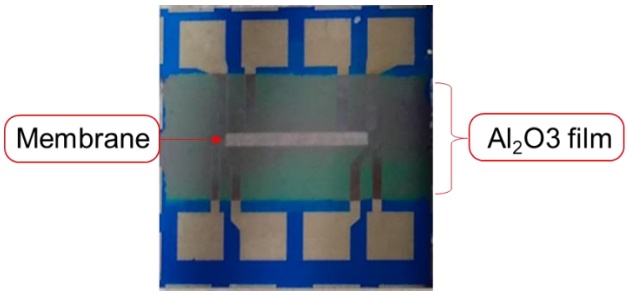

Figure 3.2 Optical image of the 3ω-Völklein device.

Since it is simpler to deposit/grow the samples on top of the device (figure 3.2) an insulating alumina (Al_2O_3) film with thickness 50 nm was deposited onto the heater/membrane prior to sample growth with the goal to isolate the heater/sensor from the sample. This is especially relevant and necessary for conducting samples

3.1.3 Microfabrication of the 3ω-Völklein sensor

The 3ω-Völklein sensor was microfabricated using the following steps:

i) The process begins with a 4-inch Si wafer with 525 µm of thickness and slightly doped (*p*-type and electrical resistivity 20 Ω.cm).

ii) Formation of 50 nm of SiO_2 layer by oxidation.

iii) Growth of a 180 nm thick SiN_X film via low pressure chemical vapor deposition (LPCVD) at 800 ºC.

iv) Photolithography to define the Pt strips: The process consists in spinning the positive photoresist and use of Cr masks to mark the appropriate patterning. Then, a 100 nm thick Pt layer is deposited, and the photoresist is lifted off to define the Pt strips. To enhance the adhesion of Pt with the oxide/nitride a layer of Ti 10 nm thick is deposited before the Pt layer.

v) An annealing process is carried out at 600 ºC during 2 hours to stabilize the resistance of the Pt strips.

vi) By reacting ion etching (RIE) the backside SiN_X and SiO_2 films are removed.

vii) The backside of the Si wafer is etched using KOH 35% at 80ºC leaving around 5-10 µm of Si in contact with the $SiNx/SiO_2$ membrane.

viii) The wafer is cut in devices of 6 mm x 6 mm.

ix) The last 5-10 µm of Si are removed individually in each sensor by dropping KOH 40% at 60ºC during 2 hours.

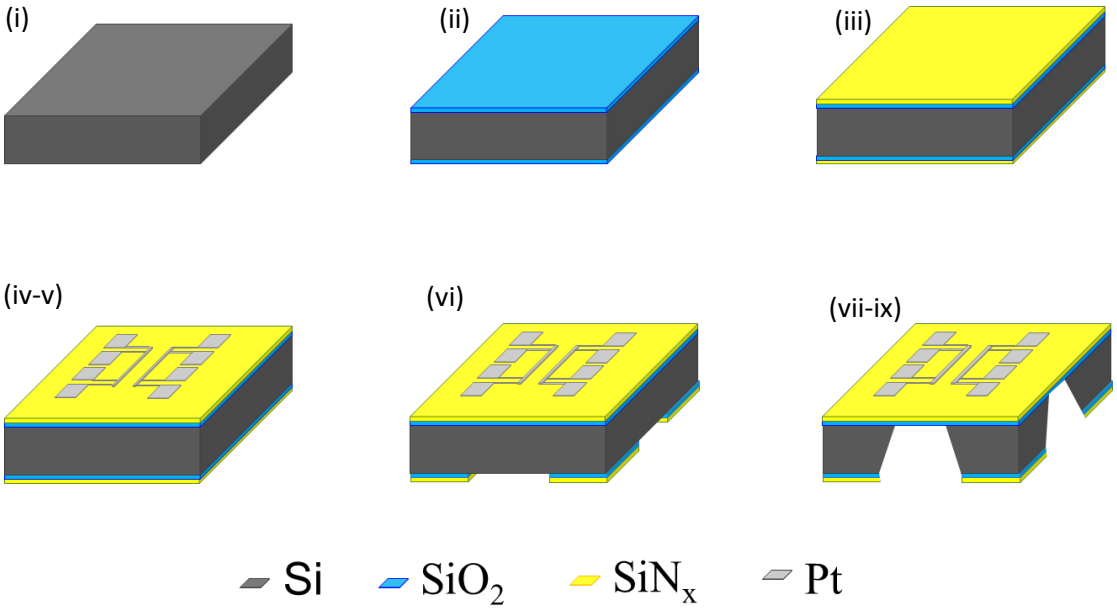

Figure 3.3 Microfabrication steps of the 3ω-Völklein sensor.

3.1.4 Thermal conductance

The relation between the thermal conductance and the temperature oscillations will be performed analyzing the propagation of heat in one dimension. This is an excellent assumption given the geometry of the device. The heater is a long strip located at the center of the rectangular SiN_x membrane (see schematic design in Figure 3.1). When the metallic strip is heated by the current there is a temperature difference build-up between the heater and the frame and heat flows perpendicular to the heat source. Assuming the film is isotropic in the plane of propagation the system can be considered as 1D, the heat equation can be simply solved and the thermal conductance evaluated. In DC mode:

$$G = (k_s t_s + k_m t_m)\frac{2L}{l} \tag{3.9}$$

where k and t are the in-plane thermal conductivity and thickness respectively, L is the length of the heater and l is the distance from the heater to the frame. The s and m subscripts refer to sample and membrane, respectively.

If the sensor is fed with an AC current, the analysis is more complex, but the 1D analysis remains valid due to the geometry of the sensor. As discussed by Sikora the solution for the $\Delta T_{2\omega}$ is very complex, but considering the Taylor expansion series and

getting the first order-terms of the expansion a simple solution can be reached as follows [50]:

$$\Delta T_{2\omega} = \frac{Q_0}{G\sqrt{1+(2\omega)^2\left(\tau^2+\frac{1}{3}\frac{l^2}{D}\tau+\frac{1}{6}\frac{l^4}{D^2}\right)}} \tag{3.10}$$

where τ is the characteristic time defined as the ratio between the heat capacity of membrane plus the sensor (Pt strip), $C' = c_m t_m \rho_m L\frac{w}{2} + c_{Pt} t_{Pt} \rho_{Pt} L\frac{w}{2}$, and the thermal conductance, G, $\tau = C'/G$. D is the thermal diffusivity of the membrane, $D = k/\rho c$. Applying equation 3.10 in equation 3.3.b we obtain:

$$G_{2\omega} = G\sqrt{1 + (2\omega)^2\left(\tau^2 + \frac{1}{3}\frac{l^2}{D}\tau + \frac{1}{6}\frac{l^4}{D^2}\right)} \tag{3.11}$$

Observing equation 3.11 it is possible to note that the apparent thermal conductance can reach values close to the real thermal conductance when $\omega \to 0$. Therefore, low values of frequency allow to obtain G measuring $G_{2\omega}$. Besides that, the characteristic time and the relationship between *l* and the penetration depth, $d = \sqrt{D/\omega}$ should be considered to obtain the apparent thermal conductance to values close to the real thermal conductance. The penetration depth is a parameter that describes the spatial damping of the thermal wave generated by the heater. Thus, if $d \gg l$ (or $\omega \ll {}^{D}/_{l^2}$) all heat generated by the strip will be dissipated through the membrane and when the frequency increases overly, part of heat will be dissipated in the dynamic heating due to lack of time to dissipate the heat through the membrane.

When a thin film is deposited on the membrane the values of the penetration depth and the characteristic time of the system change, therefore, the effective thermal diffusion coefficient should be rewritten considering the sample contributions:

$$D_{eff} = \frac{(k_m t_m + k_s t_s)(t_m + t_s)}{(\rho_m t_m + \rho_s t_s)(c_m t_m + c_s t_s)} \tag{3.12}$$

besides the values of *G* and *C'* should be rewritten as follows:

$$G(s) = (k_s t_s + k_m t_m)\frac{2L}{l} \tag{3.13}$$

$$C' = (c_m t_m \rho_m + c_{Pt} t_{Pt} \rho_{Pt} + c_s t_s \rho_s) L \frac{w}{2} \tag{3.14}$$

As explained before measurements should be performed at low frequencies to obtain values of $G_{2\omega}$ that approximate to G. In the case of the film deposition the deviation between the $G_{2\omega}$ and G increases significantly using high frequencies. As described earlier by Ferrando-Villalba *et al.* [55], the value of $G_{2\omega}$ is very similar to G during the deposition when the frequency is set at 1 Hz. Thus, in this work the 3ω-Völklein measurements are carried out at 1 Hz to ensure the apparent thermal conductance coincides with the real thermal conductance.

3.1.5 Electronics and measurement procedure

To achieve high sensitivity in the measurement of the in-plane thermal conductivity by the 3ω-Völklein method an electronic setup as shown in Figure 3.4 is necessary. Sensor and reference (potentiometer) are connected in series and fed with an AC current at low frequency (1 Hz) and amplitudes between 100 µA and 500 µA. The reference is a variable resistance that does not change its temperature and therefore does not produce a third harmonic voltage. It is used to cancel the first harmonic component of the sensor's voltage. The drop voltage at each element is measured by INA 114 amplifiers with gains of 3.28. The voltage signal of the reference is subtracted from the voltage signal of the sensor remaining only the third harmonic of the sensor signal. The 3ω component is also amplified with gain of 98.

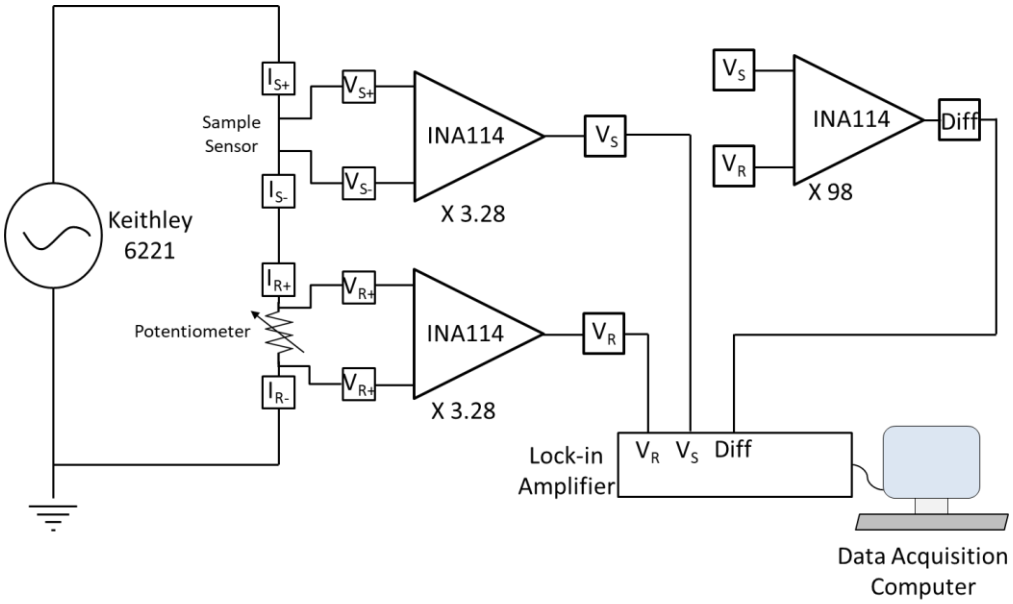

Figure 3.4 Scheme of the electronic setup used in 3ω-Völklein method.

The sensor, reference and the differential (V_S - V_R) voltages are measured with a digital build lock-in amplifier based on PXI 6124DAQ from National Instruments. Then, the voltage signal pass through Discrete Fourier Transform (DFT) by Labview software to get the amplitude and phase of ω and 3ω signals. Moreover, the signal to noise ratios are calculated by software and values higher than 10^3 are attained. Using the measured values in equations 3.3b, 3.8 and 3.13 the in-plane thermal conductivity can be obtained. As observed by Ferrando-Villalba et al performing in-situ measurements, the interface scattering (is) does not play an important role in the total thermal conductance, being around of 1.2 %. This percentage decreases as a function of the sample thickness, thus, the thermal conductance of the sample can be obtained measuring the thermal conductance of the membrane before the sample deposition, which is deducted from the thermal conductance of the sample plus membrane, yielding a thermal conductance of the sample $(G_s = G_{s+m} - G_m)$ [55].

As explained before the temperature coefficient of resistance (TCR) of the heater must be determined. Thereunto, a custom-built vacuum chamber is used to control the sensor temperature, which also reduces the heat dissipated by the surround. The vacuum chamber is equipped with three feedthroughs used as follows: electrical connections to temperature probes and control, electrical connections to sensor probes and a pipe to establish the temperature of the thermal bath. Figure 3.11 shows a picture of the vacuum chamber.

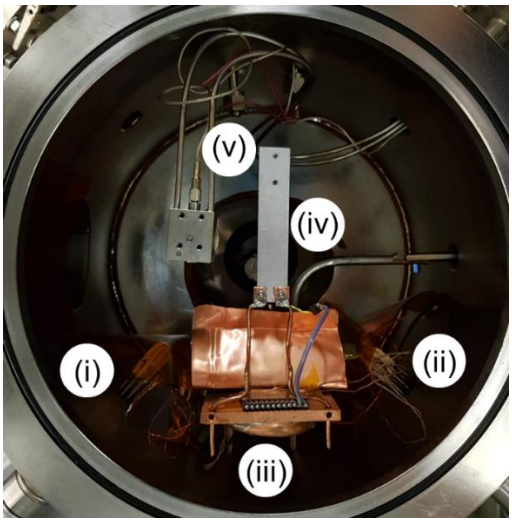

Figure 3.11 Picture of the vacuum chamber. (i) Feedthrough used to the sensor probes, (ii) feedthrough used to the temperature probes and control, (iii) feedthrough used to the thermal bath, (iv) Al plate and (v) Kapton heater.

The temperature control is achieved using the following steps: a commercial cooling circulator is connected by pipe feedthrough and establishes the temperature of the thermal bath, from -20 ºC to 30 ºC. The thermal bath temperature limits the minimum temperature of the system could reaches. The thermal bath is connected to aluminum plate through copper rods ensuring the thermal link between them. The Al plate is where the socket of sample will be collocated. Then the thermal bath temperature is established, a commercial Kapton heater beneath the Al plate and an A-type PT100 located in socket of the sample are used to control the temperature by homemade LabView PID software. This temperature control system permits to establish the temperature from 260 K to 380 K with fluctuations smaller than 0.005 K. By feeding the thermal bath with liquid nitrogen is possible down the system to temperatures around to 90 K.

3.2 Electrical conductivity and Seebeck coefficient measurements

The electrical conductivity and Seebeck coefficient are important parameters to characterize a thermoelectric material. We have designed and fabricated a measurement device, to obtain the electrical conductivity and the Seebeck coefficient of thin films deposited by several techniques.

3.2.1 Measuring system

The structure used to perform the Seebeck coefficient measurements is based on two Peltier cells that are employed to generate a temperature difference across the thin film. The Peltier cells are mounted on a Cu block as shown in Figure 3.5. They are connected in series with the polarity reversed so as one side heats and the other cools. The temperature difference was initially measured by two PT100 resistances glued to the Cu blocks that are on the Peltier cells. However, this geometry produced an error in the Seebeck coefficient because the temperature difference measured by the PT100 resistance was not the real temperature difference applied to the sample. To avoid this uncertainty, we have developed a new probe/device with thin-film Au strips in 4-wire configuration to measure the temperature at the same zone where the Seebeck voltage is measured. The Au strips are previously calibrated and used as thermometers. The ratio of the Seebeck voltage and the temperature difference (Eq. 2.25) for a range of ΔTs gives the Seebeck coefficient of the material. To guarantee a good electrical contact of the thermometers and the Seebeck voltage probes pogo pins were used. Figure 3.5 shows the scheme of the structure used to measure the Seebeck coefficient and the probe with the metal thermometers and the Seebeck electrodes.

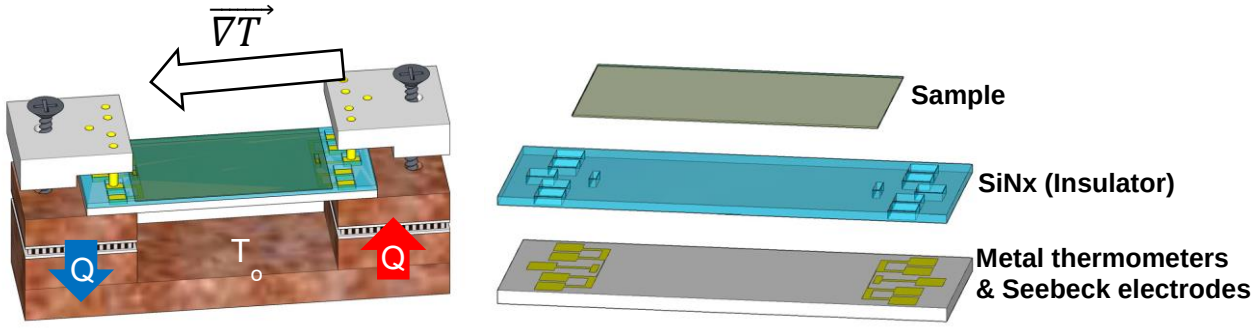

Figure 3.5 Scheme of the structure and device used to measure the Seebeck coefficient.

To verify the maximum and minimum temperature attained at the hot and cold junctions and to characterize the overall structure, the temperatures at both sides were measured using the previously described probe. Besides, the Cu structure is placed in the high vacuum chamber described previously in section 3.1.5, which permits to maintain the base temperature (T_0, see figure 3.5) during the measurements at 300 K. Figure 3.6 shows the temperature at the cool and hot sides of the device when the Peltiers are fed with different currents. The temperature differences between both sides is also shown.

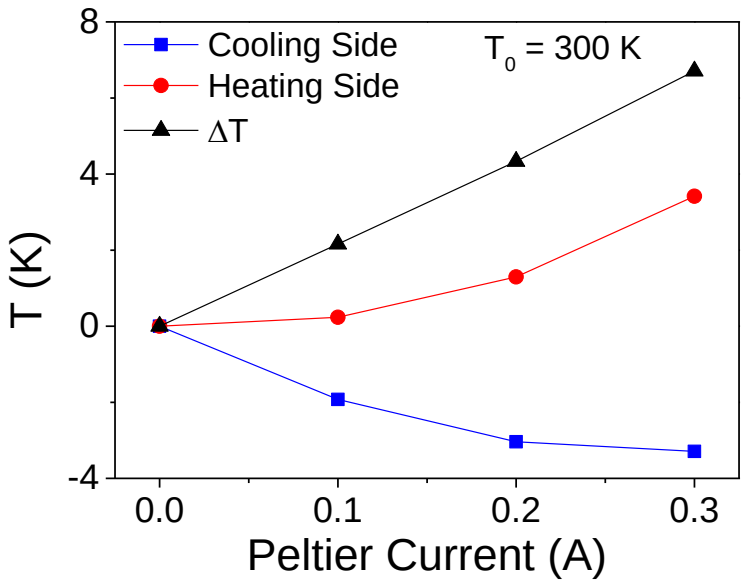

Figure 3.6 The cooling and heating side temperatures as a function of the Peltiers currents.

Figure 3.6 shows that temperature differences up to 6.5 K can be achieved by applying 300 mA to the Peltier cells. In addition, ΔT follows a linear behavior with the Peltier current.

The system described above was used in the electrical conductivity and Seebeck coefficient measurements of $MgAg_{0.95}Ni_{0.005}Sb_{0.99}$ and PEDOT:PSS thin films. Due to the different deposition processes between the polymeric samples and $MgAg_{0.95}Ni_{0.005}Sb_{0.99}$ samples, the substrates of the devices in the case of polymeric materials were Pyrex glass while the $MgAg_{0.95}Ni_{0.005}Sb_{0.99}$ samples were deposited on devices fabricated on Si substrates.

3.2.2 Microfabrication of the Seebeck coefficient sensor

As explained before for these measurements the samples were deposited on a device that permits to measure the voltage generated and the temperature difference. This device was fabricated both using 4-inch Si or Pyrex wafers. The microfabrication procedure corresponding to the Pyrex substrate is outlined below. Schematics designs of the steps are shown in Figure 3.7.

i) The process begins with a 4-inch Pyrex wafer.

ii) 100 nm thick Au contacts and thermometers are deposited by electron-beam physical vapor deposition (EBPVD) and are patterned by photolithography process and liftoff. For a good adhesion 10 nm thick Cr was deposited before the Au film.

iii) The insulation film of low thermal oxide (LTO) with 200 nm of thickness was deposited using Low pressure chemical vapor deposition (LPCVD).

iv) The open via process is performed by photolithography and wet etching in the thermometers' pads and the Seebeck voltage probes.

v) The wafer is cut in devices 21 mm x 11 mm.

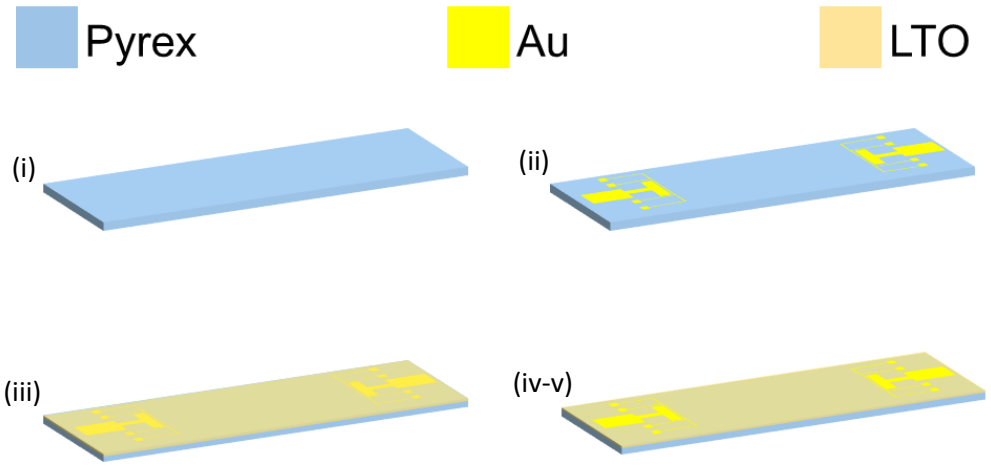

Figure 3.7 Scheme of the microfabrication processes of the device.

As explained before, the device can also be microfabricated using the 4-inch Si wafer, for this, a 180 nm thick SiN_X film is deposited before the Au deposition, this additional step is achieved to isolate electrically the Si substrate and the metal strips.

3.2.3 Seebeck coefficient measurements

To achieve a better control of the base temperature, the measurements were carried out in a high vacuum chamber with a PID system that ensures keeping constant T_0 during the application of the temperature gradient. The operating system of the vacuum chamber will be discussed in Section 3.4. As already mentioned above the Peltier cells are connected in series and the DC current flows through the two cells that are in reverse polarization, in such a way that a Peltier cell will increase the temperature at the surface in contact with the device while the other will decrease the temperature establishing thus the temperature difference between the two extremes of the sample. The thermometers used to measure the temperature of the sample at both sides were previously calibrated. The calibration procedure consists in measuring the electrical resistance of the Au strips at several temperatures close to 300 K, then the temperature coefficient of resistance (TCR) is obtained. This procedure is similar to the calibration of other heater/thermometers along the thesis and will be discussed with more details in Chapter 4 for the PTE device. The Seebeck voltage build up due to the temperature gradient is measured with a nanovoltmeter Keithley 2182a. This procedure is performed for three temperature differences and the slope of the curve is used to determine the value of *S*. Figure 3.8 presents Seebeck voltage at open circuit of the PEDOT:PPS doped with 2% of DMSO as a function of the temperature difference and the Seebeck obtained by the slope of the curve.

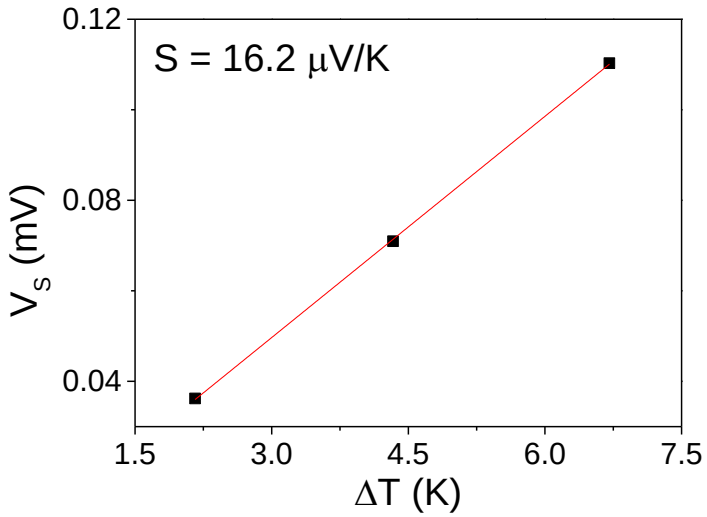

Figure 3.8 Seebeck voltage at open circuit of the PEDOT:PPS doped with 2% of DMSO as a function of the temperature difference. The error bars are smaller than the symbols.

3.2.4 Electrical conductivity measurements

The electrical conductivities of the materials were measured using the same structure without imposing a temperature gradient. *IV* measurements are carried out and to avoid the self-heating contribution the resistance is acquired by the extrapolation the voltage to zero current. Using the sample resistance and its length, width and thickness the electrical resistivity is evaluated by $\rho = \frac{RA}{L}$, where R is the resistance of the sample, $A = td$ is the cross-section area, thickness (t) multiplied per the width (d) and L is the length of the sample. As $\sigma = \rho^{-1}$, the electrical conductivity of the sample can be determined. The values of length and width are imposed by the measuring probe/device while the sample thickness is measured using a KLA TENCOR P7 profilometer.

4. Photothermoelectric effect in Si thin films

As explained in Chapter 2, the photothermoelectric effect (PTE) combines the photovoltaic and thermoelectric effects. PTE was first studied by Tauc, who discussed the changes in the thermoelectric voltage of Ge single crystals when illuminated [56]. The concept used to explain these changes did neither consider the photovoltaic effect nor the influence of this effect on the phonon drag contribution to the Seebeck coefficient. Afterwards, a more generalized analysis was performed by van der Pauw and Polder by considering that the photovoltaic effect affects the phonon drag contribution [57]. In the same way, a study of the PTE effect in *n*-*p* doped bulk Si was realized by Haper et al [58] in a wide temperature range. They observed a rise of the Seebeck coefficient in *p*-type Si at some temperatures when the photocarriers are generated. This behavior was not expected since the increase of charge carriers increases the electrical conductivity, which should decrease the Seebeck coefficient (*S*) (Eq. 2.23). A complementary study by the same authors was performed posteriorly and reported that this unexpected behavior was probably due to an experimental artifact [59].

Afterwards, some later studies focused their attention in the power factor ($PF = S^2\sigma$), since the rise of the electrical conductivity could lead to an increase of *PF* even if the Seebeck coefficient decreases. Mondal et al. studied the PTE in a PbO single crystal and observed a significant rise in the *PF* value despite the *S* reduction due to the significant amount of charge carriers generated by light [60]. In the same way, other works performed in the last decade present interesting results using photocarriers to increase the PF [61,62]

As related by Ling Xu, the photoinduced excited states generated by light could enhance the Seebeck coefficient in MEHPPV (poly(2-methoxy-5-(2′-ethylhexyloxy)-p-phenylene vinylene) devices [63]. The same behavior was also noticed by Hu et al. in a study with polymeric semiconductor films [44]. Recently, organic-inorganic hybrid perovskite (CH3NH3PbI3) showed also an improvement of the Seebeck coefficient induced by photocarriers [64]. Therefore, this mechanism provides a new way to boost *ZT*, enabling the enhancement on *S* and σ, simultaneously, in thermoelectric devices.

The photothermoelectric effect, based on the simultaneous temperature rise and enhancement of the Seebeck coefficient of the thermoelectric material through carrier

injection, converts temperature differences induced by the absorbed light to electric voltage. Compared to other photodetection mechanisms, i.e., photovoltaic, photoconductive and bolometric, the PTE effect allows improved detection over a broadband without external bias at room temperature (RT) [65]. The PTE effect has drawn some attention in 2D materials such as graphene, MoS_2, black phosphorus and topological insulators[66]. In those materials the responsivity is related to the light-induced temperature gradient and the material's Seebeck coefficient.

In this chapter, the photothermoelectric effect in Si thin films is explored. The photoresponse of a membrane-based μTEG of small dimensions was verified and its use as photosensor demonstrated. Using a laser beam as heat source, the response time of the device was shown to be fast due to the very small thermal mass of the device. During these measurements, an unexpected improvement of the Seebeck coefficient was observed as a function of the laser power. In order to verify the variation in the Seebeck coefficient, a new device (PTE device) was designed and developed to conduct a focused analysis of the photothermoelectric effect in Si (ultra)thin films. Measurements performed with the new PTE device confirmed the modification of the Seebeck coefficient caused by the injection of photocarriers and the simultaneous large temperature gradients generated by the laser beam and the resistive heater. Besides that, the laser beam also produced an increase of the offset of the open-circuit voltage.

4.1 Microthermoelectric generator device

The device that motivated the study of the photothermoelectric effect in Si thin films is a microgenerator based on a Si thin membrane [67]. The device consists in 40 thermoelectric legs (20 n and 20 p) connected thermally in parallel and electrically in series, as shown in figure 4.1. The thermoelectric legs have a doping level of $6.5x10^{18}$ cm^{-3} for p-type Si and $2x10^{19}$ cm^{-3} for n-type Si, and are connected electrically in series, leading to an internal resistance of ~ 62 KΩ. Due to the thickness reduction of the thermoelectric legs, 100 nm thick Si, the thermal conductivity of Si decreases from 150 W/mK for bulk silicon at room temperature down to 60 W/mK, as reported elsewhere [68], due to phonon scattering at surfaces/interfaces [69–73]. On the contrary, the Seebeck coefficient remained close to expected values for bulk Si with similar doping levels (~5×10^{19} at/cm^3) [36,74]. The *p,n* Si legs support the SiN_X membrane mechanically to the frame and on the top of the membrane there is a Pt grid, which permits a full

thermoelectric characterization of the device. The central Pt grid can be used as heater and/or thermometer. To use the Pt grid as a thermometer, the temperature coefficient of resistance (TCR) is previously obtained by extrapolating the *I*x*R* measurements to zero current at several temperatures close to measuring range, this extrapolation is performed to avoid the self-heating contribution, as briefly explained in Section 4.2.3. When current is injected in the Pt grid its temperature increases by Joule heating producing a temperature difference between the center and the frame of the device that is used to evaluate the thermoelectric properties of the TE Si legs. Figure 4.1 shows the optical image of the device highlighting the various elements of the device: TE legs, Pt grid and Pt pads.

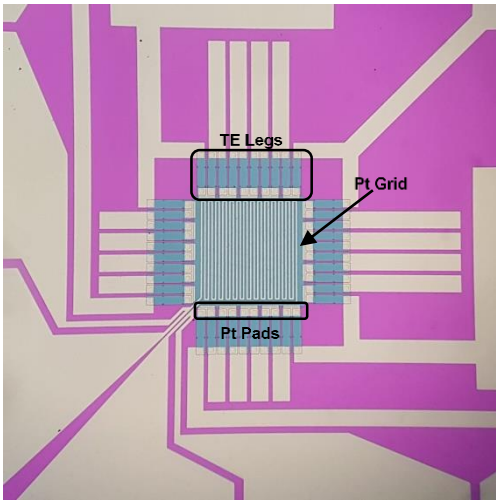

Figure 4.1 Optical image of the microthermoelectric device.

Microthermoelectric generators can be used as photosensors. The great advantage of these devices in relation to bolometers is the absence of the current or voltage source for its operation. As the device studied in this work is based on a thin Si membrane, a reduction of the thermal mass is achieved with a concomitant reduction of the response time, enabling fast photodetection response.

4.1.1 Temperature profile corrections

Due to the non-flat temperature profiles generated during the experiments, FEM corrections are required. The correction consisted of establishing a relationship between the average temperature measured by the platinum grid (heat source and/or thermometer) and the average temperature at the hot junction (Pt pads) of the thermoelectric Si legs (see Figure 4.1). Based on this analysis a correction factor is calculated and used to obtain the

real temperature gradient on the thermoelectric Si legs. For the illuminated device, the additional heating caused by the absorbed light must be also considered in the simulations due to local changes in the temperature distribution. Therefore, the power of the light is considered as a supplementary heat source and the absorption coefficient of each element of the device is used to estimate the amount of heat absorbed from the laser beam. Figure 4.2a shows the temperature as a function of the position from the center of the device in each case, in dark conditions and when the device is illuminated by an Ar^+ laser at 457 nm operating at 1 mW, 5 mW and 9 mW. It is clear that temperature increased and the temperature profiles changed due to the incident radiation. It is also important to note that the shape of the temperature distribution changed with the different power of the incident light. The temperature map of the whole device simulated by FEM is shown in Figure 4.2b.

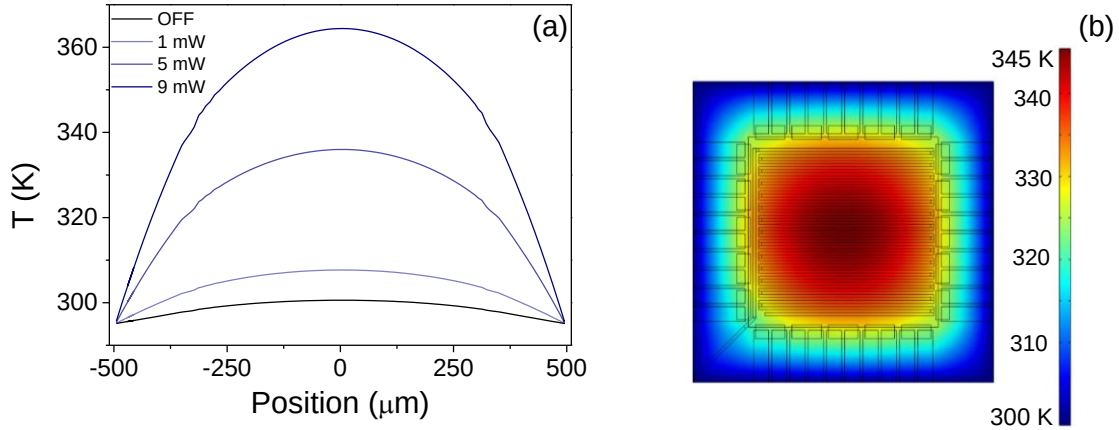

Figure 4.2 (a) Temperature as a function of the position from the center of the device. **(b)** The temperature profiles of the device simulated by FEM.

The correction of the temperature drop in the thermoelectric legs was carried out as follows: First, the mean temperature of the platinum grid ($\overline{T_G}$) was calculated using the FEM results. Then, the mean temperature in the platinum pads ($\overline{T_P}$) at the hot junction was evaluated using the FEM results, thus allowing the calculation of the correction factor using:

$$f = \frac{\overline{T_G} - T_S}{\overline{T_P} - T_S} \tag{4.1}$$

with T_S being the substrate temperature. The values of the correction factor for the illuminated device changed as a function of the temperature rise generated by the

platinum grid, from 1.39 to 1.64, increasing as the temperature gradients becomes larger. In dark conditions, this factor remained almost constant at 1.66. Thus, the real temperature difference applied to the thermoelectric legs was obtained by dividing the temperature difference measured experimentally by the correction factor.

4.1.2 Microfabrication of the µTEG device

The µTEG was microfabricated using a 4-inch high quality SOI (SOITEC, France) following the steps:

i) The Si device layer is reduced to 100 nm by wet oxidation and subsequent HF etching.

ii) The Si top layer is patterned by photolithography using bright field (BF) and etched with reactive ion etching (RIE). These processes define the thermoelectric Si legs $(50\mu m \times 150\mu m)$ and a central squared undoped silicon region $(500\mu m \times 500\mu m)$

iii) The 50 nm thick SiNx layer is grown by low pressure chemical vapor deposition (LPCVD) at 800 ºC.

iv) RIE is done on the backside of the SiN_x layer to open window.

v) The *n,p* type legs are defined using photoresist masks and sequential implantation of Phosphorous, Boron, respectively.

vi) A rapid thermal annealing process at 900 ºC is carried out to activate the dopants and to recrystallize the Si thin film as a single crystal. This is possible since the dose and energies of the implantation procedure are calculated as to leave a thin unimplanted region at the bottom of the thin film. This layer serves as a seed for the recrystallization process.

vii) Open via at the top of the SiNx layer by RIE to permit the contacts between the Si TE legs and the metal.

viii) A 50 nm thick Ni layer is grown by sputtering, followed by a thermal treatment at 300 ºC to form the NiSi and to guarantee an ohmic contact with low resistivity between the TE legs and the metal.

ix) 100 nm thick Pt metal lines and contacts are defined by photolithography and deposited by e-beam.

x) A wet etching of the backside is performed to leave the central Si platform suspended. This step was attained by etching with KOH until around 5-10 µm of Si bulk to improve the “survival” of the membrane.

xi) The wafer is cut in devices 6 mm x 6mm.

xii) The last micrometers of Si bulk that remained are finally removed individually by dropping 5 µL of KOH in the backside during 1 hour at 70 ºC.

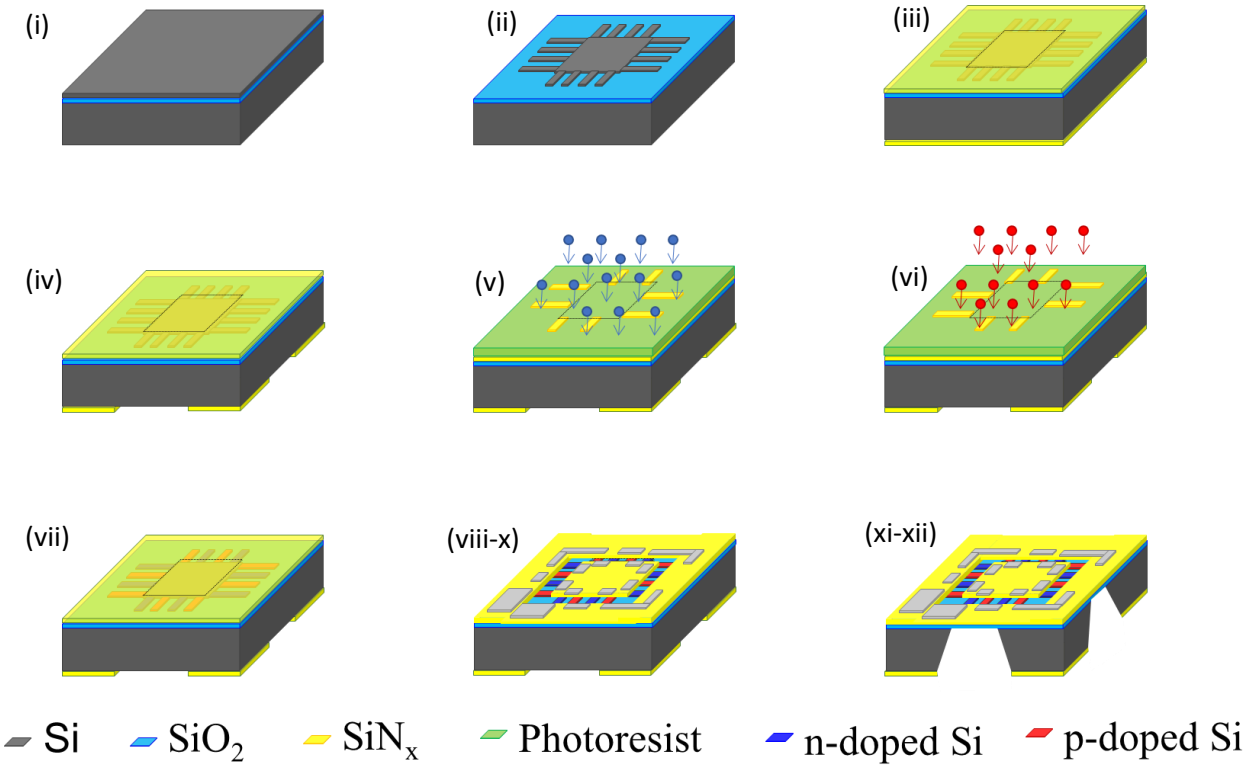

Figure 4.3 Microfabrication steps of the µTEG device.

4.1.3 Measurement procedure

The Seebeck open-circuit voltage measurements were performed using an Ar^+ laser as excitation light at 457 nm operating from 0 to 10 mW in air at atmospheric pressure. The incident light was collimated using an objective lens, permitting to control the position of the incident beam, what is important to ensure the complete illumination of the TE legs. The scheme of the device showing the illuminated zone is presented in Figure 4.4.

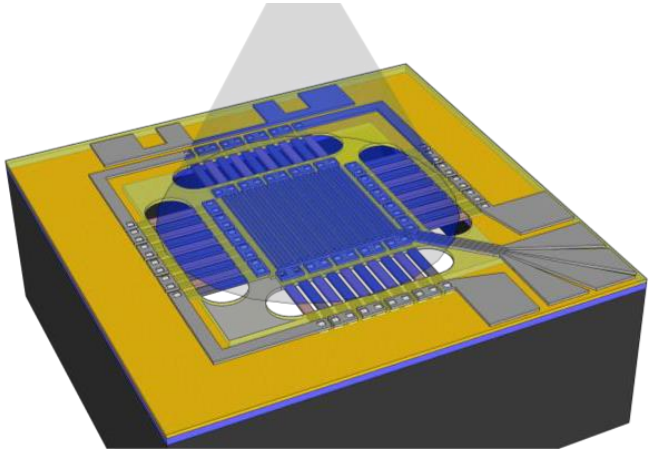

Figure 4.4 The scheme of the device with the zone illuminated by the laser beam.

4.1.4 Measurement of Seebeck coefficient

The device was used to carry out measurements of the open circuit voltage and the temperature difference between hot and cold sides while illuminated by an Ar^+ laser operating from 0 to 10 mW at 457 nm with spot diameter of $\sim 0.5\ mm$. The temperature difference is generated by the Pt heater at the center of the membrane, but the laser beam also produced an additional temperature increase, as discussed before. Therefore, for each incident power of the laser beam the open-voltage was measured as a function of the temperature difference (generated by heater). The slope of $V_S \times \Delta T$ curves (see Figure 4.5a) yields the Seebeck coefficient of the TE legs that was determined as a function of the laser power. Figure 4.5b shows the overall Seebeck coefficient of all the TE legs (connected in series) of the device versus the laser power.

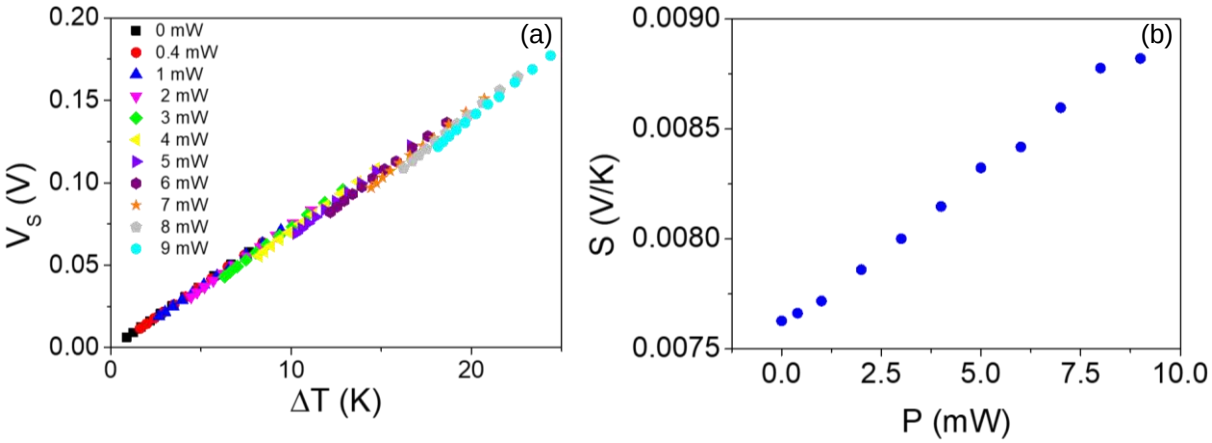

Figure 4.5 (a) Seebeck voltage at open circuit as a function of the temperature difference. **(b)**: Seebeck coefficient of TE legs of the device as a function of the laser power.

Interestingly, Figure 4.5b shows an unexpected increase of the Seebeck coefficient as the laser power increases. Despite the fact that the temperature difference generated in dark and illumination conditions occurs in a slightly different range, the increase of the Seebeck coefficient when the device is illuminated amounts to around 15%, from 7.6 mV/K in dark to 8.85 mV/K at the maximum laser power of 9 mW. Since the device consists on 40 *n* and *p* legs the average Seebeck coefficient per leg is 190 μV/K in dark and 220 μV/K at 9 mW of laser power. The enhancement of the Seebeck coefficient can not be associated with the increase of the average temperature due to the incident laser beam. On the contrary, Geballe and Hull observed the opposite effect, *S* decreased in bulk Si, both in doped and non-doped Si, with increasing temperature [33]. As already pointed out the improvement of *S* was surprising since injection of charge carriers in a bulk thermoelectric material should lead to a reduction of the Seebeck coefficient. For bulk Si this decrease was measured and discussed by Harper et al [58]. However, we do not know about measurement of the photo-thermoelectric effect on (ultra)thin Si layers under large temperature gradients. Possible reasons for the observed enhancement will be discussed in section 4.2.

4.1.5 Thermoelectric photosensor based on ultrathin single-crystalline Si films

During the previous measurements the photoresponse of the device was also evaluated to investigate the potentiality of the device as a photosensor. Photosensors are sensors able to detect light (electromagnetic waves). Depending on the desired spectral sensitivity different physical principles should be considered. Between sensors using semiconductors as active materials we can highlight those directly working from [75–78]:

(i) photoelectric or photovoltaic effects, when the photons have energies over the semiconductor band gap.
(ii) thermal-based absorption sensors when the photon energies require the generation of mid-gap states providing energy to the phonon bath.

Thermal detectors, either bolometers or thermoelectric-based, have a broad spectral range of detection and rely on the temperature increase produced by the absorbed radiation. Among the wide family of thermal absorption photosensors those based on the TE principle do not require an external current or voltage source, and therefore may offer extremely low energy detection limits depending on designs. In general, thermal detection is preferred over photon detectors for applications involving small excitation energies.

Strategies to enhance the efficiency of thermoelectric detectors entail the improvement of the thermoelectric performance of the materials by maximizing its power factor. In addition, low heat capacities per unit area and low thermal conductances are required to attain high temperature differences upon radiation absorption. Higher ΔT implies higher sensitivities. One way of achieving this goal is to use ultrathin highly doped Si layers as active elements of the n,p thermoelectric materials. It has been previously shown that reducing the dimensionality of Si can boost its thermoelectric performance reaching for small diameter Si nanowires $ZT = S^2\sigma T k^{-1}$ values close to 1 at 300 K due to their reduced thermal conductivity close or even below the amorphous limit [36,74]. Similar achievements can be obtained using ultrathin Si membranes where enhanced scattering with the membrane surface dramatically affects the lattice thermal conductivity [69,70]. Additionally, appropriate designs and materials can be used to boost absorption at of the sensing/absorbing regions. As an additional feature, the simplicity of these type of devices enables their miniaturization.

Figure 4.6 shows the open-circuit voltage generated in the TE legs as a function of the laser power using a fixed power in the heater of around 0.23 mW. The linear increase of the voltage, V_S, is due to the temperature difference induced by the laser beam between the central region and the silicon frame (black circles). The responsivity, R_S, of the TE sensor, defined as the ratio between the output voltage and the absorbed power, is determined by the slope in Figure 3. R_S amounts to 13 V/W and, considering the small area of the device, yields an outstanding value of 2.6×10^7 V/Wm^2 in air.

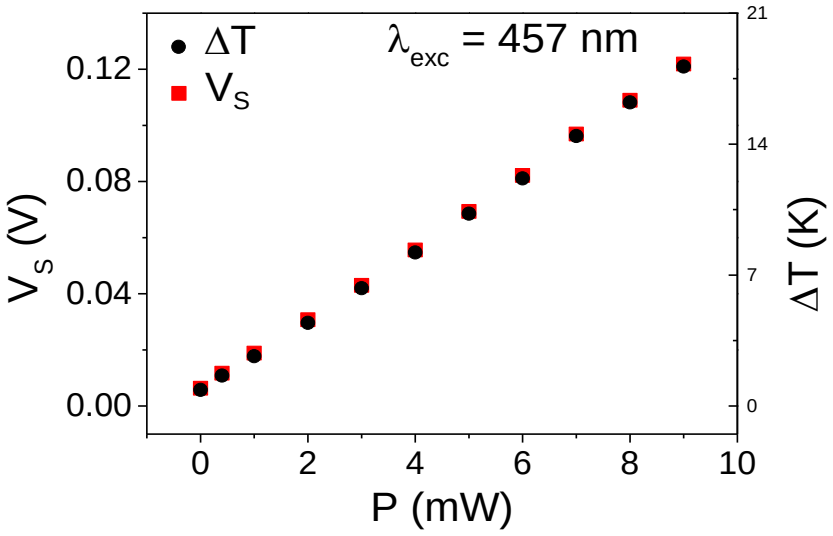

Figure 4.6 Plot of the voltage at open circuit and temperature difference as a function of laser power.

To verify the device's response to oscillating light, we used an experimental setup with a homemade optical chopper system that allowed to measure the Seebeck voltage and the grid resistance, R_G, while the light beam was chopped from 34 Hz to 239 Hz. An Ar^+ laser was used as light source at 457 nm operating at 5 mW. Figure 5 shows the Seebeck voltage and the grid resistance measurements carried out at 34 Hz and 239 Hz. The Seebeck voltage and the grid resistance oscillate as a function of the chopping frequency due to the temperature differences caused by the laser light. Both V_S and R_G present the same behavior at the several frequencies used in this experiment. Furthermore, it was verified that the sensor can measure oscillations of light at least until 239 Hz. This value was limited by our experimental setup, therefore it is expected that the device will be able to efficiently measure variations in a higher frequency range. By fitting the voltage curve in Figure 5(a), it was also possible to determine the thermal time constant of the device, which is ~4 ms. The detectivity is evaluated through the relation $D^* = R_S \cdot \sqrt{A/4kTR}$ [79–81], where R_S is the responsivity, A the area of the device, k the Boltmann constant, T the temperature and R the internal resistance of the device. $D^* = 2.86 \times 10^7\ cmHz^{(1/2)}W^{-1}$ which considering the reduced thermal constant of the device compares nicely with other thermoelectric-based CMOS-compatible sensors [79].

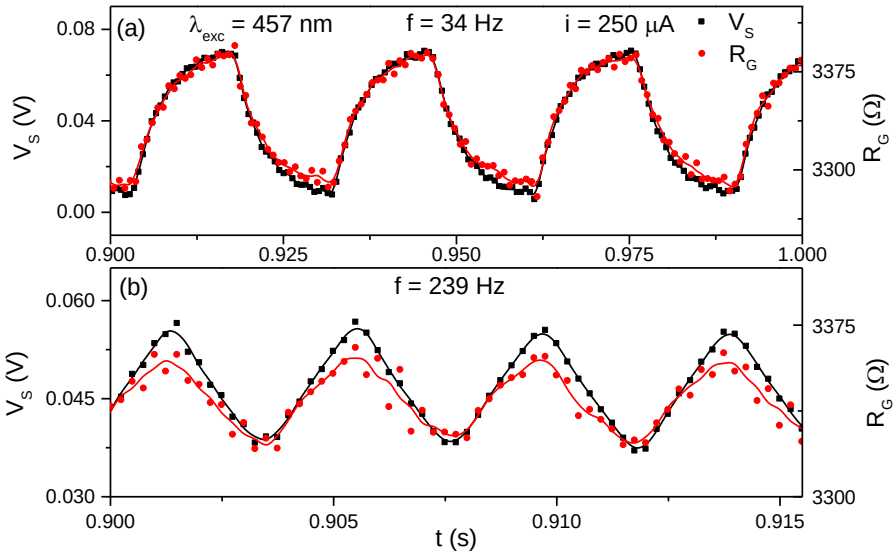

Figure 4.7 Open-circuit voltage (left axis) and grid resistance (right axis) measured while the light was chopped at 34 Hz **(a)** and 239 Hz **(b)**. Red and black lines are guides to the eye.

4.2 Photothermoelectric device

To further investigate the variation of the Seebeck coefficient during intense light irradiation we designed and microfabricated a new device. This new device avoids the complex temperature profile of the previous design (Figure 4.2b) and integrates additional temperature sensors to monitor temperature at various locations.

The new photothermoelectric device was based on the Völklein geometry to obtain a linear heat flux at the sensing zone and a flatter temperature profile. In a first step, the device was modeled via Finite Element Modeling (FEM) in COMSOL Multiphysics to verify the suitability of the generated heat flux and Seebeck voltage (see section 4.2.1.). The device consists on a free-standing membrane of $SiNx/SiO_2$ on top of which two heavily doped Si thermoelectric legs (*p* and *n* type) are defined. To independently measure the Seebeck voltage generated in each thermoelectric leg a Pt strip was deposited on top of the union between the *p* and *n* legs. Beyond that, on the outer Si edge two Pt pads were deposited permitting to measure the Seebeck voltage (Figure 4.8b). The Pt pads disposed on the edge are also responsible to guarantee the thermal link between the TE legs and the frame. To ensure the ohmic contact between the Pt and Si legs, 20 nm of Ni was deposited and annealed at 350ºC to form the NiSi. On this first level a SiN_X film was deposited with 450 nm of thickness insulating the contact used to measure the voltage and the Pt strips employed as temperature probes, as well as, the heater strip. Then, on the top of the SiN_X film a Pt strip used as a heater was deposited in the center of device and two additional Pt strips were deposited to measure the temperature on the extern border of Si. These Pt strips have 4-wire configuration and 155 nm (5 nm Cr and 150 Pt) of thickness. The devices were fabricated with several configurations in relation to the distance between the contacts and thickness of the Si legs. The length of the Si legs variated from 75 µm to 450 µm, the aim of the different distances between the electrical contacts being to observe if shorter distances, i.e. larger temperature gradients, influence the role of the photocarriers in the generated Seebeck voltage. The legs were microfabricated with 3 different thickness: 100 nm, 300 nm and 450 nm. Thickness may influence both the amount of photoinjected carriers since absorption is proportional to the thickness and the recombination and/or scattering process at the surfaces/interfaces of the TE legs that will increase as thickness is reduced. Thickness can thus play a significant role in the lifetime of the carriers, that is in the distance travelled by the charges before recombination or in the amount of charges

arriving to the electrical contacts. A scheme of the device and the optical image of PTE device with a zoom of the central area are shown in Figure 4.8.

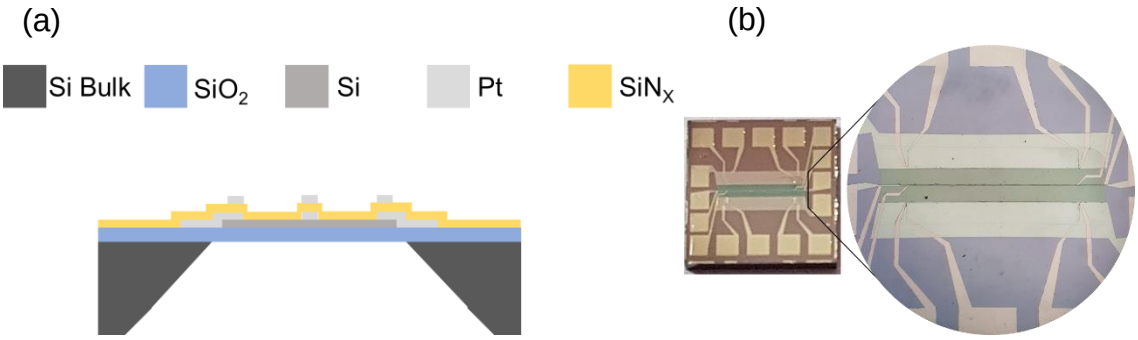

Figure 4.8 A scheme **(a)** and the optical image **(b)** of PTE device zoomed the central area.

4.2.1 FEM simulation of the PTE device

To ensure the linearity of the heat flux and the possibility to measure with certainty the Seebeck voltage in the PTE device, COMSOL Multiphysics was used to model the temperature and voltage drops across the device. COMSOL Multiphysics is a software based on Finite Element Modeling (FEM). The simulation was performed for a specific device: *p*-type Si with a carrier concentration of 6.5×10^{18} cm^{-3}, 100nm thick and distance between the contacts of 400 µm. To save computational cost part of the frame, the Pt pads, SiN_X insulation film and the thermometers were not considered in this simulation. Furthermore, the heater in the simulation was made of gold, but this is not especially relevant for the results and discussion. Figure 4.9 shows the temperature profile modelled and the temperature profile at the heater and the border with COMSOL. The temperature and voltage probes are located on the heater (at the center of the membrane) and on the border of the Si leg.

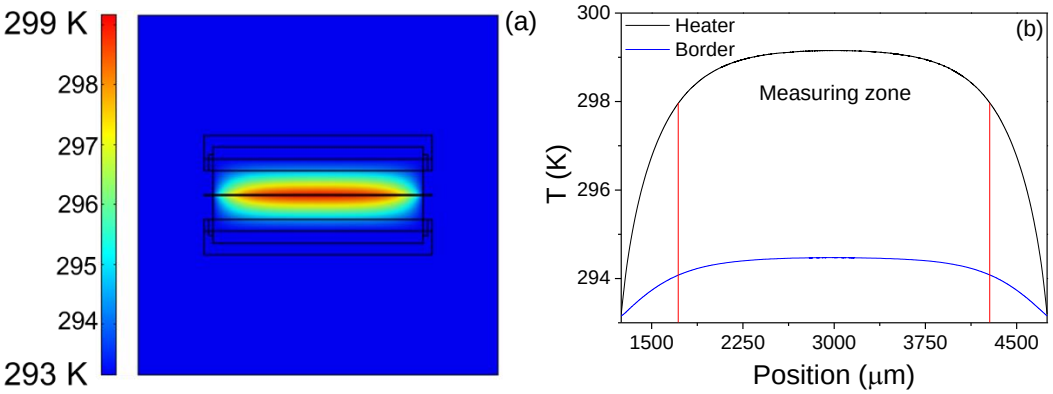

Figure 4.9 (a) The temperature profile of PTE device and **(b)** temperature profile at the heater and at the border. The red lines indicate the measuring zone.

The values of electrical and thermal conductivities of each material used in the simulation are described in Table 4.1. The Seebeck coefficient of the Si leg was considered as being 200 μV/K, which is the value for Si with carrier concentration close to 10^{19} cm^{-3}. Besides, the power injected on the heater was 2 mW.

Table 4.1 The properties of the materials used in the FEM simulation.

Material	*k* (W/mK)	σ (S/m)
SiO_2	1.41	$1x10^{-10}$
Au	109	$1{,}6 \cdot 10^{5}$
Si doped	43.4	$8{,}3 \cdot 10^{3}$
Si undoped	55	35,7

FEM simulation confirmed that, in this design, a linear heat flux will be produced in the center of the device (measuring zone), as shown in Figure 4.9b. The other aim of this simulation was to verify the values of the temperature differences and output voltage for a given input power to adapt the measuring instrumentation. The simulated values of the temperature and Seebeck voltage were 4.42 K and 826 μV, respectively. Voltage measurements will be carried out with the nanovoltmeter Keithley 2182a.

4.2.2 Microfabrication of the PTE device

The PTE device was fabricated using a 4-inch high quality SOI (SOITEC, France) wafer and the steps of microfabrication are described with more details below:

i) The single-crystalline Si top layer on top of the buried oxide (box) is reduced to 450 nm, 300 nm or 100 nm by oxidation and chemical etching of the SiO_2 with HF.

ii) Bright field (BF) photolithography and reacting ion etching (RIE) define the Si legs.

iii) A 50 nm thick SiN_X film is deposited on the two surfaces (top and bottom) using low pressure chemical vapor deposition (LPCVD) at 800 ºC.

iv) Dark field (DF) photolithography is performed to protect the *p* type legs, and the Phosphorous ion implantation is achieved defining the *n* type Si leg.

v) DF photolithography is performed to protect the *n*-type legs, and the Boron ions are implanted to obtain the *p*-type Si leg.

vi) A rapid thermal annealing process at 900 ºC is carried out to activate the dopants and to recrystallize the disordered Si film. The same procedure outlined in section 4.1.2. is used here.

vii) DF photolithography and RIE to the SiN_X film is performed to open via for the ohmic contact between the electrical contacts and Si legs.

viii) A 20 nm thick Ni layer is grown by sputtering, then the photoresist is removed. To guarantee the ohmic contact the wafer is annealed at 300 ºC to form the correct silicide phase.

ix) DF photolithography and 5 nm thick Cr and 150 nm thick Pt were deposited by e-beam and lift off was performed to define the electrical contacts.

x) An insulating film of SiN_X with 450 nm of thickness is deposited via plasma-enhanced chemical vapor deposition (PECVD), which avoids the electrical contact between the metallic contacts of the first and second level.

xi) DF photolithography and RIE attack the 450 nm SiN_X film to open via for the electrical contacts.

xii) The strips of Pt are defined following the same process of the steps vii and ix.

xiii) In order to open a window in the backside of the devices, an Al layer 400 nm thick is deposited on the backside to define a stopping mask for an ulterior deep RIE etching. Combining a DF photolithography to open a window in the

photoresist and etching the exposed Al layer with a wet etching, the SiNx surface is reached in the central window.

xiv) RIE is used to etch the 50 nm of the SiN_X membrane (step iii) and deep reacting ion etching (DRIE) using the Al mask to leave only 15 µm of Si bulk.

xv) KOH attack is realized using a SiN_x mask in the backside to remove the Al mask. To protect the device components a wax resistant to the KOH is deposited on the topside.

xvi) The wafer is cut in devices 6 mm x 6mm.

xvii) The last micrometers of Si bulk are removed in each device dropping 5 µL of KOH in the backside of the membrane during 2 hour at 70 ºC leaving only the SiNx/SiO_2 membrane in the center of the device

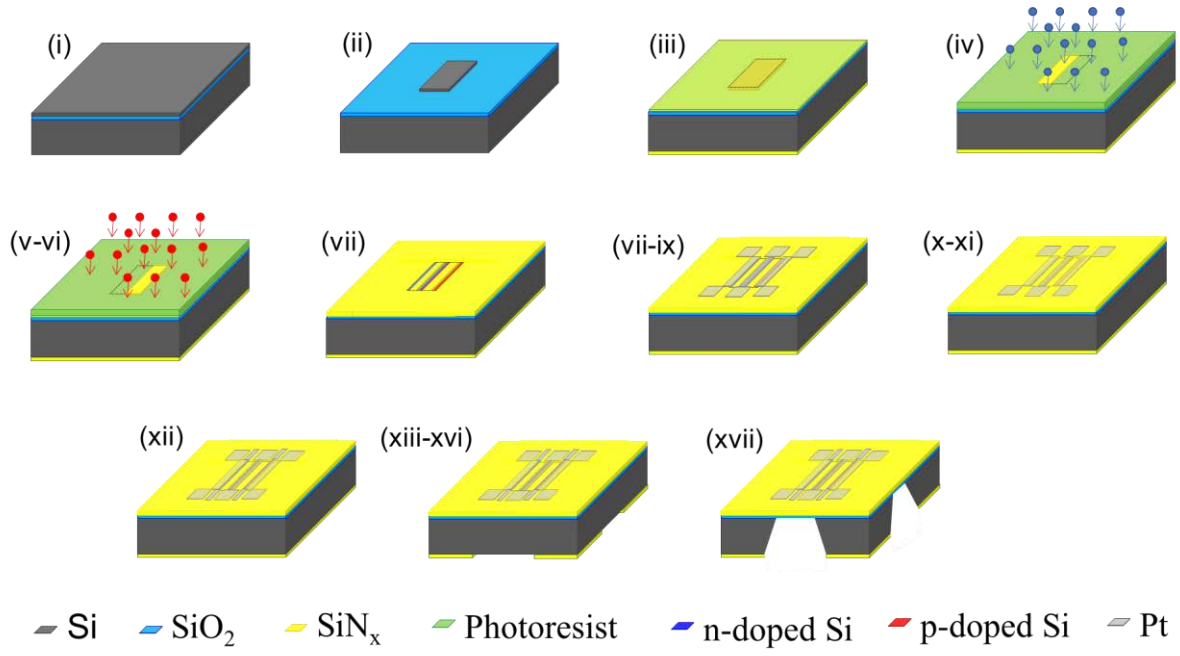

Figure 4.10 Microfabrication steps of the PTE device.

4.2.3 Calibration

Before performing the measurements, the heater and thermometers of the devices were calibrated as a function of temperature. Since the PTE device was characterized at room temperature, i.e.300 K, calibration was carried out in a temperature range close to 300 K. In the limited T range analyzed here, the resistance of Pt changes linearly as a function of temperature, following equation:

$$R(T) = R_0 + \frac{dR}{dT}(T - T_0) \tag{4.2}$$

where R_0 is the resistance at T_0, $R(T)$ is the resistance at T and $\frac{dR}{dT}$ is the temperature coefficient of resistant (TCR). Thus, to calibrate the resistance of the Pt strips and to obtain the $\frac{dR}{dT}$, the device is placed in a cryostat system with a fix temperature, then the Pt strips' resistances are measured in 4-wire configuration using a sourcemeter Keithley 2400. To avoid the influence of self-heating, the R_0 value is obtained extrapolating the experimental data of the I*x*R curves to zero current. The R_0 is measured at several temperatures close to 300 K and by the slope of the R_0xT the $\frac{dR}{dT}$ is attained. The I*x*R measurement of the heater at 300 K and the R_0 of the heater and thermometers as a function of the temperature are shown in Figure 4.11.

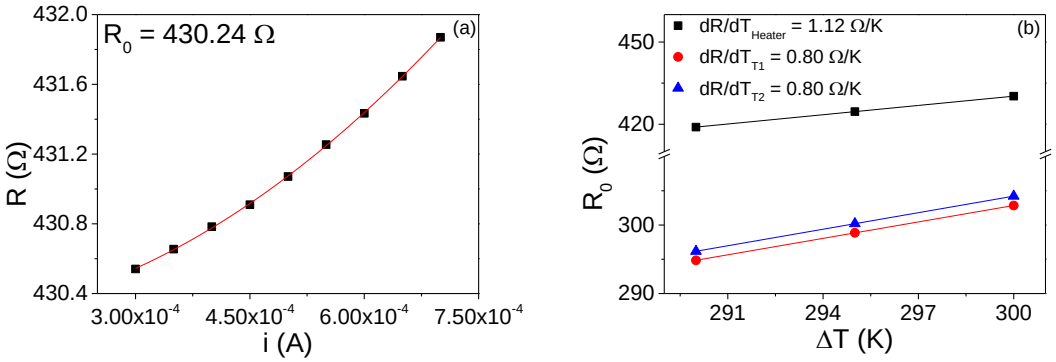

Figure 4.11 (a) I*x*R measurement of the heater at 300 K and **(b)** R_0 of the heater and thermometers as a function of the temperature.

4.2.4 Measurement procedure

The new device was microfabricated with the aim to verify the influence of the photogenerated charge carriers in the output voltage of Si thin films in response to a simultaneous temperature difference. To achieve high photoinjection an objective lens was used to collimate the Ar^+ laser beam with an excitation wavelength of 514 nm operating from 2mW to 7.9 mW into a spot of roughly 100 μm^2. The incident power per unit area was as high as $8x10^7$ W/m^2.

The protocol used was the following: since the heater and voltage probes are mm in length and the laser beam is focused onto a small spot we need to infer the average temperature of the Pt lines (hot and cold sides) and the local temperature at the laser beam

location. The central line (heater) is heated by Joule effect that produces a temperature difference in dark conditions between the center (hot) and Si frame (cold parts). During illumination the temperature changes locally at the laser spot but the metallic voltage and temperature probes measure the average Seebeck coefficient of the n,p materials. Due to the limited amount of feedthroughs in the cryostat that we have used for this experiment the temperatures were measured in 2-wire configuration. This measurement was carried out in collaboration with Alejandro Goñi from the Institut de Materials de Barcelona ICMAB-CSIC.

4.2.5 Photothermoelectric measurements

Measurements were carried out under dark and illumination conditions at different incident laser powers (2 mW, 3.8 mW and 7.9 mW). The device studied in this section has 300 nm of thickness and the distance between the electrical contacts is 250 µm. The incident light has 10 µm of diameter and was focused at the center of the TE leg, halfway the two metallic probes (heater-sensors) (See schematics in Figure 4.14a). Figure 4.12 shows the Seebeck voltage at open circuit as a function of the temperature difference of the p-type leg when the measurement is performed without illumination (dark) and illuminated with different powers.

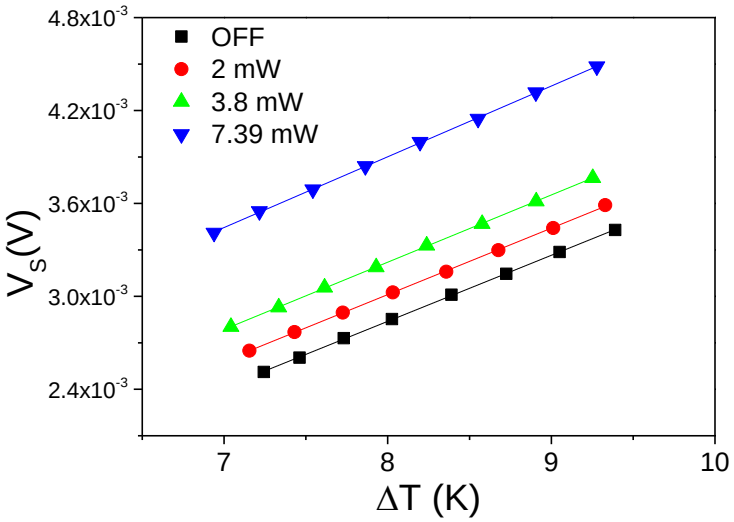

Figure 4.12 Seebeck voltage at open circuit as a function of the temperature difference when the *p*-type Si leg is in dark conditions and illuminated by laser light.

We obtain the Seebeck coefficient through the slope of $V_S \times \Delta T$ curves at the different conditions. Interestingly, we observe again an enhancement of S when the TE

leg is illuminated, as indicated in Table 4.2. The increase, compared to S_{dark}, amounts to *0,5%*, *1,8%* and *7%* at power levels of 2, 3,8 and 7,4 mW, respectively. The same type of measurements were carried out for the *n*-type Si leg.

Table 4.2 Seebeck coefficient of the *p*- and *n*-type Si legs in dark conditions and illuminated by laser operating at 2 mW, 3.8 mW and 7.39 mW.

	Off	**2 mW**	**3.8 mW**	**7.39 mW**
$S_p(\mu V/K)$	427 ± 2	429 ± 2	434 ± 2	456 ± 2
$S_n(\mu V/K)$	-272 ± 2	-282 ± 3	-277 ± 2	-274 ± 2

Figure 4.13 shows the variation of the slope of the $V_S \times \Delta T$ as the laser power increases for the n-type material. The maximum enhancement of the Seebeck coefficient is ~3.5 % when the device is illuminated at 3.8 mW. The value of the Seebeck coefficient in dark conditions for both, n and p-type materials, can be used to infer the amount of activated dopants in them. For this comparison we assume that the Seebeck coefficient does not depend on the thickness of the Si layer in the thickness range of our experiments, as already demonstrated by Salleh et al. [82]. For the *p*-type *S*=426 µV/K that corresponds to ~5x10^{17} cm^{-3} positive charge carriers and for the *n*-type *S*=-272 µV/K that corresponds to around ~8x10^{18} cm^{-3} electrons.

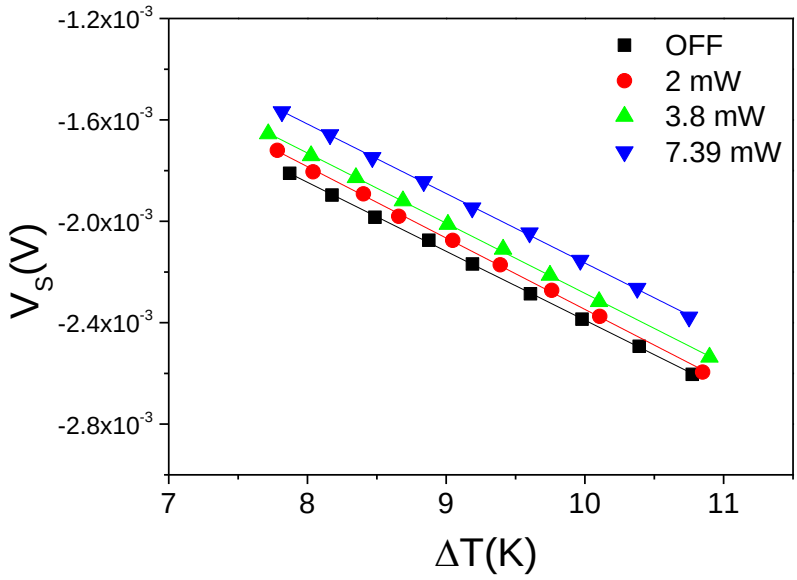

Figure 4.13 Seebeck voltage at open circuit as a function of the temperature difference when the *n*-type Si leg is in dark conditions and illuminated by laser light.

To investigate further the observed enhancement of the Seebeck coefficient the laser beam was focused at different positions between the central heater and the sensor located at the edge of the membrane (see schematics of Figure 4.14a).

These measurements may reveal the influence of the photoinjection location with respect to the diffusion length and nature of the carriers. Figure 4.14 presents the Seebeck voltage at open circuit as a function of the temperature difference at an average temperature close to RT when the incident light is positioned close to the heater (H), at the center (C) of the Si TE leg and close to the border (B) for *p*- (a) and *n*-type (b), (see schematics of Figure 4.14). These measurements are performed with the laser operating at 7.39 mW. The values obtained in these measurements are presented in Table 4.3. There are two main observations analyzing these data. First, the position of the laser beam does not affect the value of the Seebeck coefficient that for the p-type is still around 9% larger than under dark conditions for the three locations of the beam. Second, the voltage offset changes under illumination but its variation is affected by the position of the laser beam with respect to the metallic lines. In the *p*-type material, the offset value is higher when the light is close to the heater, while in the n-type leg, the offset value is higher when the laser beam is close to the border.

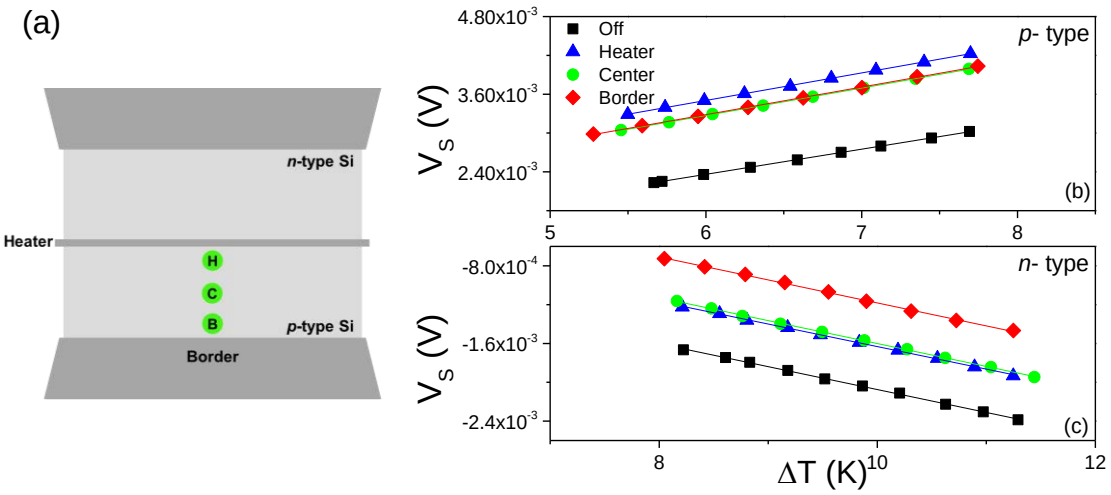

Figure 4.14 (a) Schematics of the incident light position. Seebeck voltage at open circuit as a function of the temperature difference for *p*- **(b)** and *n*-type **(c)** when the Si leg is in dark conditions and illuminated at different position from heater to border.

Table 4.3 Seebeck coefficient and offset voltage of the *p*- and *n*-type Si legs in dark conditions and illuminated by laser operating at 7.39 mW in different zones of the leg, close to the heater (H), at the center (C) and close to the border (B).

	7.39 mW (H)	**7.39 mW (C)**	**7.39 mW (B)**
$S_p(\%)$	9.2 ± 1.3	9.0 ± 1.1	9.5± 1.3
$\Delta V_p = V - V_{off}$	922 ± 20	699 ± 10	688 ± 20
$S_n(\%)$	-1.3 ± 0.8	0.9 ± 0.4	2.6 ± 1.2
$\Delta V_n = V - V_{off}$	406 ± 20	476 ± 20	906 ± 30

To verify if the increase of the Seebeck coefficient is caused by the photothermoelectric effect, or if it could be an effect related to the temperature distribution imposed by the local heating of the laser beam we conducted specific FEM simulations that only consider thermal effects. Before the simulations, the temperature rise caused by the local heating of the laser beam is experimentally obtained using Raman thermometry [47]. Using the same optical setup, the Raman spectra of the *p*- and *n*-type Si legs were measured at the laser beam location and by the spectral shift of the Si Raman mode, we can obtain the temperature rise [47]. Figure 4.15 shows the Raman spectra of *p*- and *n*-type Si legs for different incident laser powers.

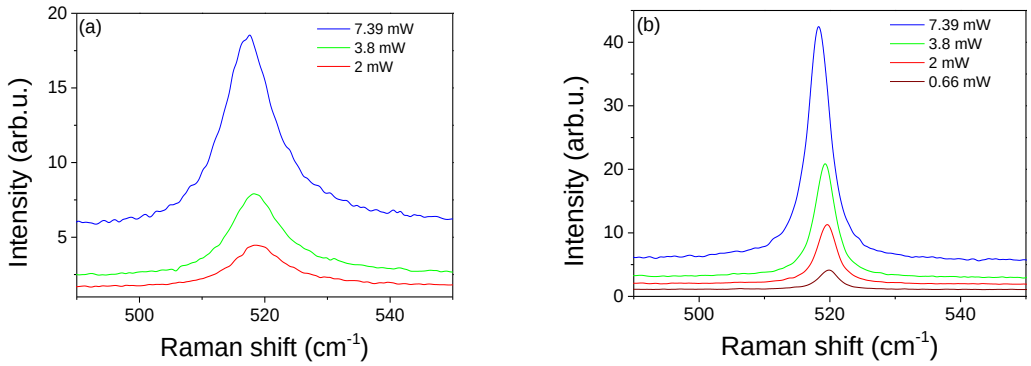

Figure 4.15 Raman spectra of *p*- **(a)** and *n*-type **(b)** Si legs for different incident laser power.

Because the TE legs are heavily doped the fit of the spectra is obtained pondering the Fano contribution [83–85]. Considering that the low laser power does not increase the temperature of the TE leg and by fitting the spectra, the temperature rise caused by the laser can be determined. Figure 4.16 shows the temperature rise as a function of the

incident laser power. Due to the difference between the Raman spectra intensity of the *p*- and *n*-type Si, it was not possible to measure the Raman spectrum of the *p*-type Si with the laser operating at 0.66 mW. Therefore, for the p-type we use the spectra acquired at 2 mW as the reference one. This is why the temperature values for the p-type material have a larger uncertainty.

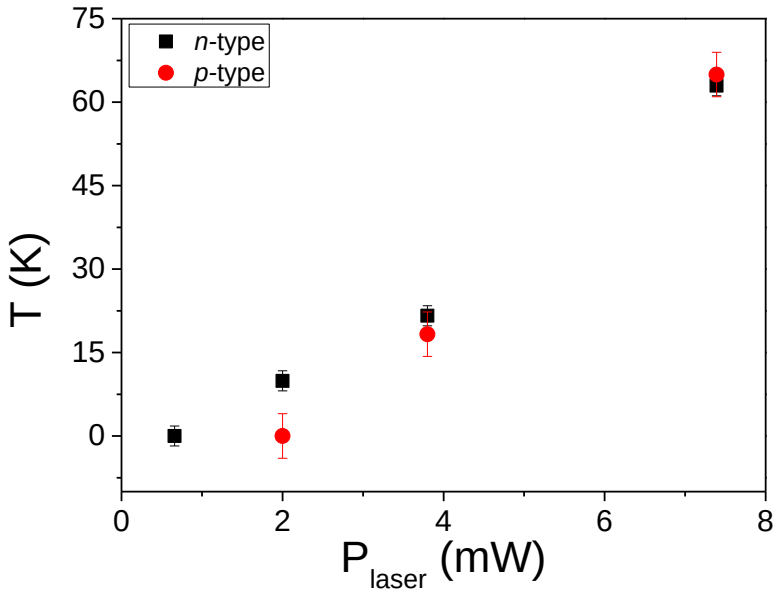

Figure 4.17 Temperature rise locally produced by the focused laser beam in *p*- and *n*-type Si legs for the different incident laser powers.

The laser operating at 7.39 mW increases the temperature of both TE legs around 65±5 K. This value of the temperature rise caused by the laser beam is used in the FEM simulations of the *p*-type legs. FEM simulations do not include the photoinjected carriers, that is, the simulations provide an analysis of the temperature profile and how it influences the values of the output voltage with respect to the temperature differences.

4.2.6 Finite Element Modeling

The experiment has been modeled using the Finite Element Method in a two-dimensional approximation to shed light about the observed phenomenology. In the 2D modeling approximation, when considering the compact geometry equivalent to the real system the magnitudes should be lumped and vertical dimension of the structure should be considered. In the present problem, the geometry corresponds to a membrane with a multiple stack of films (see microfabrication for details). In Figure 4.18, the seven different areas with the detail of the different contribution of films to the global stack is

reviewed. In our case, as d_z we will choose the thickness of the thermoelectric active layer, the monocrystalline silicon one, that measures 300nm. The rest of the magnitudes should be reevaluated considering the physical contribution of all the layers, to provide the effective value into the surface element.

To evaluate the thermal and the electrical conductance, the contribution of the different layers has been added weighted by the real thickness of each layer:

$$K_{lumped} = \sum_{i=1}^{N\ layers} K_i \frac{d_i}{d_z}$$

$$\sigma_{lumped} = \sum_{i=1}^{N\ layers} \sigma_i \frac{d_i}{d_z}$$

The term considering the heat capacity also includes the density, therefore following the same strategy, we have considered a common density for all the elements (the one of the Si) and the effective heat capacity magnitudes have been weighted before their addition for each elements of the surface.

$$Cp_{lumped} = \sum_{i=1}^{N\ layers} \frac{\rho_i}{\rho_{Si}} Cp_i \frac{d_i}{d_z}$$

To consider the Seebeck for each section, we have considered the dominant as the one of the most conductive layers in electrical contact. Therefore, for sections 1-2 and 4-5 the Seebeck considered is the one of the platinum, while in sections 6 and 7 dominates the Seebeck of the silicon doped membrane.

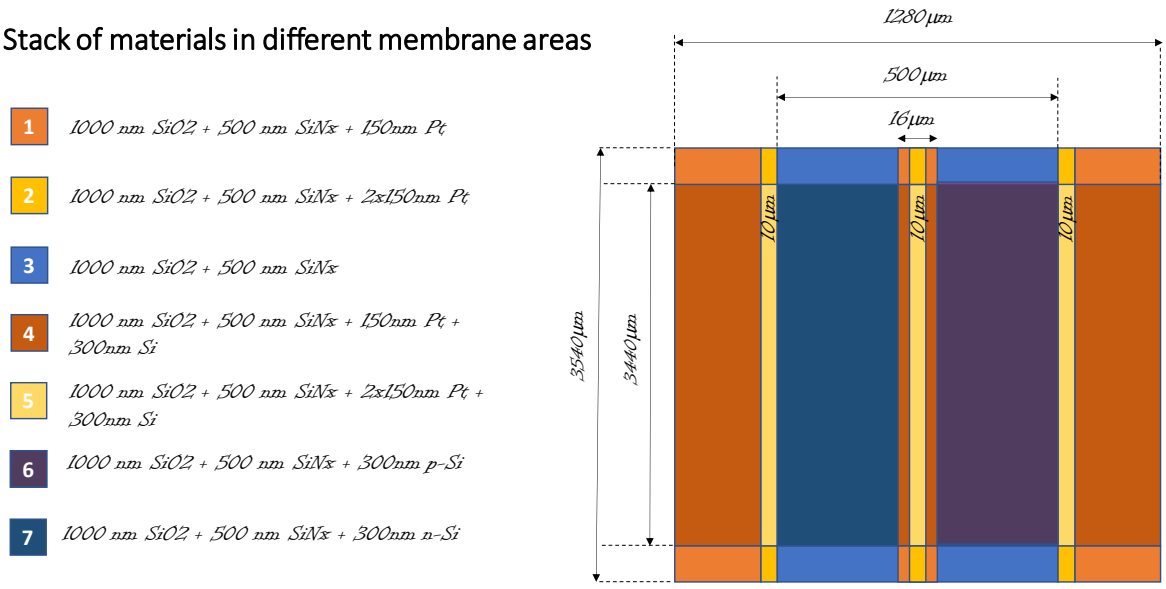

Figure 4.18 Schematics in planar view of the different sections of the membrane.

Table 4.4 Physical magnitudes used for the simulation.

Material	Thermal conductivity (W/mK)	Electrical conductivity (S/m)	Density (Kg/m^3)	Heat capacity (J/K)	Seebeck (µv/k)
Pt	70	$8.7x10^6$	21300	135	-5
Si *p*-doped	150	$1.1x10^4$	2300	700	340
Si *n*-doped	150	$1.1x10^4$	2300	700	230
SiO_2	1.7	0	2400	720	-
SiN_x	2.5	0	2400	710	-

To model the behavior of the devices, mimicking the real experiment a variable power (0 to 10mW) has been released into the central heater section. Parallelly, a spot of 10 µm diameter has been defined in different sections of the membrane to simulate the power released by the absorption of the laser beam. The amount of power released in the spot of the laser has been adjusted to promote similar heating than those observed by local Raman.

Figure 4.19 shows the simulated temperature profiles of the PTE device in the case of 10 mW dissipated in the heater with the additional heat source produced by the laser beam at different locations. The laser heating produces an increase of the temperature of 70 K at the laser spot.

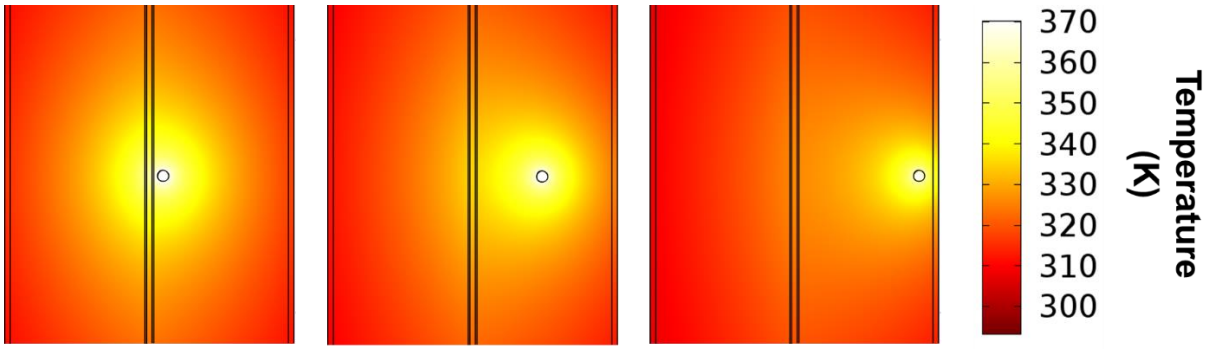

Figure 4.19 Temperature profile of the PTE device with the additional heat source produced by the laser beam at different locations, (left) close to the heater, (center) at the center and (right) close to the border.

Figure 4.20 shows the FEM simulations results for the open circuit voltage measured as a function of the temperature difference (Figure a) and the voltage offset variation as a function of the position of the laser beam (Figure b), being 0 the position of the central heater and 250 µm the distance between the central heater and the outer sensor.

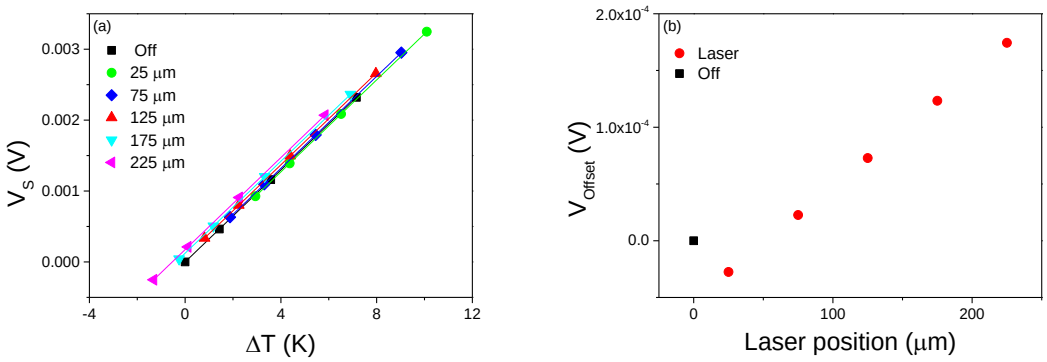

Figure 4.20 Seebeck voltage at open circuit as a function of the temperature difference obtained by FEM simulations **(a)** and the voltage offset of each curve **(b)**.

FEM simulations show that the Seebeck coefficient derived as the ratio between the output voltage and the temperature difference (the slope of the curves of Figure 4.20a) remains constant when the laser-induced heating is considered. That is, in the absence of photoinduced carriers there is no variation of the Seebeck coefficient even if the thermal profile of the device changes locally due to the laser heating. It is important to note that in the simulations the Seebeck coefficient of Silicon was a constant parameter. In reality

it is known [33] that the Seebeck coefficient of bulk Si (intrinsic or highly-doped) decreases with temperature in the temperature range of our measurements (around 300 K). In contrast, the values of the offset voltage change as a function of the laser position due to the temperature difference achieved in each case. As shown in Figure 4.20a,b the displacement of the light heat source from the heater to the border produces a vertical shift on the simulated $V_S \times \Delta T$ curves. Figure 4.20b shows the offset increases up to 200 μV when the laser beam is located close to the outer metallic line.

The potential and the charge density of the PTE device are also analyzed. Figure 4.21 shows the FEM results for the potential and charge density of PTE device with the additional heat produced by the laser beam at the different locations (H, C, B).

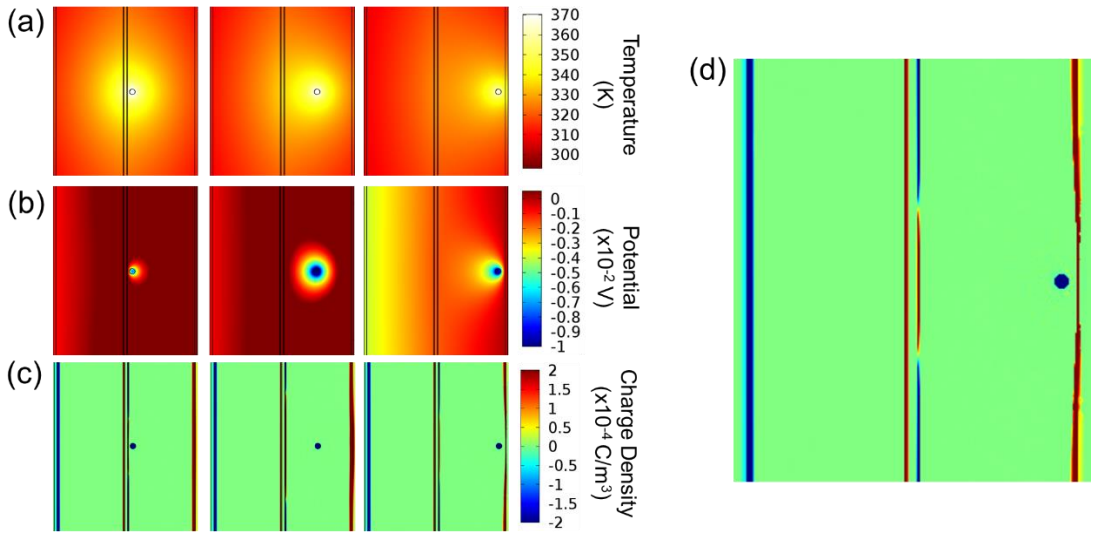

Figure 4.21 Temperature profile **(a)**, the potential **(b)**, and the charge density **(c)** of the PTE device with the additional heat source produced by the laser beam at different locations: H, C, B. **(d)** Close up of the charge density for the case in which laser heating is positioned close to the border, (B).

Observing Figure 4.21b it is possible to verify that the potential at the location of the laser heating is deeply modified. It is notorious that the high temperature of the laser beam distorts the local heat flux inducing the charges carriers to move away from the laser region. That is, as the material is *p*-type local heating forces the positive charges to diffuse away from the hot region to regions of lower temperature. The laser area is therefore depopulated from positive charges and its potential becomes much lower (blue color in Figure 4.21b) than the surrounding regions. In terms of charge density (Figure 4.21d) when the laser is at location B close to the sensor positive charges accumulate in

it with a lesser amount being diffused to the central section of the heater. In this case, the offset voltage (measured as V_{sensor}-V_{heater}) is maximum compared to the dark condition, as shown in Figure 4.20b. If the laser beam is located at position H (close to the heater) positive charge injection into the heater line is very effective and (V_{sensor}-V_{heater}) may become even slightly negative, as observed in Figure 4.20b. At some point at around 75 µm away from the heater the temperature distribution is such that the offset is similar to the one measured in dark conditions without biasing the structure.

Summarizing, thermal-based FEM without considering photoinjection indicate that the offset voltage is produced by charge accumulation at the contacts and changes with the position of the laser beam, but this effect does not modify the ratio between the output voltage and the ΔT, the Seebeck coefficient.

4.2.7 Discussion

The experimental results as well as the finite element modelling support the idea that the observed enhancement of the Seebeck coefficient is related somehow to the photogenerated carriers, since apparently standard thermal effects in the linear regime can not explain it. In order to be more quantitative in the discussion of the photothermoelectric effect we estimate the number of photoinjected carriers per unit volume generated by light. In this way, equation 4.3 is used:

$$\Delta n = \tau \alpha \phi (1-R)^2 (1-e^{-\alpha l}) QE \tag{4.3}$$

where τ is the lifetime of the charge carriers, α is the absorption coefficient, l is the thickness of the absorbing medium, R is the percentage of light reflected by the film, and $\phi = P\lambda_{exc}/Ahc$ is the intensity of light divided by the photon energy (in other words, the amount of arriving photons per unit area), P is the power light, λ_{exc} the wavelength of the excitation light, A is the area, h is the Planck's constant, c is the speed of light and QE is ratio of photon converted to electrons, which is 97% for Si at 514 nm [86]. Using the values of Si and considering that the lifetime is 0.9 µs [87,88], the number of photocarriers generated by laser light is around of 2×10^{19} cm^{-3}. This huge amount of photoinjected carriers, larger than the doping level of both p and n-type materials, is generated in a small zone of the TE leg of area about 100 µm^2. In terms of carrier population the photoinjection modifies by an order of magnitude the population of majority carriers but dramatically

increase the population of minority carriers. In the case of the p-type material the recombination lifetime of the minority carriers is reduced.

The laser produces a large quantity of photoexcited states (excitons) that dissociate into the same density of positive and negative carriers and therefore should not contribute to the Seebeck effect. Only in the case that electrons and holes show different mobilities or lifetimes photoinjection may play a role.

The thermoelectric power has two main components: the diffusive part due to the diffusion of charge carriers, S_d, and the phonon-drag thermopower, produced by the momentum transfer between phonons and charge carriers, S_{ph}. S_d is typically expressed though the Mott equation and thermopower can be maximized by enhancing the variation of σ near the Fermi level. It is possible that injection by a laser of energy 2 eV leads to hot carriers with an excess energy per carrier. If the population of carriers is not balanced because of their different lifetimes and more holes arrive to the contact cold side the Seebeck coefficient will increase because the carriers carry more energy per charge (See Figure 4.22).

On the other hand, phonons also carry thermal energy and migrate from hot to cold. If the interaction phonon-charge carrier is sufficiently large the charge carriers can be swept along with the phonons. Since the hole mass in Si is around $0.36m_0$ for conductivity considerations and the electron mass is $0.26m_0$ for electrons we may expect a stronger interactions of the phonon bath with the positive carriers. That means small imbalances of the phonon drag between the positive and negative photoinjected carriers. This would be comparable to saying that the lifetime for recombination of holes (majority carriers) is slightly larger than the one for electrons (minority carriers) in the *p*-type material (see the schematic representation of figure 4.22), And therefore, there might be an enhancement of the open circuit voltage for a given ΔT, producing a rise in the Seebeck coefficient. We suspect this behavior is also related to the large temperature gradients imposed by the laser beam that locally heat the laser spot 65 K above the surroundings. The smaller increase in the *n*-type material may be related to the higher doping level that leads to a lesser influence of photoinjection [36,37].

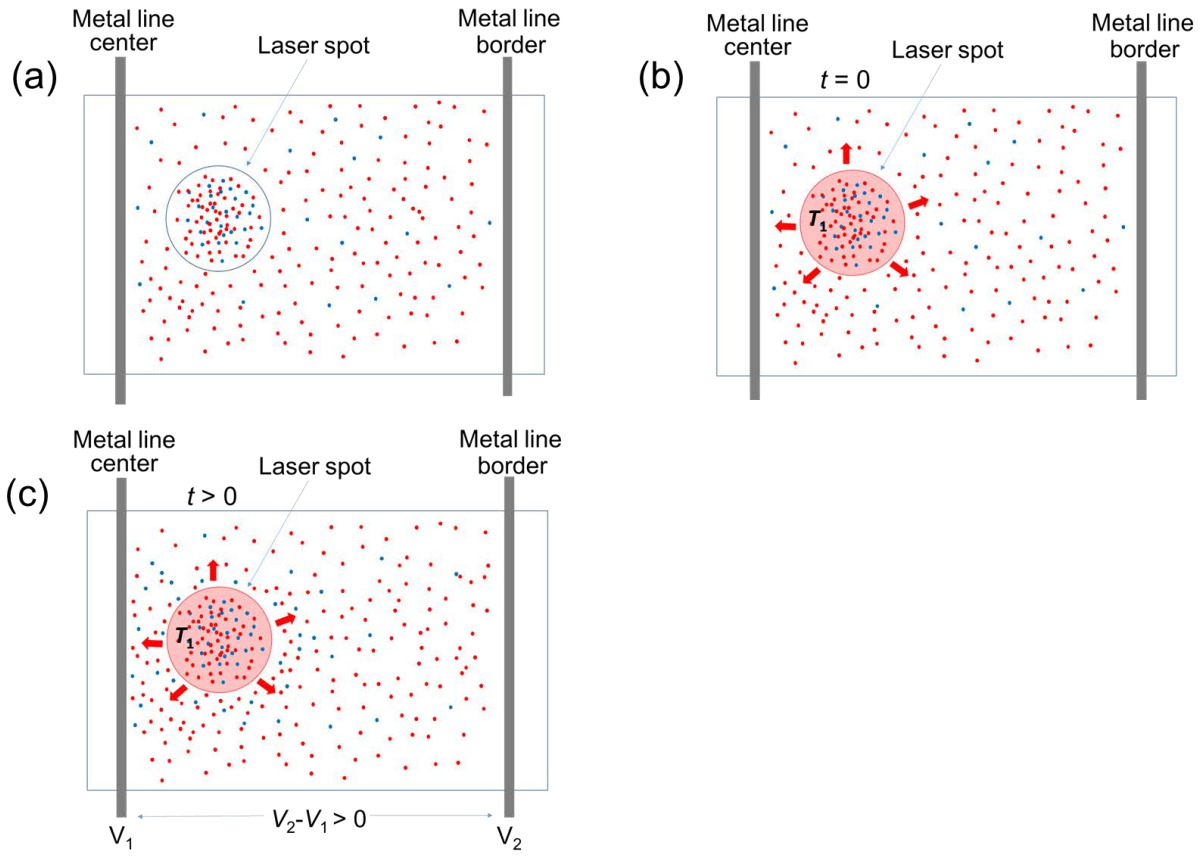

Figure 4.22 (a) Schematic representation of the generation of electron-hole pairs inside the laser spot region without a temperature increase with respect to the surroundings; **(b)** idem with T increase but shown at $t = 0$ before the carriers have time to diffuse; **(c)** idem at $t > 0$ showing the unbalanced flux of holes due to shorter recombination time of the minority carriers leading to an increase of the V_2-V_1 voltage difference.

4. 3 Conclusions

The photothermoelectric effect in highly-doped Si thin films was explored. We described the use as photosensor of a thermoelectric microdevice based on single-crystalline Si thin films. By decreasing the thickness, the thermal conductance and heat capacity of the Si thermopiles were significantly reduced, therefore substantially improving the thermal insulation of the membrane. The result was an enhancement of the detectivity of the TE device to very small temperature differences. Furthermore, a small thermal time constant was obtained. FEM simulations were used to obtain the real temperature gradients applied to the thermoelectric legs, correcting the non-flat temperature profile generated during the experiments. The linear dependence of the

output voltage with the input power facilitates the use of the microsensor as a photosensor. The R_S was determined being 13 V/W in air at atmospheric pressure. The measurements carried out with a chopped light beam evidenced the quick response time of the device due to its very small thermal mass, ~4.3 ms. Finally, the D^* of the device was 2.86×10^7 $cmHz^{(1/2)}W^{-1}$. During the photoresponse measurements, an unexpected enhancement of the Seebeck coefficient was observed as a result of the photogeneration of charge carriers.

To understand this unexpected effect, a new device was developed, which allows to measure the Seebeck coefficient of each thermoelectric leg (n and p-type) separately. The Seebeck coefficient of the *p*- and *n*-type legs were measured in dark conditions and under illumination. An increase of 7% and 3.5% of the Seebeck coefficient was observed in the *p*- and *n*-type Si leg, respectively. This is an outstanding result since the strong photoinjection was limited to a very small area (100 μm^2) compared to the area of the device ($5x10^5$ μm^2). Using the principles of the Raman thermometry, the heating caused by laser was determined to be around 65 K. Thus, simulations were performed considering the heating contribution of the laser, which shows that the improvement of the Seebeck coefficient is an effect of the photocarriers generated by light. Although we still do not have a complete understanding of the observed variation of the Seebeck coefficient, this effect could be extremely relevant to boost the figure of merit of Si devices using local photoexcitation. The offset voltage values obtained during the experiments show that the photovoltaic effect contributes to it increasing the initial voltage values of the *p*-type Si leg.

5. Microgenerator based on MgAgSb thin film

MgAgSb-based materials have shown a great potential as p-type thermoelectric materials due to their high Figure of Merit (*ZT*) close to room temperature. In this chapter the growth of MgAgSb thin films with a small amount of Ni using the sputtering method will be described. The thermoelectric properties of the thin films are measured and a full microthermoelectric device based on MgAgSb thin film is microfabricated and characterized.

5.1 MgAgSb-based material

One of the main aims of the thermoelectric community is to find electrical conductors with a very low thermal conductivity. A possible strategy is to employ materials with complex crystal structures, large unit cells and a large number of atoms in it. Half-Heusler materials with chemical formulas X_2YZ and XYZ and crystal structures related to fluorite satisfy this criterion. However, despite the half-Heusler structure of the MgAgSb alloys that is known to possess interesting electrical and magnetic properties, the thermoelectric properties of these materials were not studied until 2012. M. Kirkham et al. measured a *ZT* of ~ 0.35 at room temperature [89] with values of *k* from 1.1-1.5 W/mK in the *T* range spanning from room *T* up to 200C. They identified three possible polymorphs depending on the preparation temperature. At low *T* the alpha phase, stable up to XC, the beta phase stable in the mid *T* range, and the high-temperature gamma phase. The α and β have a tetragonal disordered structure, while the γ-phase has a cubic half-Heusler structure (See Figure 5.1).

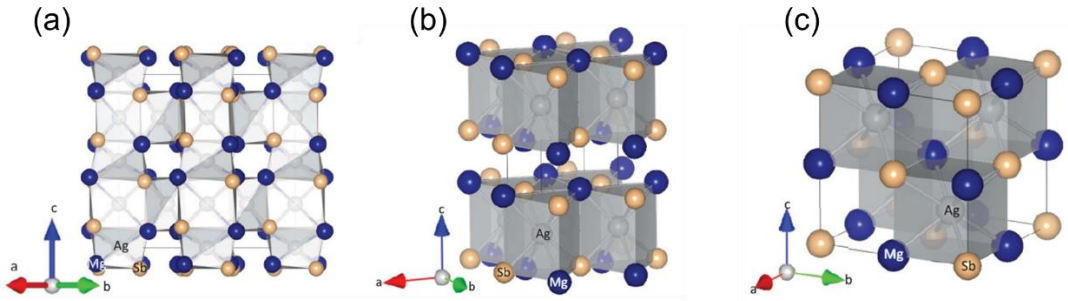

Figure 5.1 Crystal structure of the α **(a)** and β **(b)** γ **(c)** MgAgSb phase. Extracted from Kirkham et al. [89].

The powder diffraction files of the three structures as well as the experimental X-ray patterns obtained by Kirkham et al. are shown in Figure 5.2.

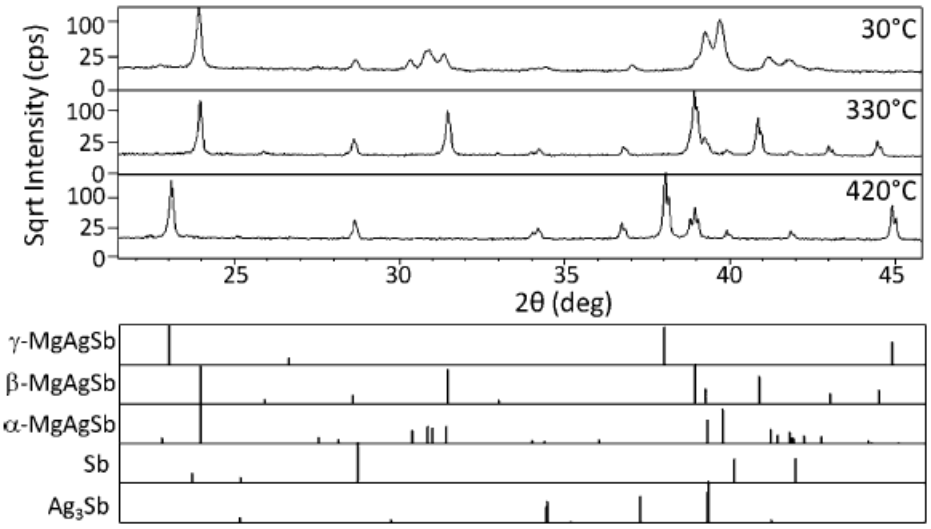

Figure 5.2 (top panel) X-ray diffraction profiles measured at 30ºC (top), 330ºC (middle) and 420ºC (bottom). **(bottom panel)** Powder diffraction profiles for the three MgAgSb phases plus typical impurity phases of Sb and Ag_3Sb. Extracted from Kirkham et al. [89].

The low thermal conductivity of the α-phase is related to the 24 atoms in the unit cell that implies 3 acoustic and 69 optical branches in the crystal. Since in general optical branches have small contributions to the lattice thermal conductivity due to their low phonon velocities, it is expected that α-MgAgSb will exhibit low $k_{lattice}$. In relation to this, previous nanoindentation measurements in α-MgAgSb have revealed a low elastic modulus of 55 GPa, consistent with the weak chemical bonding and low thermal conductivity in this material [90].

First studies [89] of the three phases already identified that the power factor ($S^2\sigma$) is highest in the low temperature phase with values attaining 18 $\mu Wcm^{-1}K^{-2}$ at 290ºC, while the β and γ phases reach 2 and 4 $\mu Wcm^{-1}K^{-2}$, respectively. So, the α-phase combines a high Seebeck coefficient with a high electrical conductivity. Further work in very recent years, have demonstrated the potential of MgAgSb-based compounds as thermoelectric material for applications in the low temperature range (from 300 K to 550 K). The high *ZT* value achieved so far combined with its good mechanical properties and the abundancy of the elements offers a promising future for thermoelectric applications [12].

α-MgAgSb presents the best thermoelectric performance and therefore the main efforts are devoted to its synthesis in pure form. In fact, Kirkham et al. already reported the strong difficulties to obtain the α-phase without impurities or other phases.

Typically, the samples synthesized by vacuum-melted and hot-pressing methods contain secondary phases of Ag and Ag_3Sb that lead to a reduced *ZT*. Yin et al. used long-time annealing protocols (1-2 weeks at 550 K) to get the room temperature phase reducing the concentration of impurity phases up to a mass fraction below 2% [90].

In real materials intrinsic point defects in crystals are deleterious to the phonon mean free path due to enhanced scattering of short-wavelength phonons. This strategy was applied to MgAgSb compounds by Zhao et al. [91] and further refined by Liu et al. [92]. Zhao et al. used a two-step ball milling method in combination to a quick hot-pressing process to finely tune the phases and stoichiometry of the MgAgSb alloy. They successfully synthesized both, MgAgSb and $MgAg_{0.97}Sb_{0.99}$, with grain sizes around 20 nm and free of impurities. The corresponding *ZT* was improved to around 0.7 at 300 K. In this same work, a *ZT* of ∼0.9 at room temperature was achieved by adding a small amount of Ni, yielding a MgAg0.965Ni0.005Sb0.99 alloy [91]. Liu et al. controlled the synthesis temperature to manipulate the Ag vacancy concentration and tailor carrier and phonon transport behavior. They reached a peak *ZT* of 1.3 and average *ZT* of 1.1 for samples hot pressed at 533 K. MgAgSb alloys prepared with small amount of In, Cu, Na, Li, Ca, Yb and Zn also attained *ZT's* higher than 1 between 300 K and 550 K [93]. In general, the required phase of the MgAgSb alloy is synthesized in bulk form at relatively high temperature [93].

In this chapter, we explore the feasibility to grow these materials as thin films by vapor deposition in order to fabricate a planar microthermoelectric generator. The MgAgSb(Ni) thin films are grown using the sputtering technique and the phase and stoichiometry are characterized by XRD and SEM-EDX measurements. The in-plane thermal conductivity of the samples is determined via 3ω-Völklein method while the electrical conductivity and Seebeck coefficient are measured using a homemade test system. Finally, a microthermoelectric generator based on a sputtered MgAgSb thin film is designed, fabricated and characterized.

5.1.1 $MgAg_{0.95}Ni_{0.005}Sb_{0.99}$ thin film

MgAgSb thin films with a small addition of Ni (<0.5%) were deposited using the sputtering system model A3000-0014-M from AJA International. A target with the

required composition was purchased from Testbourne Ltd to ensure the same composition in the sample with respect to the target material. Initially, the samples are deposited on (100)-single crystalline Si substrates capped by a 450 nm thick SiN_X film. After growth the samples are characterized by X-ray diffraction (XRD) in order to verify the degree of crystallinity, structure of the crystalline phases and purity of the sample. The growth of the films via sputtering is highly dependent on several parameters such as the power applied to the target, deposition pressure and temperature, distance between source and substrate and inclination of the source. The inclination of the source and the distance between the target and substrate were fixed for all experiments at 7º and 15 cm, respectively. The first sample was deposited at a substrate temperature of 650 K using a DC power of 100 W and a deposition pressure of 10 mTorr. The sample was grown for 90 min with a growth rate of 10 nm/min. Figure 5.3 shows the XRD patterns of the sample deposited at 650 K (red line) and after annealing for 2h at 750K.

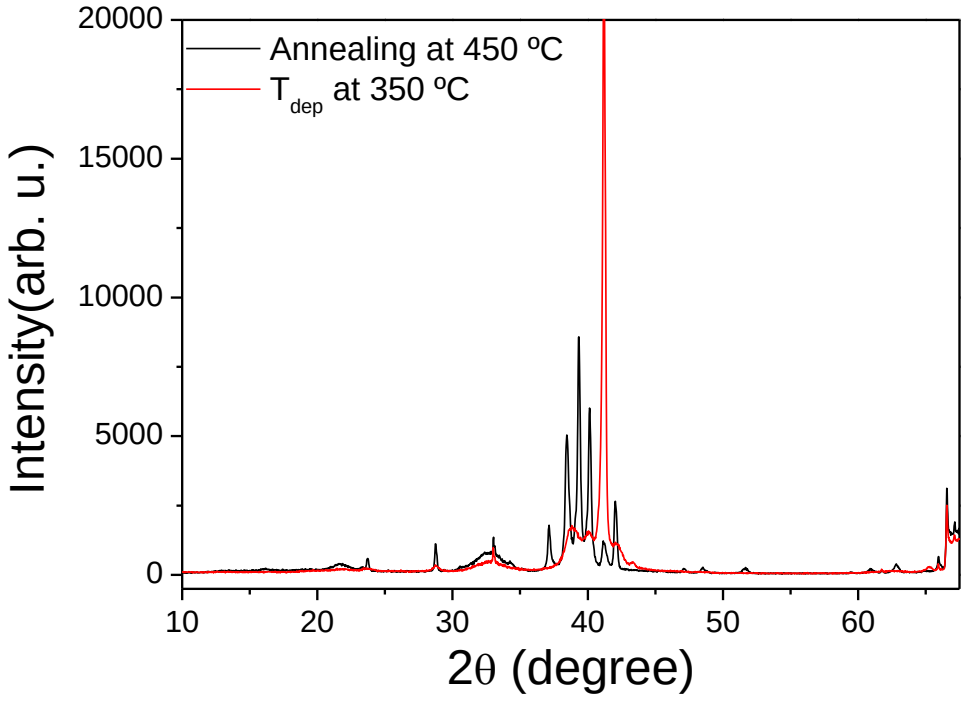

Figure 5.3 XRD patterns of the $MgAg_{0.95}Ni_{0.005}Sb_{0.99}$ sample deposited at 650 K (red curve) and the sample post annealed at 750 K for 2 h (black curve).

Comparing the sample's patterns shown in Figure 5.3 with the patterns of the sample synthetized by Kirkham (Figure 5.2) it is possible to observe that the sample deposited at 650 K did not obtain the same crystalline phase. In order to obtain a sample

more crystalline and purer phase, the sample was submitted to an annealing process at 750 K during 2 hours. The X-ray diffraction measurement was carried out post annealing process and is shown in Figure 5.3 (black curve). It is possible to observe that after the post annealing process the sample became more crystalline. Despite this, the peaks between 35º and 39º are related to the Ag_3Sb secondary phase [91,94] and the peak at around 28º is due to Sb. The next step would be to measure the thermoelectric properties of the samples deposited using these parameters, but unfortunately the target used in this deposition melted because of the high temperature reached at the target. This occurs when a high power is applied and the cooling system is not able to efficiently cool the target.

Therefore, a new target with the same stoichiometry was acquired at the same vendor. In the first tests with the new target, we verified that the deposited samples were not electrical conductors probably because the surface of the target was slightly oxidized. After some depositions, the oxide on the surface of the target is completely sputtered and the samples deposited at room temperature were conductors. After this, three different samples were deposited. The deposition was performed with a deposition pressure at 15 mTorr and to avoid that the target overheats the power applied to it was limited to 59 W, resulting in a low growth rate $\sim 6\,\text{Å}/min$. Several samples were deposited at room temperature, 450 K and 600 K. The deposition temperature was controlled to verify if the crystalline phase is achieved even at low deposition temperatures. The crystalline structures of the samples were characterized by grazing incidence X-ray diffraction (GIXD). This technique was preferred in relation to the XDR because the samples are very thin. The GIXD patterns of the samples deposited at room temperature, 450 K and 600 K are shown in Figure 5.4.

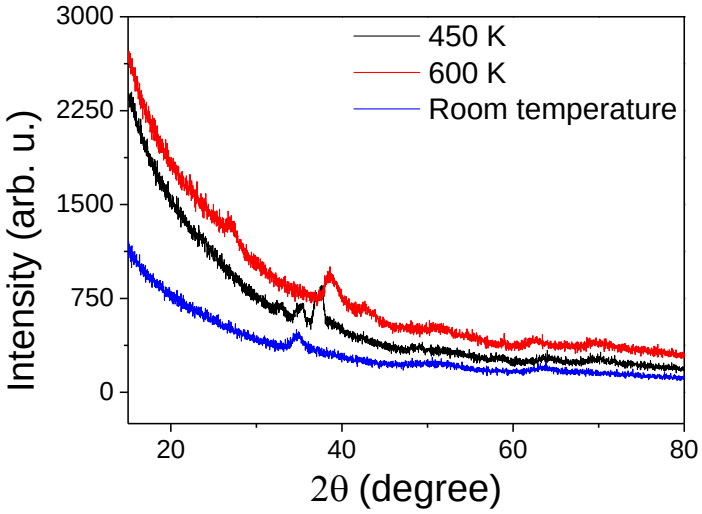

Figure 5.4 GIXD patterns of the $MgAg_{0.95}Ni_{0.005}Sb_{0.99}$ sample deposited at room temperature (blue curve), 450 K (black curve) and 600 K (rede curve).

Figure 5.4 shows that the deposited samples are highly disordered with small crystalline peaks of low intensity and some amorphous background. As the samples deposited below 450 K were conductors, the thermoelectric properties of the sample deposited at room temperature were measured. For this purpose, a sample was deposited on the device to measure the Seebeck coefficient (Section 3.2) and on a 3ω-Völklein sensor to measure the in-plane thermal conductivity. Figure 5.5 shows the Seebeck voltage at open-circuit as a function of the temperature difference and the $\Delta T_{2\omega} \times P$ curve used to calculate the Seebeck coefficient and the in-plane thermal conductivity of the sample, respectively.

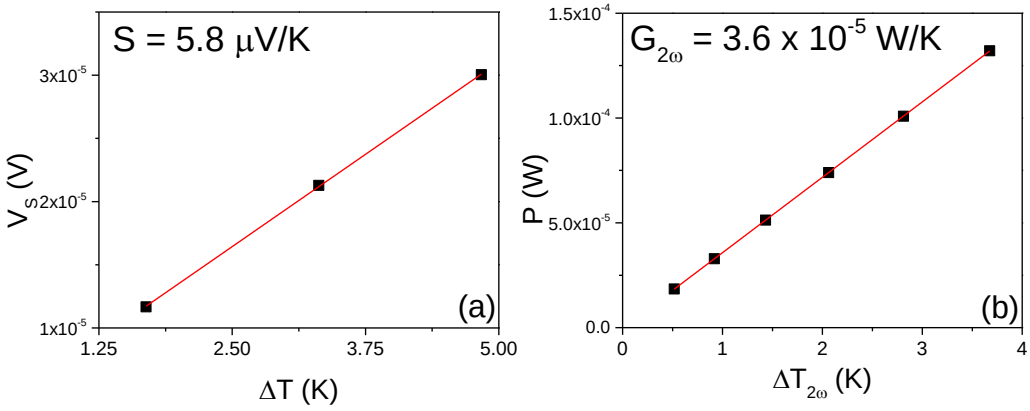

Figure 5.5 Plot of the Seebeck voltage at open circuit **(a)** and $\Delta T_{2\omega} \times P$ curve **(b)** of the $MgAg_{0.95}Ni_{0.005}Sb_{0.99}$ sample. The error bars are smaller than the symbols.

By the slope of the Seebeck voltage at open-circuit the Seebeck coefficient can be obtained, being $\sim 6\,\mu V/K$. The slope of the $\Delta T_{2\omega} \times P$ curve gives the thermal conductance of the sample plus membrane $(3.59 \times 10^{-5}\,W/K)$. Subtracting the contribution of the thermal conductance of the membrane, that was measured beforehand, the thermal conductance of the sample can be calculated. The in-plane thermal conductivity is determined considering the sample dimensions. The measured value is $\sim 4{,}0 \pm 0.2\,W/mK$. This value is much higher than the one typically measured in MgAgSb alloys. The uncertainty in the in-plane thermal conductivity is mainly attributed to the sample thickness. The values of the thermoelectric properties show that a more crystalline phase is required to obtain samples with high *ZT* value. The deposition temperature used is lower than the one required to obtaining highly crystalline films and the deposition carried out at 600 K produces oxidized samples. Even though the base pressure of the vacuum chamber is very low, around $5x10^{-8}$ mbar, the small deposition rate favors the oxidation of the sample during the flight of the atoms to the substrate or during the residence time before atoms are buried by new atoms. .

Next, in order to increase the growth rate, a codeposition strategy was adopted. The codeposition consists in using two or more targets to grow a sample with the desirable stoichiometry. Due to limitations of our sputtering setup concerning the number of guns that could be operated simultaneously we decided to use two targets: $MgAg_{0.95}$ and $Ni_{0.005}Sb_{0.995}$ to get a film of $MgAg_{0.95}Ni_{0.005}Sb_{0.99}$. To obtain the desirable stoichiometry the targets must deposit the same amount of material during the deposition. First, a deposition of $MgAg_{0.95}$ sample was achieved with the pressure deposition at 12.2 mtorr and at room temperature during 15 min. The power applied to target was 69 W obtaining a growth rate of 12 Å/min. Second, to deposit the $Ni_{0.005}Sb_{0.995}$ film, the RF mode at 13560 KHz was used. The growth rate was tuned to obtain the same deposition rate of the $MgAg_{0.95}$ sample, thus, the sample was deposited applying 30 W, at 15.2 mTorr and at room temperature. After this, the $MgAg_{0.95}Ni_{0.005}Sb_{0.99}$ film was deposited at room temperature using the powers described before and at 12.2 mTorr. In agreement with previous results, the sample codeposited at room temperature is highly disordered, as shown in Figure 5.6. Although a Rietveld refinement analysis does not yield accurate results for this 'amorphous' phase, the convergence is reasonable for a single α-MgAgSb phase. However, convergence with other phase mixtures may also be possible.

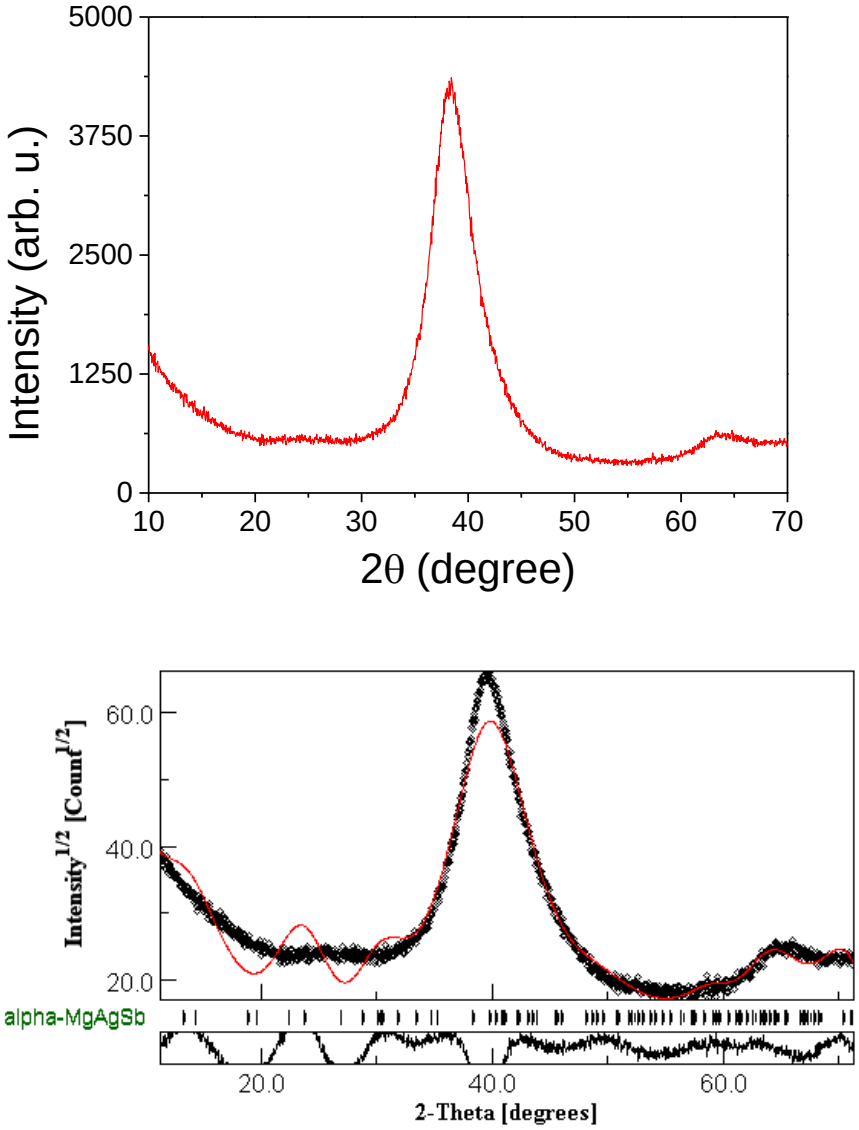

Figure 5.6 (top panel) GIXD patterns of the $MgAg_{0.95}Ni_{0.005}Sb_{0.99}$ sample deposited at room temperature. **(bottom)** Rietveld refinement of the disordered structure.

Afterwards, as the deposition pressure used during the deposition has to be the same for the two targets we slightly increased the power applied to the $Ni_{0.005}Sb_{0.995}$ target up to 38 W, since the growth rate of 12 Å/min was attained at 15.2 mTorr and the amount of material sputtered is related to the deposition pressure and power. To obtain a more crystalline phase the sample was deposited at 650 K and then the sample was characterized by GIXD. Figure 5.7 shows the GIXD patterns of the sample codeposited at 650 K (top panel) and the Rietveld refinement of the structure (bottom panel) that

identifies the crystalline phases as being Ag_3Sb (84%) and the high-temperature form of the MgAgSb-structure: γ-MgAgSb (16%).

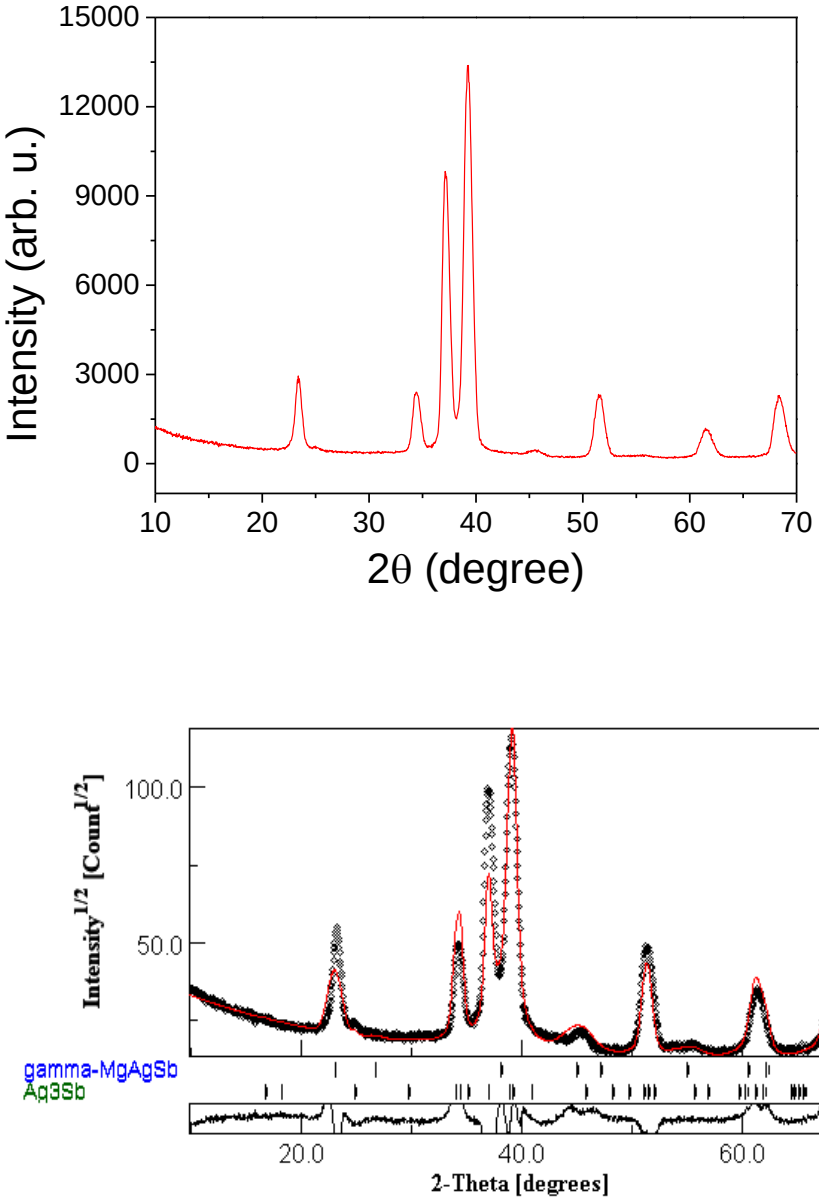

Figure 5.7 (top panel) GIXD patterns of the $MgAg_{0.95}Ni_{0.005}Sb_{0.99}$ sample deposited at 650 K. Rietveld-refinement of the GIXD pattern shown in **(bottom)**.

To verify the stoichiometry of the codeposited sample energy dispersive X-ray spectroscopy (EDX) measurements were done. This technique permits to analyze the composition of the sample and the proportions of each element. The measurements were performed using the scanning electron microscope (SEM) model MERLIN FE-SEM.

Table 5.1 shows the percentages of each element, Ag, Mg and Sb also O of the sample deposited using codeposition process.

Table 5.1 Percentages of each element of the MgAgNiSb film deposited using codeposition.

Element	Atomic%
O	17.57 (±0.59)
Mg	18.01333 (±0.39)
Ag	43.27667 (±0.35)
Sb	22.15 (±0.37)

Surprisingly the amount of Ag deposited is ~ 2.4 times higher than the amount of Mg. This stoichiometry explains in part the difficulties associated to the growth of a pure MgAgSb phase, since the proportion between the Mg and Ag cannot be easily changed. In contrast, the proportion between Sb and Ag is very closed to the required value. The presence of oxygen may be due to partial oxidation of the sample after the sample is removed from the sputtering chamber and exposed to ambient conditions. Because of the limited resolution of the EDX apparatus it was not possible to confirm the presence of Ni in the grown film.

Due to the difficulties obtaining suitable layers with the new target as well as the problems that appeared during codeposition, we decided to use the first target again. As discussed before, this target overheated during the first deposition, thus, the new deposition is performed using lower power levels. The power applied to the target was 29 W and during the deposition process the target temperature was checked through the value of the voltage applied to the gun to ensure no overheating. The pressure and deposition temperature were 10.5 mTorr and 650 K, respectively. The growth rate attained during this deposition is $\sim 6.6\,\text{Å}/min$, but the deposition was carried out with better base pressure and the walls of the chamber were cooler than in previous experiments, what minimizes degassing from the chamber walls. The sample deposited with these parameters was characterized by GIXD, as shown in the top panel of Figure 5.8. The Rietveld refinement of the structure (bottom panel) although quantitatively not satisfactory probably due to some preferential orientations yields information about the quantity of the phases: α-MgAgSb: 39 %, Ag_3Sb: 48 % and Sb: 12 %.

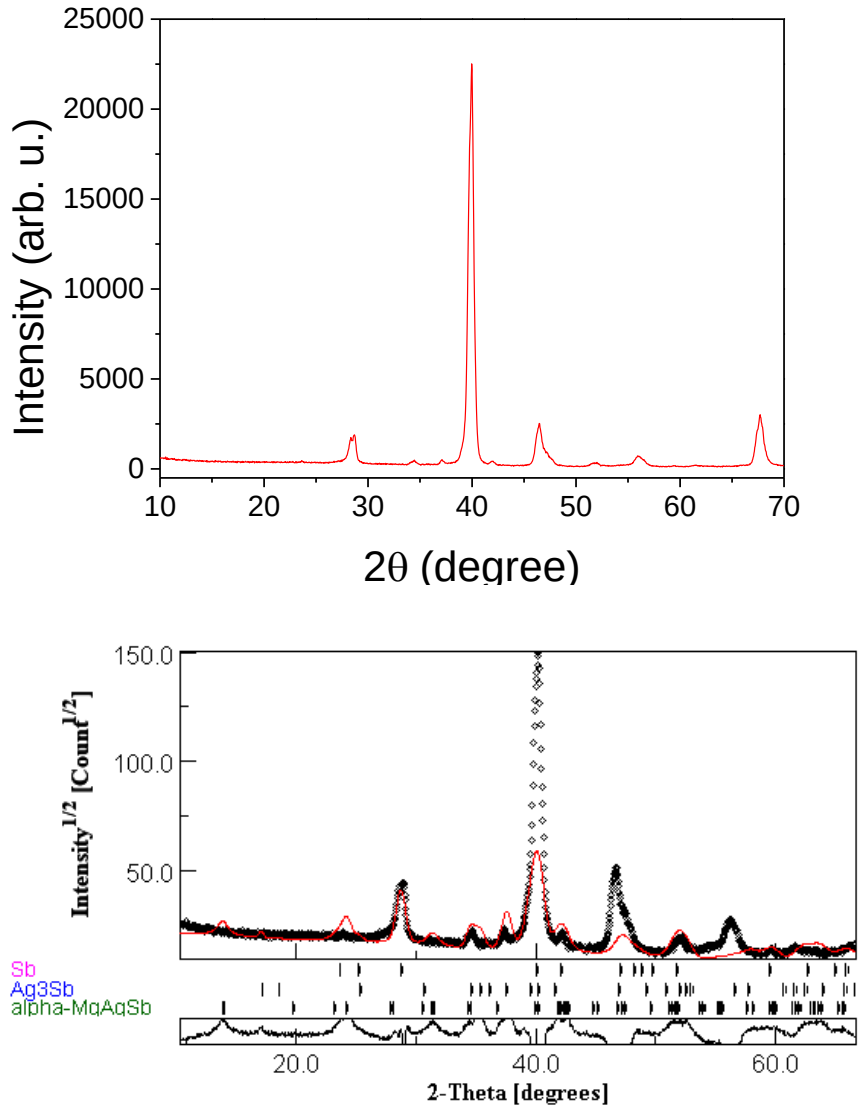

Figure 5.8 (top panel) GIXD patterns of the $MgAg_{0.95}Ni_{0.005}Sb_{0.99}$ sample deposited at 650 K. **(bottom panel)** Rietveld refinement of the structure using various phases.

During this deposition, the film was also deposited on a device to measure the Seebeck and electrical conductivities, as well as on a 3ω-Völklein sensor to determine the in-plane thermal conductivity. Figure 5.9 presents the *IV* curve, the Seebeck voltage at open circuit as a function of the temperature difference and the $\Delta T_{2\omega} \times P$ curve.

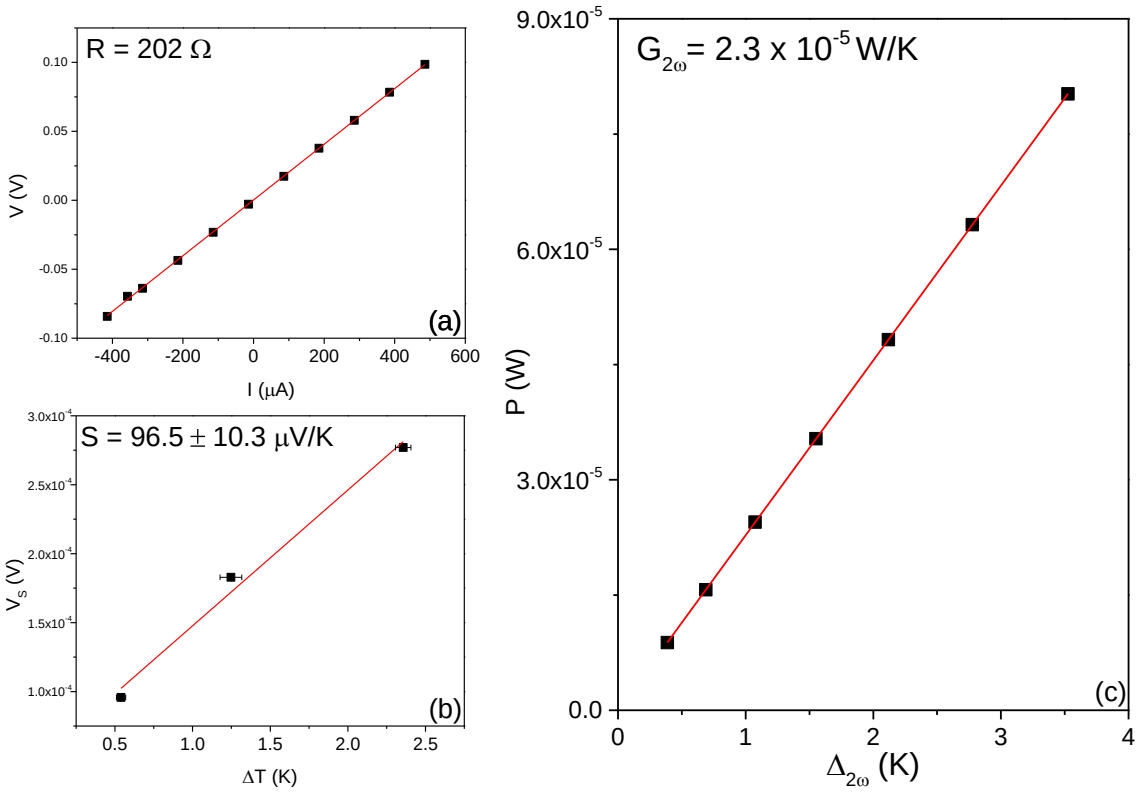

Figure 5.9 Plot of the *IV* curve **(a)**, Seebeck voltage at open circuit **(b)** and $\Delta T_{2\omega} \times P$ curve **(c)** of the $MgAg_{0.95}Ni_{0.005}Sb_{0.99}$ sample. Error bars are smaller than the symbols.

The Seebeck coefficient, electrical and thermal conductivity were determined at room temperature, being, $96.5\,\mu V/K$, $8.9 \pm 1.6 \times 10^4\,S/m$ and $2.0 \pm 0.2\,W/mK$, respectively. The errors in the thermal and electrical conductivity are mostly induced by the uncertainty of the sample thickness. Therefore, a *ZT* value of ~0.13 at 300 K was achieved. Notwithstanding the low *ZT* in relation to bulk samples (~0.9), the sample deposited via sputtering technique is compatible with microfabrication processes. In this way, a thermoelectric generator based on $MgAg_{0.95}Ni_{0.005}Sb_{0.99}$ thin film will be developed and characterized.

5.1.2 Microfabrication of the thermoelectric microgenerator

The thermoelectric microgenerator based on p-type $MgAg_{0.95}Ni_{0.005}Sb_{0.99}$ thin film is microfabricated following the next steps:

i) The process starts with a 4-inch Si wafer with 500 μm of thickness.

ii) A thermal oxidation is performed and 50 nm thick SiO_2 film is achieved.

iii) LPCVD 450 nm thick SiN_X film is deposited.

iv) Photolithography is achieved to pattern the electrical contacts, pads and *n* type legs. The 20 nm thick Cr is deposited then 200 nm thick Pt/Cr is deposited by PVD. Next this process the lift off is performed leading only the Pt/Cr legs and pads.

v) An annealing process is performed at 550 ºC during 2 hours to stabilize the TCR of the Pt/Cr strip.

vi) Photolithography is achieved in the backside to open the window.

vii) RIE is performed to etch the 450 nm thick SiNx and 50nm thick SiO_2 film.

viii) The backside is etched with KOH, leaving only 5-10 µm of Si, which are left to guarantee the survival of the membrane during the cut process.

ix) The wafer is cut in chips of 6 mm x 8 mm.

x) The last 5-10 µm of Si are removed by dropping 5 µL of KOH in the backside during 2 hours at 70 ºC.

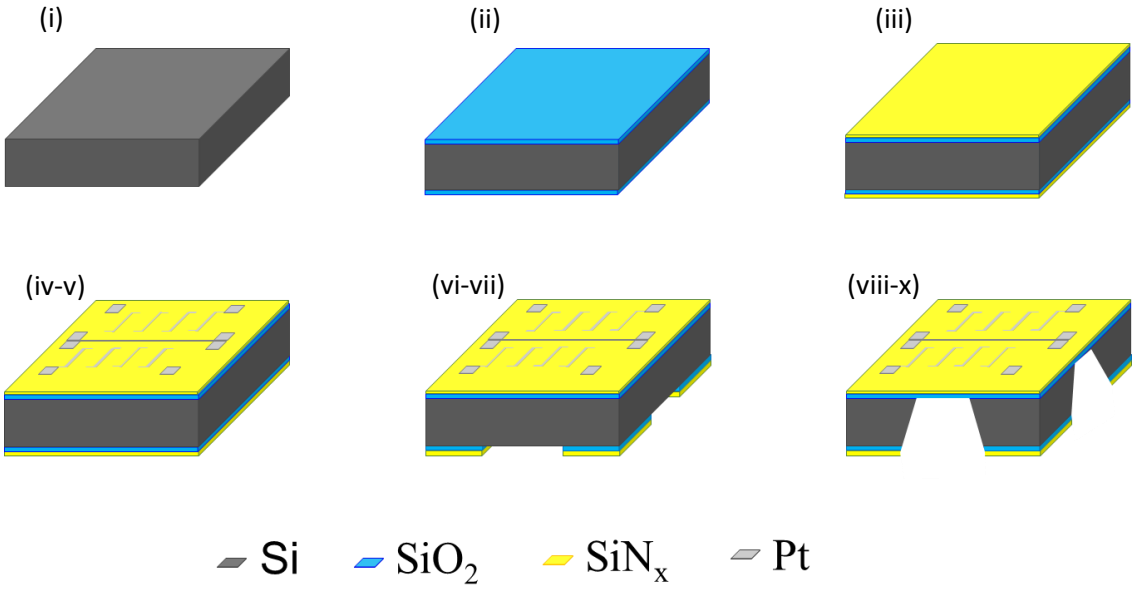

Figure 5.10: The microfabrication steps of the µTEG based on p-type $MgAg_{0.95}Ni_{0.005}Sb_{0.99}$ thin film.

After the microfabrication process, the *p*-type legs are defined by shadow mask and deposited via sputtering. In addition, this device can be used for others *p*-type thermoelectric materials to thermoelectric characterization as well as to produce thermoelectric generator based on these materials.

5.1.3 Device description

The TE legs that conform the *p*-type thermoelectric materials are deposited by sputtering using a shadow mask. The material is grown in similar conditions as those previously reported to yield a thin film material that even does have some impurity phases has a high Seebeck coefficient, high electrical conductivity and low thermal conductivity, as previously discussed in section 5.1.1. To improve the quality, we isothermally anneal the as-deposited layers in high vacuum during 3 days at 600 K.

The device consists of 10 *p*-type thermoelectric legs connected electrically in series and thermally in parallel. The *p*-type leads are connected by Pt metallic lines. The internal resistance of the *n,p* TE legs is around of 7.3 KΩ. This is a much better value (around 10 times lower) than the one obtained for a previous microthermoelectric generator that was built using highly doped ultrathin Si films [67] enabling a better use of the microgenerator in real conditions where the external load should have comparable resistances as the device. In the center of the device a Pt strip that is used as heater to produce temperature gradients is supported by the SiN_x membrane. The good thermal insulation between the frame and the center of the device facilitates the generation of large temperature gradients between the center and the Si frame with low power injections. The TE legs are disposed with part on the frame and part on the membrane. Figure 5.11 shows the optical image of the MgAgNiSb thermoelectric generator.

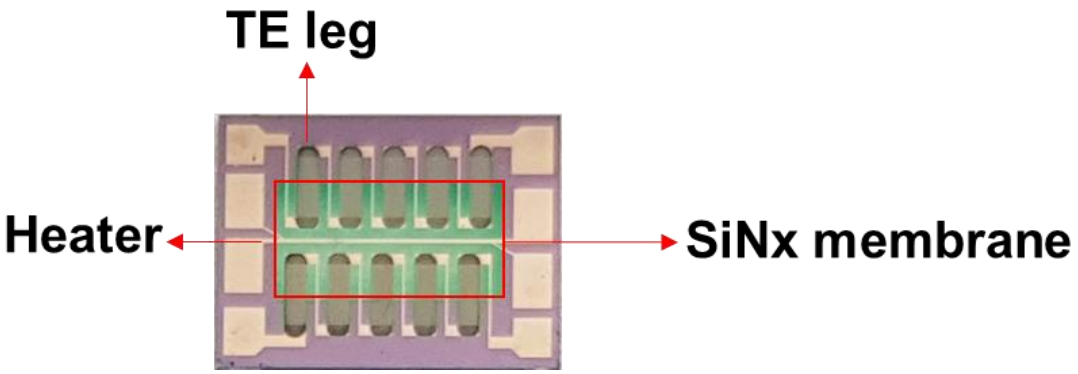

Figure 5.10 Optical image of the MgAgNiSb thermoelectric generator.

5.1.4 Thermoelectric characterization

Prior to the evaluation of the Seebeck coefficient of the device we calibrated the temperature coefficient of resistance of the central metallic strip that we used as a heater. We used the same protocol already explained in Chapter 4 (See Section 4.2.3). Figure 5.11 shows the resistance of the heater at 300 K (a) and the heater resistance at several temperatures.

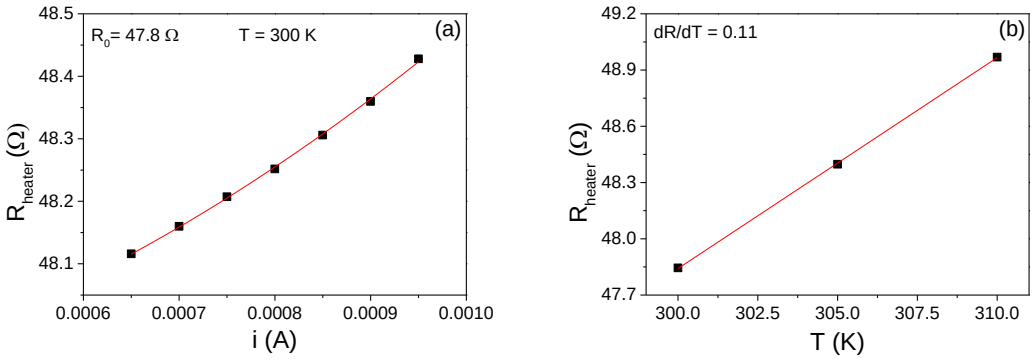

Figure 5.11 (a) IxR measurement of the heater at 300 K and **(b)** R_0 of the heater as a function of the temperature.

To modify the temperature of the hot side (center of the membrane) the heater is fed with electrical currents spanning from 1.3 mA to 2.4 mA, in steps of 0.1 mA, producing temperature differences from 10 K to 34 K between the center and the frame of the device. The generated Seebeck voltage is measured using a nanovoltmeter Keithley 2182a. By the slope of $V_S \times \Delta T$ curves the Seebeck coefficient is measured. Figure 5.12 presents the Seebeck voltage at open-circuit as a function of the temperature difference at an average temperature of 310 K.

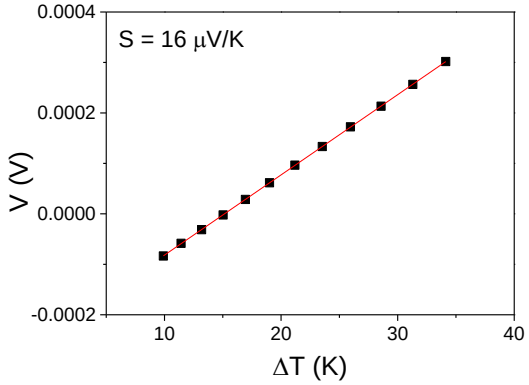

Figure 5.12 Seebeck voltage at open-circuit as a function of the temperature difference at 310 K.

The low value of the Seebeck coefficient, 16 μV/K voltage seems to indicate that the phase that we have deposited is not the intended one. To understand this variation we characterize the as-deposited sample and after annealing for 3 days. As shown by the X-ray diffraction measurement, the as-deposited phase via sputtering is predominantly formed by Sb (16%), Ag_3Sb (83%) and a residual amount of MgAgSb (1%). After annealing the Sb disappears and the main phase is Ag_3Sb (88%) with an increasing amount of α-MgAgSb (12%) with respect the as-deposited state. This is the main reason for the low values of the Seebeck coefficient. Figure 5.13 shows the Rietveld refinement of both samples.

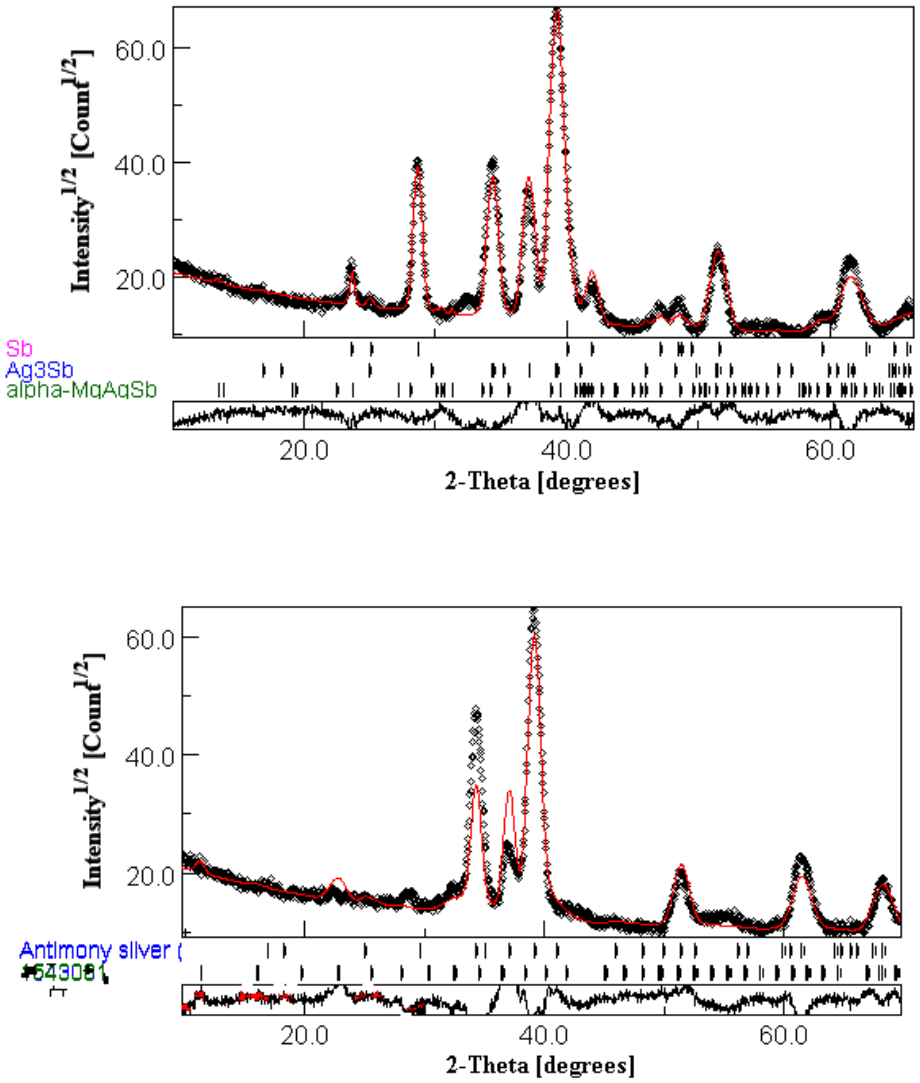

Figure 5.13 Rietveld refinement of the as-deposited **(top panel)** and after an isothermal annealing at low-temperature for 3 days **(bottom panel)**.

5.1.5 Thermoelectric generator characterization

To characterize the device as a generator a load resistor is connected in series and *I-V* curves are obtained changing the values of the load resistor. These measurements are performed maintaining a constant temperature difference across the TE legs. Due to the low value of Seebeck coefficient, high temperature differences are needed to obtain reliable measurements. Using the *I-V* curves, power density curves are determined at each temperature difference. Figure 5.14 shows the *I-V*-curves (a) and power density curves (b) at several temperature differences at base temperatures in the proximity of 310 K.

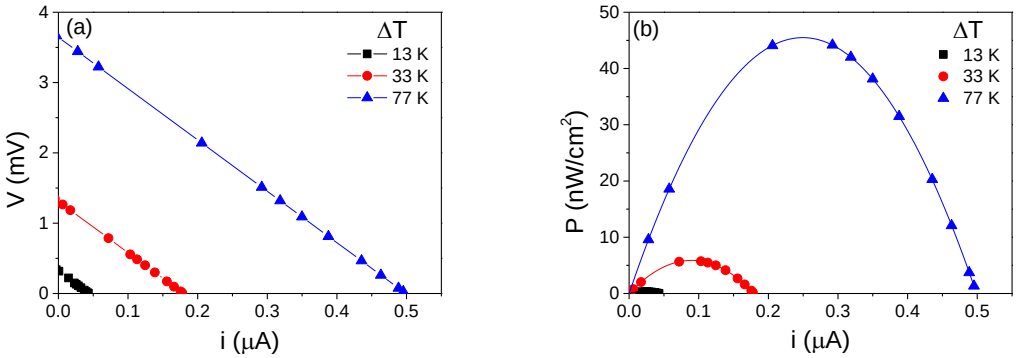

Figure 5.14 Output voltage **(a)** and power density **(b)** versus current for the TEG device at a base *T* of 310 K.

The maximum power is attained when the load resistor has the same value as the internal resistance. A value of 45 nW/cm^2 is reached for a ΔT of 77 K applied to TE legs. The output power of the device is very small due mainly to the low Seebeck coefficient of the deposited films. However, the potentiality that integration of complex materials as thin films offers to build miniaturized devices for sensing or microgeneration is high. Further work to master the sputtering deposition conditions is required to build more efficient devices.

5.2 Conclusions

We have fabricated a first prototype of a planar microthermoelectric generator that contains a suspended structure with a new Mg-based *p*-type material as the active TE material. Since thin film growth can be performed as the last step of the microfabrication process the outlined procedure can be integrated into standard Si chips. A power output of 4.5 nW/cm^2 was achieved under a temperature difference of 77 K. Even that we have not been able to obtain the desired phase in pure form this approach will be the basis for

future microdevices based on complex alloys. The low thermal conductivity of the propose material (below 2 $Wm^{-1}K^{-1}$) will enable large temperature differences. In addition, the proposed design permits the fabrication of multiple optimized generators on a single wafer to be connected in series to boost the voltage performance or in parallel to increase current output to match the desired application.

6. Thermoelectric characterization of polymer films via in-plane measurements

Organic semiconductors show unique processing advantages with respect to its inorganic counterparts. The low cost, processability, high conductivity and the adaptability to curved surface have driven conducting polymers as excellent candidates for many applications in organic electronics, ranging from solar cells to organic field effect transistors (OFETs) or thermoelectric sensors or generators [95–99]. Flexibility is one of the leading properties that is paving the way to employ conducting polymers to develop a new generation of flexible displays and devices. Besides that, due to their nontoxicity and biocompatibility many of these conducting polymers can be applied in wearable or implantable devices as energy source for low power devices [100,101] or for sensing. Of course, the main drawback of using polymers for electronic applications is related to their inherently low electrical conductivity compared with doped inorganic semiconductors. However, recent progress in semiconducting polymers has led to carrier mobilities exceeding that of amorphous silicon [102]. Also recently, a variety of polymers have been investigated as suitable candidates for thermoelectric applications due to their promising high values of power factor that together with the low values of thermal conductivity have boosted the enhancement of the figure of merit (*ZT*) of these materials to values approaching 0.5 at room temperature [103]. Doping with carbon nanotubes or BiTe platelets, nanowires or nanoparticles is a good strategy to enhance *ZT* [104–112]. Determination of *ZT* often requires independent measurements of all its variables, i. e. Seebeck coefficient, electrical conductivity and thermal conductivity on the same sample. This is a challenging task since most often electrical and Seebeck coefficient are measured in the in-plane direction while the thermal conductivity is most easily measured in the out-of-plane direction. This is not a big issue for isotropic materials where both in-plane and out-of-plane values are similar. But in polymers anisotropy is often encountered. On one side long polymer chains are by nature highly anisotropic with dimensions along the chain axis much larger than the ones associated to the transversal axis. In addition, standard fabrication procedures such as spin cast favor anisotropy with chains more oriented parallel to the substrate. In extreme cases in which chain alignment is highly favored by specific approaches such as electropolymerization inside the aligned nanopore

channels of anodic alumina templates [113], thermal anisotropy ratios, i. e. the ratio between the longitudinal (in-plane) and the transversal (out-of-plane) thermal conductivities, can be as large as 100. It is clear than when anisotropy exist it is necessary to measure the figure of merit in the same direction, in-plane or out-of-plane, for the three variables. However, the in-plane measurement of *k* is very challenging, and many authors rely on indirect measurements or even they wrongly use the out-of-plane value of *k* and the in-plane values of S and σ.

Thus, for a correct thermoelectric characterization of the polymeric films, the thermal conductivity should be determined in the same direction that is considered for the Seebeck coefficient and electrical conductivity. However, several previous works have reported the difficulties to measure the in-plane thermal conductivity of polymeric films, obtaining its value by using the relation between the out-of-plane and in-plane thermal conductivities and considering that the Wiedmann Franz law is valid [114,115].

In this chapter, we explore the applicability of the 3ω-Völklein method in obtaining reliable values of the in-plane thermal conductivity of polymeric films. To this aim we choose PEDOT:PSS (Poly(3,4-ethylenedioxythiophene)-poly(styrenesulfonate)) thin films as a model system with a relatively high figure of merit. In addition, a complete thermoelectric study of the PEDOT:PSS thin films doped with DMSO (dimethyl sulfoxide) is also performed. The aim of our study is not to obtain a material with a high *ZT* but rather to confirm our capability to obtain a true *ZT* value of the parallel component with all parameters measured in the same direction. Remarkably, the lattice component of the in-plane thermal conductivity of the PEDOT:PSS thin films does not obey a linear behavior as a function of the doping level challenging previous observations in thicker materials [114].

6.1. PEDOT:PSS (doped with DMSO)

PEDOT is a *p*-type polymer with a conjugated chain that has been extensively studied due to its high electrical conductivity. However, despite its good electrical properties, PEDOT is an insoluble polymer, and a counter ion is required to prepare it in aqueous solution. PSS (poly(styrenesulfonate)) is very often used to stabilize PEDOT, in PEDOT:PSS form [116–118]. The addition of PSS allows to solubilize the PEDOT in polar solvents, but in contrast it reduces the electrical properties of pristine PEDOT, since PSS is an insulate polymer.

PEDOT:PSS is one of the most important and employed conducting polymers in thin film form with a high figure of merit [119,120]. PEDOT:PSS shows outstanding features, such as biocompatibility, non-toxicity, good thin film-formation by different techniques, high transparency in the visible range, excellent thermal stability, and the facility to tune its electrical conductivity over orders of magnitude by secondary doping. Owing to the good electrical conductivity, the thermoelectrical properties of PEDOT:PSS have been studied as well as the possibilities to improve them. The addition of solvents (secondary doping) in the polymeric solution changes the interaction between PEDOT and PSS chains and is a very successful approach to change the amount of charge carriers (secondary doping) [121–123]. PEDOT:PSS can be heated in air at 100ºC for more than 1000 h without variation of the electrical conductivity. In fact, the influence of temperature and solvents on the transport properties of thin and thick films of PEDOT:PSS have been deeply investigated [102]. It is generally found that transport is highly anisotropic with two orders of magnitude variation in the electrical conductivity, being lower in the cross-plane direction. Likewise, the in-plane thermal conductivity $k_{\parallel}$ of thin films was also found to be anisotropic and dependent on the charge carrier density in agreement with the Wiedemann−Franz law. The validity of such relation for the cross-plane thermal conductivity $k_{\perp}$ is not clear yet.

In the next section we evaluate the thermoelectric properties of the PEDOT:PSS thin films doped with DMSO. Figure 6.1 shows the molecular structure of PEDOT:PSS and DMSO.

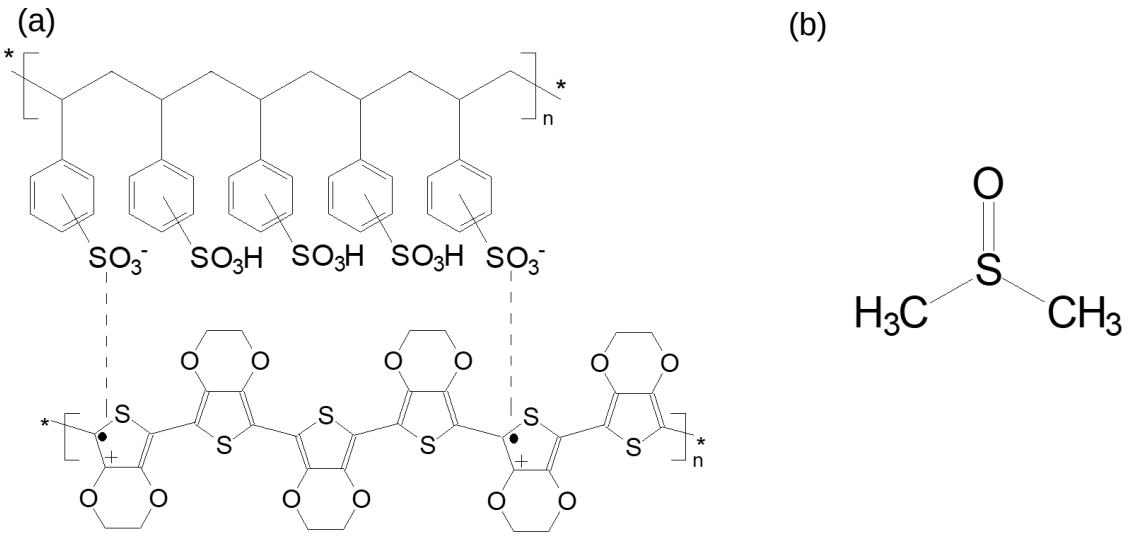

Figure 6.1 Molecular structure of PEDOT:PSS (a) and DMSO (b).

6.1.1 Sample Preparation

Two batches of PEDOT:PSS samples were prepared using the spin-coating technique. The spin-coating is a technique widely used to produce homogeneous thin films of polymers with variable thickness depending on the final rotation speed, acceleration and time. The solvent, the viscosity and the substrate treatment also play a crucial role. The technique consists in dropping a polymeric solution on the substrate and then rotate the substrate during a given time. During the spinning process the solvent evaporates leading to a homogenous thin film. Figure 6.2 shows the schematics of the steps of the spin-coating technique.

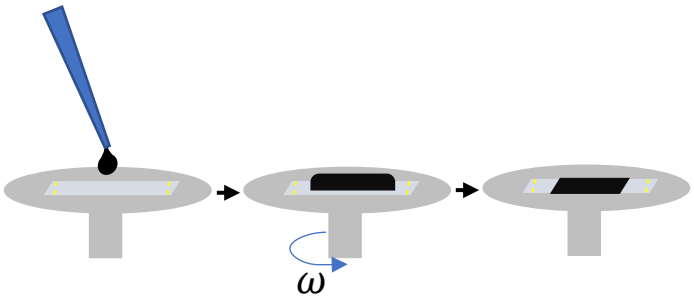

Figure 6.2 Steps of the spin-coating technique.

The first batch of samples is prepared to verify the applicability of the 3ω-Völklein method in the study of the in-plane thermal conductivity of polymeric materials. The PEDOT:PSS solution, Clevios PJ 700 (50% PSS), was purchased from Sigma Aldrich. After, three PEDOT:PSS thin films were deposited controlling the rotation per minute to obtain films with thickness 110 nm ± 10 nm. The electrical conductivity of the films was around $2{,}7 \times 10^4$ S/m. These samples were prepared in collaboration with Marco Cassinelli and Mario Caironi from the Printed and Molecular Electronics (PME) group at the Center for Nano Science and Technology @Poli-Milan.

Besides that, another batch of the PEDOT:PSS thin films doped with DMSO were prepared by spin coating technique in collaboration with Ll. Abad from the Instituto de Microelectrònica de Barcelona-Centro Nacional de Microelectrónica (IMB-CNM) from CSIC located at UAB campus. The second batch was prepared in order to verify the influence of DMSO in the thermoelectric properties of the PEDOT:PSS thin films. The base solution of high conductivity PEDOT:PSS in aqueous solution with 3-4% concentration was purchased from Sigma Aldrich and was posteriorly doped with several concentration of DMSO, 2%, 5% 6.5% and 8% in volume (See Table 6.1). The solutions were prepared by adding DMSO in PEDOT:PSS solution and then the solutions were

homogenized using a magnetic stirrer during 2 hours. The samples were deposited via spin-coating at 4000 rpm during 1 min. After the deposition, the samples were annealed at 80 ºC during 20 min on a hotplate in ambient atmosphere, drying fully the solvent. These samples were deposited on a 3ω-Völklein sensor, also in devices to measure the Seebeck coefficient and electrical conductivity. In the case of the 3ω-Völklein sensor, a previous treatment was performed to hydrophilize the deposition surface, it is important to obtain homogenous sample. Thus, before the spin-coating deposition, the sensor is treated during 2 min with a solution prepared of hydrogen peroxide, ammonium hydroxide and deionized water in volume of 5:1:1, respectively. After this process, the device is cleaned with deionized water and dried inside a furnace at 60 ºC during 5 min in atmosphere ambient. The devices used to measure the Seebeck coefficient and electrical conductivity were pre-cleaned with iso-propanol, acetone and deionized water.

Table 6.1: PEDOT:PSS samples doped with DMSO.

Rotation (RPM)	Time (s)	PEDOT:PSS (%)	DMSO (%)
4000	60	100	0
4000	60	98	2
4000	60	95	5
4000	60	93.5	6.5
4000	60	92	8

6.2 In-plane thermal conductivity of PEDOT:PSS films

In order to verify the ability of the 3ω-Völklein method to measure the in-plane thermal conductivity of polymers, three reference samples of PEDOT:PSS prepared from the commercial formulation Clevios PJ700 were deposited by spin coating on the 3ω-Völklein sensors. As explained in chapter 3, to determine the in-plane thermal conductivity of the sample, the in-plane thermal conductance of the membrane should be determined before sample deposition. After the polymer layer is spin-cast the measurement yields the in-plane thermal conductance of the sample plus membrane. Thus, the thermal conductance of the thin film is determined subtracting the contribution of the membrane's thermal conductance from the total thermal conductance. The thermal

conductances are obtained through the slope of $\Delta T_{2\omega} \times P$ curves. Figure 6.3 shows the $\Delta T_{2\omega} \times P$ curves for the membrane alone (m) and the membrane + PEDOT:PSS samples (s + m), both measured at room temperature.

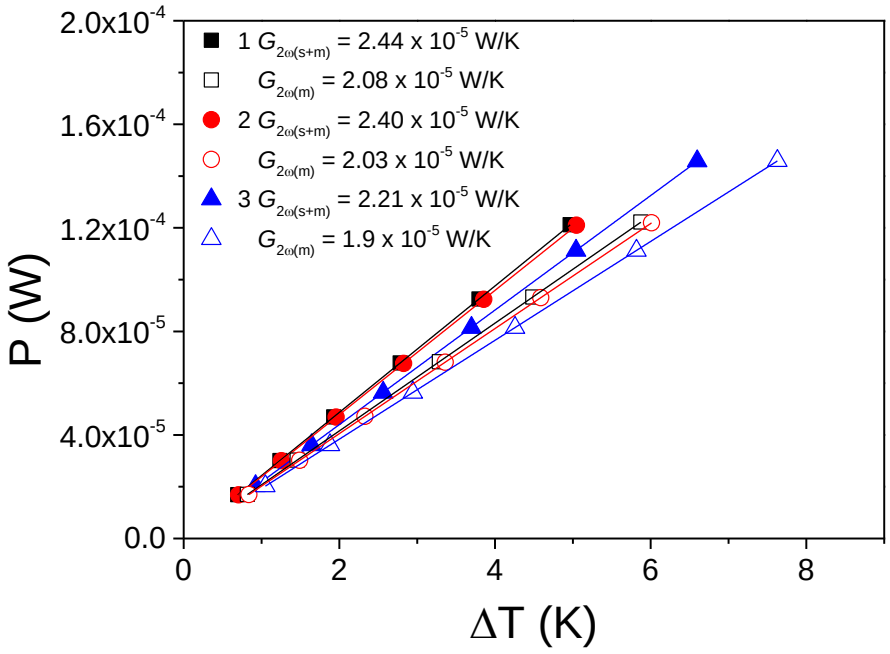

Figure 6.3 Plot of $\Delta T_{2\omega} \times P$ curves of the membrane (m) and PEDOT:PSS samples (s + m) with contribution of the membrane at room temperature.

Once the thermal conductance of the sample is known, the in-plane thermal conductivity is determined considering the sample dimensions. The in-plane thermal conductivities of three PEDOT:PSS reference samples measured at room temperature are shown in Table 6.2.

Table 6.2: In-plane thermal conductivities of PEDOT:PSS films. Error bars are mostly due to the uncertainty of the sample thickness.

Sample	$k_{\parallel}$ (W/mK)
1	1.02 ± 0.10
2	1.05 ± 0.10
3	0.86 ± 0.10

It is important to compare these values with previous literature data, both cross-plane and in-plane on PEDOT:PSS. In-plane measurements are scarce and they are often

conducted on micron thick films. Liu and coworkers [114] measured the in-plane and cross-plane thermal conductivity of drop-cast PEDOT:PSS films of thickness 40 µm and the $k_{\perp}$ for much thinner spin-cast layers. For pristine drop-cast PEDOT:PSS $k_{\perp}$=0.3 $Wm^{-1}K^{-1}$ and was independent of the value of the electrical conductivity, while the $k_{\parallel} \cong 0.75\ Wm^{-1}K^{-1}$ and largely depends on the dopant concentration (i. e. on the electrical conductivity). The anisotropy ratio, $k_{\parallel}/k_{\perp}$, of the pristine sample is 2 and raises to 3 for more conductive samples ($\sigma \approx 6x10^4$ S/m). The cross-plane of the 65 nm spin-cast films was 0.29 $Wm^{-1}K^{-1}$ and was also independent of the dopant concentration.

Wei et al. [124] used a freestanding film with a thickness larger than 10 µm and a commercial technique to determine the cross and in-plane thermal diffusivities of PEDOT:PSS with different post-treatments (and therefore with different electrical conductivities). PEDOT:PSS with σ=170 S/m had $k_{\parallel}$=0.55 $Wm^{-1}K^{-1}$ and $k_{\perp}$=0.15 $Wm^{-1}K^{-1}$, while the sample with $\sigma=8x10^4$ S/m had $k_{\parallel}$=0.94 $Wm^{-1}K^{-1}$ and $k_{\perp}$=0.20 $Wm^{-1}K^{-1}$, respectively. Both samples exhibited important anisotropy ratios around 4. On the other hand, Greppmair et al. [125] used a thermography technique to estimate the in-plane thermal conductivity by measuring the temperature distribution along the thin film fitted to an analytical expression of heat transfer for the specific geometry. For thin films of PEDOT:PSS post-treated with ethylene glycol (with $\sigma=7{,}2x10^4$ S/m) they found a value of 1.0 $Wm^{-1}K^{-1}$ for the room temperature in-plane thermal conductivity.

Beretta et al. [115] have used an indirect estimation to infer the value of the in-plane thermal conductivity, $k_{\parallel}$= 1.09 W $m^{-1}K^{-1}$. They measured σ‖ and $k_{\perp}$ to be $2{,}7x10^4$ S/m and 0.45 W $m^{-1}K^{-1}$, respectively and used $k_{\parallel} = k_{\parallel,ph} + k_{\parallel,el}$ with $k_{\parallel,ph}=2\ k_{\perp,ph}$ and $k_{\parallel,el}= \sigma\parallel LT$. L is the Lorentz number $L= 2.44 \times 10^{-8}\ W\Omega\ K^{-2}$.

The values of $k_{\parallel}$ highlighted in Table 6.2 are in very good agreement with the previous literature values, validating the use of the 3ω-Völklein method developed at the Nanomaterials and Microsystems Group as a suitable technique to determine parallel to the plane thermal conductivities in polymeric thin films.

6.3 Thermoelectric characterization of PEDOT:PSS films doped with DMSO

A batch of PEDOT:PSS thin films were deposited by spin coating technique with different dimethyl sulfoxide (DMSO) concentrations (Table 6.1). As reported by Luo et al., the addition of DMSO in PEDOT:PSS solution improves the electrical conductivity of the PEDOT:PSS films, whereas the Seebeck coefficient value changes only slightly with the amount of DMSO [119]. Thus, this is a way to enhance the power factor of the PEDOT:PSS films, enabling potential applications in thermoelectric devices. Figure 6.4 shows the electrical conductivity of the PEDOT:PSS films doped with several DMSO concentrations at room temperature. Results obtained by other authors in previous works are also shown for comparison [121–123].

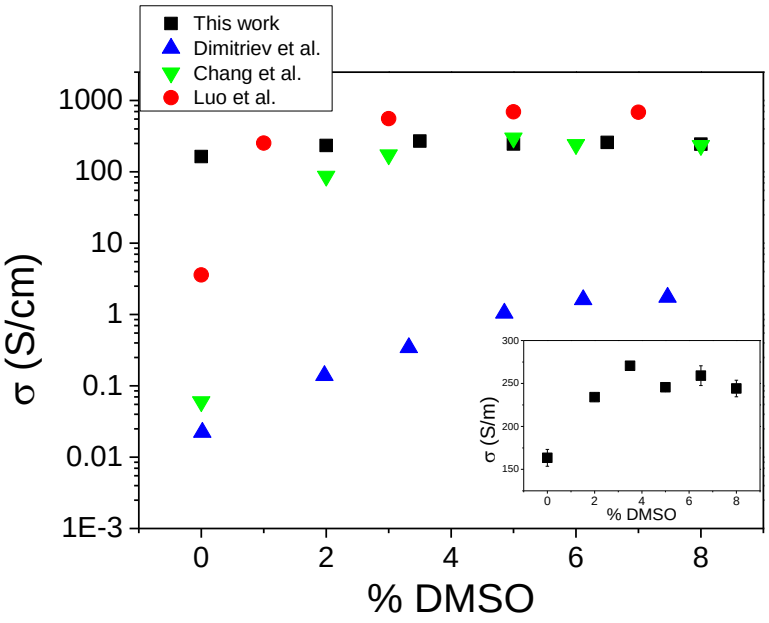

Figure 6.4 Plot of the electrical conductivity of PEDOT:PSS films as a function of DMSO concentration. The errors bars are due to variations in sample thickness along the length of the sample. Data from Dimitriev et al. [121], Chang et al. [122] and Luo et al. [123] included to comparison. The results obtained along this PhD thesis are zoomed in the inset.

Comparing our results with previous literature data, it is possible to observe that the electrical conductivity of the PEDOT:PSS films exhibit a common behavior as a function of the DMSO concentration for all of them, that is, the electric transport obeys a logarithmic function of the DMSO concentration that reaches a maximum around 6.5% [121–123]. The previous works are performed using different PEDOT:PSS solutions, the

mainly difference is the ratio between the PEDOT and PSS molecules, thus, the electrical conductivity values are different. It is known that in pristine form, the insulating PSS chains interact with conductor PEDOT in a coiled structure, yielding a low electrical conductivity. As reported by Zhu et al., the polar solvent molecules as DMSO weak the Coulombic interaction between PEDOT and PSS molecules, separating and uncoiling the PEDOT and PSS molecules. This molecular conformation creates a way to the charge transport, improving the electric conductivity of the PEDOT:PSS films [126].

After these measurements, the Seebeck coefficient of the PEDOT:PSS films were determined using a homemade system (Section 3.2.1). Therefore, the Seebeck voltage at open-circuit is measured as a function of the temperature difference and by fitting the $V_S \times \Delta T$ curve the Seebeck coefficient of each film is obtained (see Section 3.2.1). Figure 6.5 shows the Seebeck coefficient of the PEDOT:PSS thin films as a function of the DMSO concentration at room temperature.

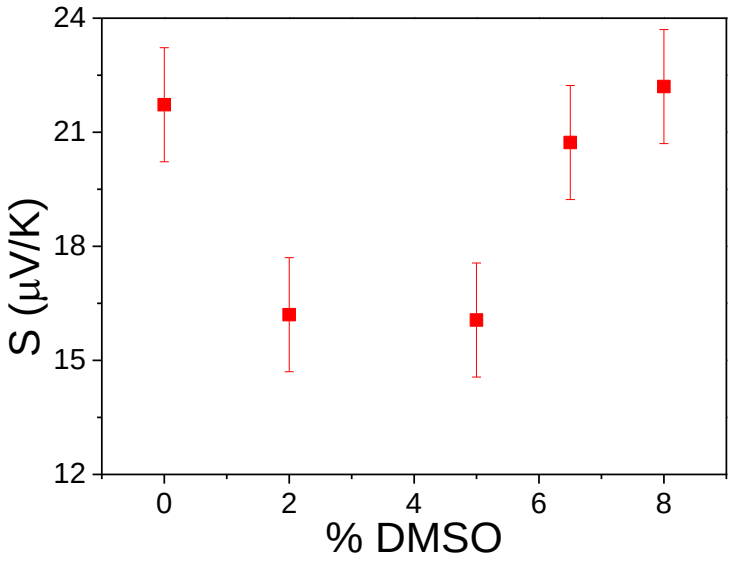

Figure 6.5 Seebeck coefficient of PEDOT:PSS films as a function of DMSO concentration.

By inspection of Figure 6.5 it is possible to verify that the Seebeck coefficient is slightly affected by DMSO concentration, remaining almost constant as a function of DMSO concentration. Previous works reported contradictory behaviors of the Seebeck coefficient due to the solvent concentration, i. e., Luo et al. and Yee et al. observed a

slightly reduction as a function solvent concentration while Kim et al. verified an improvement of the Seebeck coefficient [103,111,123,127].

Using the Seebeck coefficient and electrical conductivity we derive the *PF* of the PEDOT:PSS thin films as a function of DMSO concentration, which is presented in Figure 6.6.

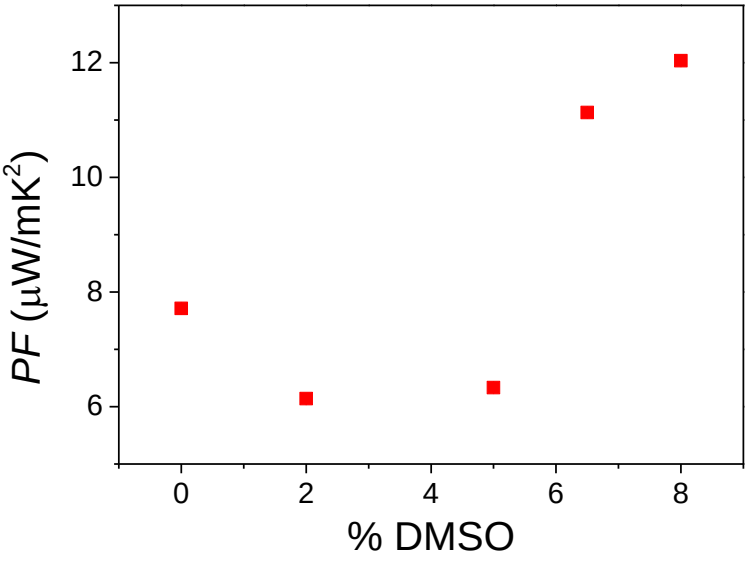

Figure 6.6 *PF* of PEDOT:PSS films as a function of DMSO concentration.

In our measurements the maximum value of *PF* is 12 μW/mK^2, which is reached at 8% of solvent. This value is lower than the one reported by Luo et al. In their case the optimized power factor by DMSO addition of 5% is 18.2 μW/mK^2 while it increases to 30.1 μW/mK^2 for the film with DMSO post-treatment. This difference is mainly caused by the values of electrical conductivities attained in our work that are 2 times lower than the electrical conductivities obtained by Luo et al. (see Figure 6.4) [123].

Next, the in-plane thermal conductivity of the PEDOT:PSS samples doped with DMSO were determined by the 3ω-Völklein method. Figure 6.7 shows the in-plane thermal conductivity of the several doped PEDOT:PSS films at 300 K.

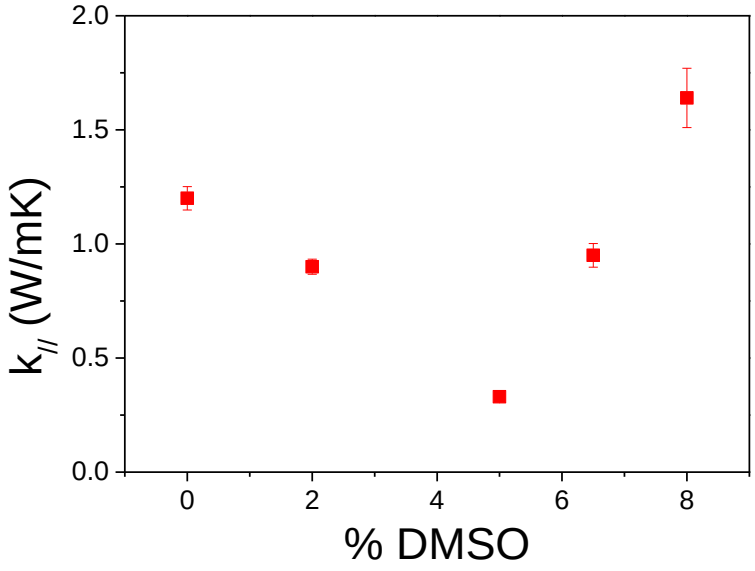

Figure 6.7 In-plane thermal conductivity of PEDOT:PSS films as a function of DMSO concentration. The errors are calculated from the uncertainty in the sample thickness.

There is a clear reduction of $k_{\parallel}$ by DMSO addition of 2% and 5% and a rise when the DMSO concentration reaches 6.5% and 8%. In previous works, $k_{\parallel}$ of the PEDOT:PSS thick samples show a linear trend with increasing doping [114]. In those measurements, the lattice contribution remained constant and the linear increase of $k_{\parallel}$ was attributed to the electronic carriers. In fact, the increase was shown to obey the Wiedmann-Franz law (Equation 2.17). Our measurements of $k_{\parallel}$ in very thin films show a remarkably different behavior, as shown in figure 6.7, with a 6-fold variation of $k_{\parallel}$ and a minimum at an intermediate doping level.

In another study with post-treatment, Kim et al. reported that the out-of-plane thermal conductivity of PEDOT:PSS thin films was reduced due to the removal of PSS chains. This reduction can be associated to the increase of van der Waals bonding with respect to covalent bonds as PSS is removed. Since PSS chains are larger than PEDOT molecules removal of PSS leads to more vdW interactions. The efficiency of heat transmission depends heavily on the strength of the bonding with weaker bonds leading to more inefficient heat transfer between molecules/chains [128]. Therefore, PSS reduction results in a decrease of the thermal conductivity [103].

In contrast in our case, the PEDOT:PSS ratio remains constant. Nevertheless, DMSO acts as a structural dopant that enters into the PEDOT:PSS chains and allows a reorganization of the PEDOT molecules, partially insulating the PSS chains, what may produce variations of the lattice contribution of $k_{\parallel}$ [129–132].

If we consider that the Wiedemann-Franz law is valid, the electronic contribution of $k_{\parallel}$ can be calculated. Then, subtracting the electronic contribution from the total in-plane thermal conductivity, the lattice contribution is readily obtained. The electronic contribution increases as a function of the DMSO concentration in the same way as the electrical conductivity, while the lattice contribution decreases reaching a minimum value at a DMSO concentration of 5% to increase again for higher doping levels. The change in k_{lattice} is remarkable since at 5% reaches an outstanding low value of 0.15 $Wm^{-1}K^{-1}$ while at 8% increases to 1.48 $Wm^{-1}K^{-1}$. While we do not have yet a clear microscopic picture of the changes in chain conformation of the PEDOT:PSS with DMSO addition, we suspect there is an enhanced corrugation of the chains that impedes thermal flow in the parallel direction.

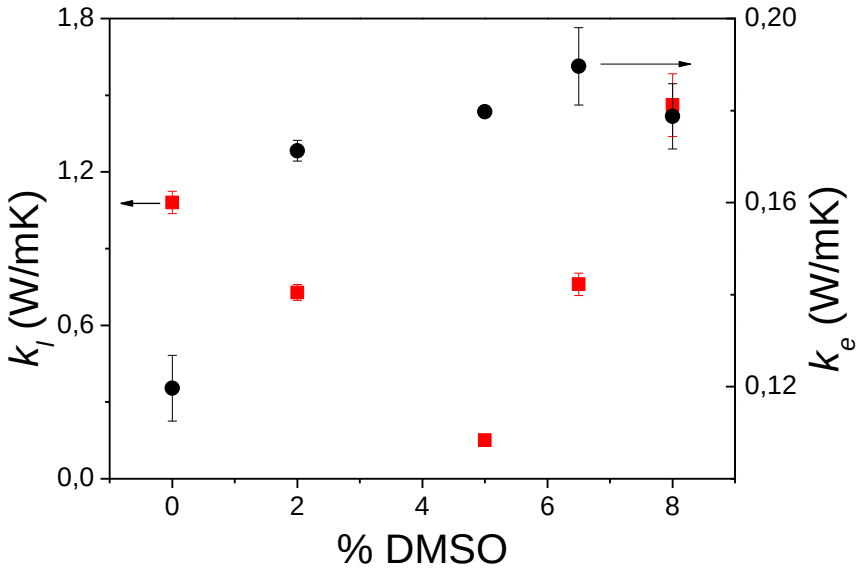

Figure 6.8 Lattice and electronic contribution of the in-plane thermal conductivity of PEDOT:PSS films as a function of DMSO concentration. The errors are induced by the uncertainty in the sample thickness.

Using the thermoelectric parameters independently measured: Seebeck coefficient, thermal and electrical conductivities, a full thermoelectric characterization of

the PEDOT:PSS films as a function of the DMSO concentration has been realized at 300K. The *ZT* values of the PEDOT:PSS films as a function of the DMSO doping level are presented in Figure 6.9.

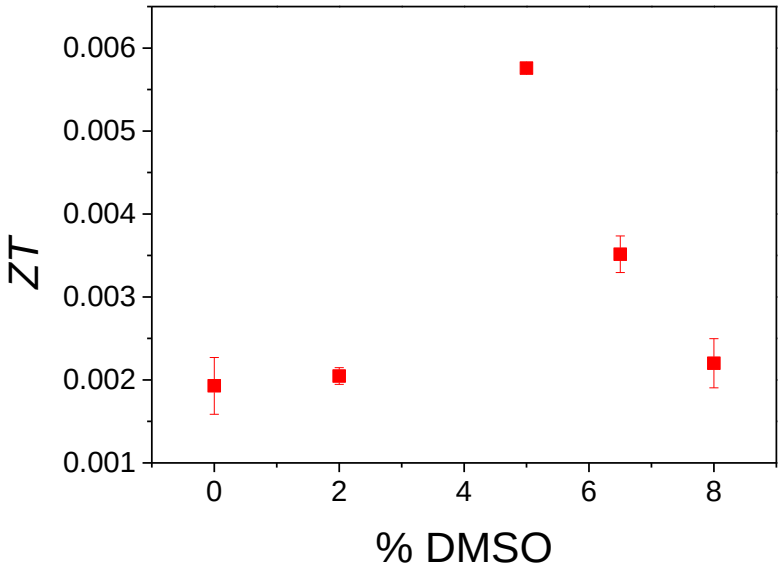

Figure 6.9 *ZT* of the PEDOT:PSS films as a function of DMSO concentration.

The reduction in the in-plane thermal conductivity of the PEDOT:PSS films caused by DMSO doping plays an important role in the *ZT* value, since the Seebeck coefficient is nearly constant, the electrical conductivity increases for all doping level whereas the thermal conductivity is reduced at 2% and 5%. Therefore, the sample at 5% of DMSO concentration reaches a *ZT* value of $\sim 6 \times 10^{-3}$, 3-fold larger than values at other doping levels. As discussed earlier the goal of this chapter was not to obtain a polymer with a high *ZT* but rather to highlight the importance of measuring the in-plane thermal conductivity to obtain real values of the figure of merit in the direction parallel to the substrate. Many authors use in-plane Seebeck and electrical conductivities and cross plane thermal conductivities to infer *ZT*. This is the case of the work of Luo et al. that assume a very low value of the thermal conductivity of PEDOT:PSS k=0.17 $Wm^{-1}K^{-1}$ [123], based on previous measurements by Jiang et al. [133].

6.4 Conclusions

We have verified the applicability of the 3ω-Völklein method to determine the in-plane thermal conductivity of polymeric thin films. We believe this technique may fill the gap that existed up to now enabling faster, easier and more precise and direct measurements since the 3ω-Völklein technique directly measures the thermal conductance. Other techniques measure thermal diffusivity and rely on the density and heat capacity to obtain the thermal conductivity of the material. In addition, in other cases the value of $k_{\perp}$ is used to estimate the in-plane conductivity assuming a standard value of the anisotropy ratio that may not be appropriate for each specific material yielding incorrect values of the figure of merit. Our results show that the thermal conductivity obtained for the reference samples are in very good agreement with previous literature data.

Besides that, we have demonstrated that the technique is very sensitive to variations in $k_{\parallel}$ induced by secondary doping. In particular, the addition of DMSO significantly influence the thermoelectric properties of the PEDOT:PSS thin films. The Seebeck coefficient, electrical and thermal conductivities were measured as a function of DMSO concentration. In agreement with previous data, the Seebeck coefficient remains almost constant as a function of DMSO concentration and the values of electrical conductivity obey a logarithmic function, increasing the electrical conductivity as the DMSO concentration increases. However, the in-plane component of k_{lattice} of the PEDOT:PSS thin films does not obey a linear behavior as a function of the doping level as reported in previous work for thicker layers. The possible reason to the reduction of the in-plane k_{lattice} is the separation of the PEDOT and PSS molecules caused by the DMSO, that can heavily impede the heat flux in parallel direction with the addition of 5% of solvent.

7. Conclusions

This thesis follows the tradition of previous PhD works at GNaM trying to combine the development and/or application of new techniques or devices together with a strong interest in the materials characterization and development. In this thesis, we have studied the thermal transport and thermoelectric properties of variety of thin film materials ranging from organic polymers to inorganic semiconductors. The 3ω-Völklein method has been shown to be a reliable tool to measure the in-plane thermal conductivity of organic thin films opening an interesting avenue for such type of measurements that up to now were scarce in the literature because of the inherent difficulty to carry out precise measurements. In addition, a homemade measuring system including devices to measure the thermopower, as well as the electrical conductivity were designed, fabricated and tested along this thesis. Several microthermoelectric devices on-purpose designed and microfabricated to incorporate thermoelectric legs of a variety of materials were also developed along this work. It is worth to note the effort spent in building and characterizing a photothermoelectric device based on n and *p*-type Si thin films.

The use of the Si-based μTEG as photosensor was reported. The low thermal mass of the sensing zone, together with the high thermal insulation caused by the reduced thickness of Si allowed to obtain a sensor with quick response time and excellent responsivity of 13 *V/W*. During these measurements an unexpected enhancement of the Si thermopower apparently caused by the generation of photocarriers was evidenced. In this way, a study of the simultaneous effect of photovoltaics and thermoelectric phenomena and its influence on the Seebeck coefficient was undertaken. For this purpose, a new device with a better temperature profile was designed and microfabricated to guarantee better and more reliable measurements of the Seebeck coefficient. Several experiments using a focused laser beam that locally heats the thermoelectric materials besides generating a huge amount of photoinjected carriers were performed. Those experiments demonstrated a variation of the thermopower up to around 10% for the *p*-type Si thermoelectric legs under illumination. The experimental study was complemented by Finite Element Modelling simulations that indicated the existence of a pure thermal effect that leads to a voltage offset due to charge accumulation. However, no variation of the thermopower is obtained in the modelling data. Overall, this study

shows that the photoinjected carriers and the generated temperature difference do play a key role in the observed enhancement of the thermopower. One possible reason of the variation of *S* could be related to a phonon drag effect that is more effective with the heavier majority carriers (in the *p*-type material) leading to an unbalanced in the charge distribution and charge accumulation at the contacts.

An important effort has been dedicated to try to produce thin films of pure MgAgSb alloys, since these materials have been already synthesized in bulk form showing high figure of merits. MgAgSb-based samples were deposited via sputtering technique in order to obtain films with the desired stoichiometry and hopefully with high *ZT* value as the bulk counterparts. The great advantage of this technique in relation to the standard techniques used to fabricate those samples (mechanical alloying + sintering and/or hot pressing) is its compatibility with microfabrication process and the development of planar devices. Several MgAgSb thin films with a small amount of Ni were morphologically, structurally and thermoelectrically characterized. Unfortunately, is spite of the many runs and processed samples the desired single phase was not obtained leading a low value of the Seebeck coefficient. In spite of this shortcoming, a planar prototype thermoelectric generator was designed, microfabricated and tested paving the way for future studies in other *p*-type thin film materials.

The applicability of 3ω-Völklein method to determine the in-plane thermal conductivity of polymeric films was demonstrated. The in-plane thermal conductivity of PEDOT:PSS reference samples were in very good agreement with values reported by other authors in the literature. Moreover, the in-plane *ZT* of PEDOT:PSS films doped with several DMSO concentration were measured. The Seebeck coefficient remained almost constant, while the electrical conductivity showed a logarithmic behavior as function of the doping level, similarly to other reports. On the contrary, the in-plane thermal conductivity measurements did show some interesting and unexpected behavior. The lattice component of the in-plane thermal conductivity of the thin films (around 100 nm) exhibits a pronounced minimum at around 5% of DMSO addition, in contrast to previous data on much thicker materials (20 μm thick) that follow a linear behavior with the amount of DMSO. The reason for the observed decrease is probably related to chain misalignment and separation due to the interaction of DMSO with the PEDOT:PSS chains. Therefore, a peak in the *ZT* value was obtained in PEDOT:PSS layers with 5% of DMSO.

8. Supplementary Information

8.1 FEM simulations

This simulation method consists in solving the system partial differential equation (PDEs) on infinitesimal pieces of the geometry mesh. Using the meshed geometry, the physical magnitudes are iteratively solved in the partial differential equations of the simulated system. In general, when leading with very asymmetric structures, like ultra-thin membranes where one of the distances (in that case the out of plane) is very different to the rest, the mesh should be adapted to the most restrictive one to facilitate the solution convergence stability. Unfortunately, in such structures it results into a highly dense mesh that requires a large memory and computational demand to be solved. The strategy to overcome such a limitation is to reduce the 3-dimensional problem to a 2D one, defining a constant vertical thickness of the mesh and rewriting the PDEs.

In the problem presented here in, we have considered in a first instance the PDEs of the heat transfer with in the plane of the sample, the Maxwell equation for electrical evolution, including the thermoelectrical effects.

$$d_z \rho C_p \boldsymbol{u} \nabla \cdot T = \nabla \cdot (d_z k \boldsymbol{u} \nabla T - p\boldsymbol{J}) + d_z Q \quad \text{(S1.a)}$$

$$\nabla \cdot \boldsymbol{J} = Q_j \quad \text{(S1.b)}$$

$$\boldsymbol{J} = \sigma \boldsymbol{E} + J_e \quad \text{(S1.c)}$$

$$\boldsymbol{E} = -\nabla \mathrm{V} \quad \text{(S1.d)}$$

where d_z is the term related to lumped, that in our case is the thickness of the thermoelectric active layer, ρ is the density, C_p is the heat capacity at constant pression, T is the temperature, k is the thermal conductivity, $\boldsymbol{u}$ is the velocity field, p is the Peltier coefficient, J is the current density, Q is the joule heating, σ is the electrical conductivity, $\boldsymbol{E}$ is the electrical field, V is electrical potential.

9. References

(1) *Key World Energy Statistics 2018*; Key World Energy Statistics; OECD, 2018. https://doi.org/10.1787/key_energ_stat-2018-en.

(2) Papapetrou, M.; Kosmadakis, G.; Cipollina, A.; Commare, U. La; Micale, G. Industrial Waste Heat: Estimation of the Technically Available Resource in the EU per Industrial Sector, Temperature Level and Country. *Appl. Therm. Eng.* **2018**, *138*, 207–216. https://doi.org/https://doi.org/10.1016/j.applthermaleng.2018.04.043.

(3) Ferrando-Villalba, P.; Lopeandía, A. F.; Alvarez, F. X.; Paul, B.; de Tomás, C.; Alonso, M. I.; Garriga, M.; Goñi, A. R.; Santiso, J.; Garcia, G.; et al. Tailoring Thermal Conductivity by Engineering Compositional Gradients in Si1−xGexsuperlattices. *Nano Res.* **2015**, *8* (9), 2833–2841. https://doi.org/10.1007/s12274-015-0788-9.

(4) Xu, B.; Verstraete, M. J. First Principles Explanation of the Positive Seebeck Coefficient of Lithium. *Phys. Rev. Lett.* **2014**, *112* (19), 196603. https://doi.org/10.1103/PhysRevLett.112.196603.

(5) Chen, G. P. *Nanoscale Energy Transport and Conversion : A Parallel Treatment of Electrons, Molecules, Phonons, and Photons*; Oxford ; New York : Oxford University Press, 2005., 2005.

(6) Rowe, D. M. *Thermoelectrics Handbook: Macro to Nano*; Taylor & Francis, 2005.

(7) Seebeck, T. J.; der Wissenschaften zu Berlin, D. A. *Ueber Den Magnetismus Der Galvanischen Kette*; 1822.

(8) Seebeck, T. J. Ueber Die Magnetische Polarisation Der Metalle Und Erze Durch Temperatur-Differenz. *Ann. Phys.* **1826**, *82* (2), 133–160. https://doi.org/10.1002/andp.18260820202.

(9) Peltier, J. C. Nouvelles Expéreinces Sur La Caloricité Des Courants Électriques. *Ann. Chim. Phys.* **1834**, *56*, 371–386.

(10) Rowe, D. M. *CRC Handbook of Thermoelectrics*; CRC-Press, 1995.

(11) Beekman, M.; Morelli, D. T.; Nolas, G. S. Better Thermoelectrics through Glass-like Crystals. *Nat. Mater.* **2015**, *14*, 1182.

(12) Liu, Z.; Mao, J.; Sui, J.; Ren, Z. High Thermoelectric Performance of α-MgAgSb

for Power Generation. *Energy Environ. Sci.* **2018**, *11* (1), 23–44. https://doi.org/10.1039/C7EE02504A.

(13) Goldsmid, H. J.; Douglas, R. W. The Use of Semiconductors in Thermoelectric Refrigeration. *Br. J. Appl. Phys.* **1954**, *5* (12), 458. https://doi.org/10.1088/0508-3443/5/12/513.

(14) Satterthwaite, C. B.; Ure, R. W. Electrical and Thermal Properties of ${\mathrm{Bi}}_{2}$ ${\mathrm{Te}}_{3}$. *Phys. Rev.* **1957**, *108* (5), 1164–1170. https://doi.org/10.1103/PhysRev.108.1164.

(15) Rosi, F. D.; Abeles, B.; Jensen, R. V. Materials for Thermoelectric Refrigeration. *J. Phys. Chem. Solids* **1959**, *10* (2), 191–200. https://doi.org/https://doi.org/10.1016/0022-3697(59)90074-5.

(16) Smith, G. E.; Wolfe, R. Thermoelectric Properties of Bismuth-Antimony Alloys. *J. Appl. Phys.* **1962**, *33* (3), 841–846. https://doi.org/10.1063/1.1777178.

(17) Lan, Y.; Minnich, A. J.; Chen, G.; Ren, Z. Enhancement of Thermoelectric Figure-of-Merit by a Bulk Nanostructuring Approach. *Adv. Funct. Mater.* **2010**, *20* (3), 357–376. https://doi.org/10.1002/adfm.200901512.

(18) Goldsmid, H. J. Bismuth Telluride and Its Alloys as Materials for Thermoelectric Generation. *Materials (Basel).* **2014**, *7* (4), 2577–2592. https://doi.org/10.3390/ma7042577.

(19) Zhu, T.; Hu, L.; Zhao, X.; He, J. New Insights into Intrinsic Point Defects in V2VI3 Thermoelectric Materials. *Adv. Sci.* **2016**, *3* (7), 1600004. https://doi.org/10.1002/advs.201600004.

(20) Rowe, D. M.; Fu, L. W.; Williams, S. G. K. Comments on the Thermoelectric Properties of Pressure-sintered Si0.8Ge0.2 Thermoelectric Alloys. *J. Appl. Phys.* **1993**, *73* (9), 4683–4685. https://doi.org/10.1063/1.352764.

(21) Lee, S.-M.; Cahill, D. G.; Venkatasubramanian, R. Thermal Conductivity of Si–Ge Superlattices. *Appl. Phys. Lett.* **1997**, *70* (22), 2957–2959. https://doi.org/10.1063/1.118755.

(22) Liu, C.-K.; Yu, C.-K.; Chien, H.-C.; Kuo, S.-L.; Hsu, C.-Y.; Dai, M.-J.; Luo, G.-L.; Huang, S.-C.; Huang, M.-J. Thermal Conductivity of Si/SiGe Superlattice Films. *J. Appl. Phys.* **2008**, *104* (11), 114301. https://doi.org/10.1063/1.3032602.

(23) Joshi, G.; Lee, H.; Lan, Y.; Wang, X.; Zhu, G.; Wang, D.; Gould, R. W.; Cuff, D. C.; Tang, M. Y.; Dresselhaus, M. S.; et al. Enhanced Thermoelectric Figure-of-Merit in Nanostructured p-Type Silicon Germanium Bulk Alloys. *Nano Lett.* **2008**,

8 (12), 4670–4674. https://doi.org/10.1021/nl8026795.

(24) Alvarez-Quintana, J.; Alvarez, X.; Rodriguez-Viejo, J.; Jou, D.; Lacharmoise, P. D.; Bernardi, A.; Goñi, A. R.; Alonso, M. I. Cross-Plane Thermal Conductivity Reduction of Vertically Uncorrelated Ge⁄Si Quantum Dot Superlattices. *Appl. Phys. Lett.* **2008**, *93* (1), 13112. https://doi.org/10.1063/1.2957038.

(25) Li, C. W.; Hong, J.; May, A. F.; Bansal, D.; Chi, S.; Hong, T.; Ehlers, G.; Delaire, O. Orbitally Driven Giant Phonon Anharmonicity in SnSe. *Nat. Phys.* **2015**, *11*, 1063.

(26) Zhao, L.-D.; Tan, G.; Hao, S.; He, J.; Pei, Y.; Chi, H.; Wang, H.; Gong, S.; Xu, H.; Dravid, V. P.; et al. Ultrahigh Power Factor and Thermoelectric Performance in Hole-Doped Single-Crystal SnSe. *Science (80-.).* **2016**, *351* (6269), 141–144. https://doi.org/10.1126/science.aad3749.

(27) Chiritescu, C.; Cahill, D. G.; Nguyen, N.; Johnson, D.; Bodapati, A.; Keblinski, P.; Zschack, P. Ultralow Thermal Conductivity in Disordered, Layered WSe2 Crystals. *Science (80-.).* **2007**, *315* (5810), 351–353. https://doi.org/10.1126/science.1136494.

(28) Li, D.; Zhao, H.; Li, S.; Wei, B.; Shuai, J.; Shi, C.; Xi, X.; Sun, P.; Meng, S.; Gu, L.; et al. Atomic Disorders Induced by Silver and Magnesium Ion Migrations Favor High Thermoelectric Performance in α-MgAgSb-Based Materials. *Adv. Funct. Mater.* **2015**, *25* (41), 6478–6488. https://doi.org/10.1002/adfm.201503022.

(29) Liu, Z.; Gao, W.; Meng, X.; Li, X.; Mao, J.; Wang, Y.; Shuai, J.; Cai, W.; Ren, Z.; Sui, J. Mechanical Properties of Nanostructured Thermoelectric Materials α-MgAgSb. *Scr. Mater.* **2017**, *127*, 72–75. https://doi.org/https://doi.org/10.1016/j.scriptamat.2016.08.037.

(30) Snyder, G. J.; Toberer, E. S. Complex Thermoelectric Materials. *Nat. Mater.* **2008**, *7* (2), 105–114.

(31) Zebarjadi, M.; Joshi, G.; Zhu, G.; Yu, B.; Minnich, A.; Lan, Y.; Wang, X.; Dresselhaus, M.; Ren, Z.; Chen, G. Power Factor Enhancement by Modulation Doping in Bulk Nanocomposites. *Nano Lett.* **2011**, *11* (6), 2225–2230. https://doi.org/10.1021/nl201206d.

(32) Zebarjadi, M.; Esfarjani, K.; Bian, Z.; Shakouri, A. Low-Temperature Thermoelectric Power Factor Enhancement by Controlling Nanoparticle Size Distribution. *Nano Lett.* **2011**, *11* (1), 225–230. https://doi.org/10.1021/nl103581z.

(33) Geballe, T. H.; Hull, G. W. Seebeck Effect in Silicon. *Phys. Rev.* **1955**, *98* (4), 940–947. https://doi.org/10.1103/PhysRev.98.940.

(34) Trzcinski, R.; Gmelin, E.; Queisser, H. J. Quenched Phonon Drag in Silicon Microcontacts. *Phys. Rev. Lett.* **1986**, *56* (10), 1086–1089. https://doi.org/10.1103/PhysRevLett.56.1086.

(35) Behnen, E. Quantitative Examination of the Thermoelectric Power of N-type Si in the Phonon Drag Regime. *J. Appl. Phys.* **1990**, *67* (1), 287–292. https://doi.org/10.1063/1.345250.

(36) Boukai, A. I.; Bunimovich, Y.; Tahir-Kheli, J.; Yu, J.-K.; Goddard III, W. A.; Heath, J. R. Silicon Nanowires as Efficient Thermoelectric Materials. *Nature* **2008**, *451*, 168.

(37) Zhou, J.; Liao, B.; Qiu, B.; Huberman, S.; Esfarjani, K.; Dresselhaus, M. S.; Chen, G. Ab Initio Optimization of Phonon Drag Effect for Lower-Temperature Thermoelectric Energy Conversion. *Proc. Natl. Acad. Sci.* **2015**, *112* (48), 14777–14782. https://doi.org/10.1073/pnas.1512328112.

(38) Ioffe, A. F. *Physics of Semiconductors*; New York, 1960.

(39) Uher, C. *Materials Aspect of Thermoelectricity*; CRC Press, 2016.

(40) Hicks, L. D.; Dresselhaus, M. S. Effect of Quantum-Well Structures on the Thermoelectric Figure of Merit. *Phys. Rev. B* **1993**, *47* (19), 12727–12731. https://doi.org/10.1103/PhysRevB.47.12727.

(41) Lin, Y.-M.; Dresselhaus, M. S. Thermoelectric Properties of Superlattice Nanowires. *Phys. Rev. B* **2003**, *68* (7), 75304. https://doi.org/10.1103/PhysRevB.68.075304.

(42) Bahk, J.-H.; Shakouri, A. Enhancing the Thermoelectric Figure of Merit through the Reduction of Bipolar Thermal Conductivity with Heterostructure Barriers. *Appl. Phys. Lett.* **2014**, *105* (5), 52106. https://doi.org/10.1063/1.4892653.

(43) Minnich, A. J.; Dresselhaus, M. S.; Ren, Z. F.; Chen, G. Bulk Nanostructured Thermoelectric Materials: Current Research and Future Prospects. *Energy Environ. Sci.* **2009**, *2* (5), 466–479. https://doi.org/10.1039/B822664B.

(44) Hu, D.; Liu, Q.; Tisdale, J.; Lei, T.; Pei, J.; Wang, H.; Urbas, A.; Hu, B. Seebeck Effects in N-Type and P-Type Polymers Driven Simultaneously by Surface Polarization and Entropy Differences Based on Conductor/Polymer/Conductor Thin-Film Devices. *ACS Nano* **2015**, *9* (5), 5208–5213. https://doi.org/10.1021/acsnano.5b00589.

(45) Burzo, M. G.; Komarov, P. L.; Raad, P. E. A Study of the Effect of Surface Metalization on the Thermal Conductivity Measurements by the Transient Thermo-Reflectance Method. 2002, pp 179–182.

(46) Schmidt, A. J.; Cheaito, R.; Chiesa, M. A Frequency-Domain Thermoreflectance Method for the Characterization of Thermal Properties. *Rev. Sci. Instrum.* **2009**, *80* (9), 94901. https://doi.org/10.1063/1.3212673.

(47) Reparaz, J. S.; Chavez-Angel, E.; Wagner, M. R.; Graczykowski, B.; Gomis-Bresco, J.; Alzina, F.; Sotomayor Torres, C. M. A Novel Contactless Technique for Thermal Field Mapping and Thermal Conductivity Determination: Two-Laser Raman Thermometry. *Rev. Sci. Instrum.* **2014**, *85* (3), 34901. https://doi.org/10.1063/1.4867166.

(48) Goodson, K. E.; Käding, O. W.; Rösler, M.; Zachai, R. Experimental Investigation of Thermal Conduction Normal to Diamond-silicon Boundaries. *J. Appl. Phys.* **1995**, *77* (4), 1385–1392. https://doi.org/10.1063/1.358950.

(49) *Thermal Conductivity - Theory, Properties, and Applications*; Tritt, T. M., Ed.; Physics of Solids and Liquids; Springer US, 2004. https://doi.org/10.1007/b136496.

(50) Sikora, A.; Ftouni, H.; Richard, J.; Hébert, C.; Eon, D.; Omnès, F.; Bourgeois, O. Highly Sensitive Thermal Conductivity Measurements of Suspended Membranes (SiN and Diamond) Using a 3ω-Völklein Method. *Rev. Sci. Instrum.* **2012**, *83* (5), 54902. https://doi.org/10.1063/1.4704086.

(51) Cahill, D. G. Thermal Conductivity Measurement from 30 to 750 K: The 3ω Method. *Rev. Sci. Instrum.* **1990**, *61* (2), 802–808. https://doi.org/10.1063/1.1141498.

(52) Cahill, D. G.; Katiyar, M.; Abelson, J. R. Thermal Conductivity of A-Si:H Thin Films. *Phys. Rev. B* **1994**, *50* (9), 6077–6081. https://doi.org/10.1103/PhysRevB.50.6077.

(53) Tong, T.; Majumdar, A. Reexamining the 3-Omega Technique for Thin Film Thermal Characterization. *Rev. Sci. Instrum.* **2006**, *77* (10), 104902. https://doi.org/10.1063/1.2349601.

(54) Volklein, F.; Starz, T. Thermal Conductivity of Thin Films-Experimental Methods and Theoretical Interpretation. In *XVI ICT '97. Proceedings ICT'97. 16th International Conference on Thermoelectrics (Cat. No.97TH8291)*; 1997; pp 711–718. https://doi.org/10.1109/ICT.1997.667630.

(55) Ferrando-Villalba, P.; Takegami, D.; Abad, L.; Ràfols-Ribé, J.; Lopeandía, A.; Garcia, G.; Rodríguez-Viejo, J. Growth Monitoring with Sub-Monolayer Sensitivity via Real Time Thermal Conductance Measurements. **2018**.

(56) Tauc, J. The Thermal Photo-Electric Phenomenon in Semi-Conductors. *Cechoslov. Fiz. Z.* **1955**, *5* (4), 528–535. https://doi.org/10.1007/BF01687219.

(57) PAUW, L. J. V. A. N. D. E. R.; POLDER, D. XXII. The Photo-Thermoelectric Phenomenon in Semiconductors†. *J. Electron. Control* **1956**, *2* (3), 239–240. https://doi.org/10.1080/00207215608937026.

(58) Harper, J. G.; Matthews, H. E.; Bube, R. H. Photothermoelectric Effects in Semiconductors: N- and P-Type Silicon. *J. Appl. Phys.* **1970**, *41* (2), 765–770. https://doi.org/10.1063/1.1658745.

(59) Kwok, H.; Bube, R. H. Another Look at the Anomalous Photothermoelectric Effect in P-Type Silicon. *J. Appl. Phys.* **1970**, *41* (12), 5026–5027. https://doi.org/10.1063/1.1658582.

(60) Mondal, P. S.; Okazaki, R.; Taniguchi, H.; Terasaki, I. Photo-Seebeck Effect in Tetragonal PbO Single Crystals. *J. Appl. Phys.* **2013**, *114* (17), 173710. https://doi.org/10.1063/1.4829460.

(61) Terasaki, I.; Okazaki, R.; Mondal, P. S.; Hsieh, Y.-C. Trials for Oxide Photo-Thermoelectrics. *Mater. Renew. Sustain. Energy* **2014**, *3* (3), 29. https://doi.org/10.1007/s40243-014-0029-2.

(62) Lv, Y.; Chen, J.; Zheng, R.-K.; Song, J.; Zhang, T.; Li, X.; Shi, X.; Chen, L. Photo-Induced Enhancement of the Power Factor of Cu2S Thermoelectric Films. *Sci. Rep.* **2015**, *5*, 16291.

(63) Xu, L.; Liu, Y.; Garrett, M. P.; Chen, B.; Hu, B. Enhancing Seebeck Effects by Using Excited States in Organic Semiconducting Polymer MEH-PPV Based on Multilayer Electrode/Polymer/Electrode Thin-Film Structure. *J. Phys. Chem. C* **2013**, *117* (20), 10264–10269. https://doi.org/10.1021/jp4000957.

(64) Wu, P.; Xiong, Y.; Sun, L.; Xie, G.; Xu, L. Enhancing Thermoelectric Performance of the CH3NH3PbI3 Polycrystalline Thin Films by Using the Excited State on Photoexcitation. *Org. Electron.* **2018**, *55*, 90–96. https://doi.org/https://doi.org/10.1016/j.orgel.2018.01.014.

(65) Lu, X.; Jiang, P.; Bao, X. Phonon-Enhanced Photothermoelectric Effect in SrTiO(3) Ultra-Broadband Photodetector. *Nat. Commun.* **2019**, *10* (1), 138. https://doi.org/10.1038/s41467-018-07860-0.

(66) Yan, Y.; Liao, Z.-M.; Ke, X.; Van Tendeloo, G.; Wang, Q.; Sun, D.; Yao, W.; Zhou, S.; Zhang, L.; Wu, H.-C.; et al. Topological Surface State Enhanced Photothermoelectric Effect in Bi2Se3 Nanoribbons. *Nano Lett.* **2014**, *14* (8), 4389–4394. https://doi.org/10.1021/nl501276e.

(67) Perez-Marín, A. P.; Lopeandía, A. F.; Abad, L.; Ferrando-Villaba, P.; Garcia, G.; Lopez, A. M.; Muñoz-Pascual, F. X.; Rodríguez-Viejo, J. Micropower Thermoelectric Generator from Thin Si Membranes. *Nano Energy* **2014**, *4*, 73–80. https://doi.org/https://doi.org/10.1016/j.nanoen.2013.12.007.

(68) Ferrando-Villalba, P.; Pérez-Marín, A. P.; Abad, L.; Dalkiranis, G. G.; Lopeandia, A. F.; Garcia, G.; Rodriguez-Viejo, J. Measuring Device and Material ZT in a Thin-Film Si-Based Thermoelectric Microgenerator. *Nanomaterials* **2019**, *9* (4). https://doi.org/10.3390/nano9040653.

(69) Neogi, S.; Reparaz, J. S.; Pereira, L. F. C.; Graczykowski, B.; Wagner, M. R.; Sledzinska, M.; Shchepetov, A.; Prunnila, M.; Ahopelto, J.; Sotomayor-Torres, C. M.; et al. Tuning Thermal Transport in Ultrathin Silicon Membranes by Surface Nanoscale Engineering. *ACS Nano* **2015**, *9* (4), 3820–3828. https://doi.org/10.1021/nn506792d.

(70) Ferrando-Villalba, P.; Lopeandia, A. F.; Abad, L.; Llobet, J.; Molina-Ruiz, M.; Garcia, G.; Gerbolès, M.; Alvarez, F. X.; Goñi, A. R.; Muñoz-Pascual, F. J.; et al. In-Plane Thermal Conductivity of Sub-20 Nm Thick Suspended Mono-Crystalline Si Layers. *Nanotechnology* **2014**, *25* (18), 185402. https://doi.org/10.1088/0957-4484/25/18/185402.

(71) Li, D.; Wu, Y.; Kim, P.; Shi, L.; Yang, P.; Majumdar, A. Thermal Conductivity of Individual Silicon Nanowires. *Appl. Phys. Lett.* **2003**, *83* (14), 2934–2936. https://doi.org/10.1063/1.1616981.

(72) Cahill, D. G.; Braun, P. V; Chen, G.; Clarke, D. R.; Fan, S.; Goodson, K. E.; Keblinski, P.; King, W. P.; Mahan, G. D.; Majumdar, A.; et al. Nanoscale Thermal Transport. II. 2003–2012. *Appl. Phys. Rev.* **2014**, *1* (1), 11305. https://doi.org/10.1063/1.4832615.

(73) Malhotra, A.; Maldovan, M. Impact of Phonon Surface Scattering on Thermal Energy Distribution of Si and SiGe Nanowires. *Sci. Rep.* **2016**, *6*, 25818.

(74) Hochbaum, A. I.; Chen, R.; Delgado, R. D.; Liang, W.; Garnett, E. C.; Najarian, M.; Majumdar, A.; Yang, P. Enhanced Thermoelectric Performance of Rough Silicon Nanowires. *Nature* **2008**, *451*, 163.

(75) Dennis, P. J.; Welch, E. F.; Alarie, J. P.; Ramsey, J. M.; Jorgenson, J. W. Development of a Photothermal Absorbance Detector for Use with Microfluidic Devices. *Anal. Chem.* **2010**, *82* (10), 4063–4071. https://doi.org/10.1021/ac902975r.

(76) Patil, V.; Capone, A.; Strauf, S.; Yang, E.-H. Improved Photoresponse with Enhanced Photoelectric Contribution in Fully Suspended Graphene Photodetectors. *Sci. Rep.* **2013**, *3*, 2791.

(77) García de Arquer, F. P.; Mihi, A.; Konstantatos, G. Large-Area Plasmonic-Crystal–Hot-Electron-Based Photodetectors. *ACS Photonics* **2015**, *2* (7), 950–957. https://doi.org/10.1021/acsphotonics.5b00149.

(78) Chen, G. Y.; Wu, X.; Liu, X.; Lancaster, D. G.; Monro, T. M.; Xu, H. Photodetector Based on Vernier-Enhanced Fabry-Perot Interferometers with a Photo-Thermal Coating. *Sci. Rep.* **2017**, *7*, 41895.

(79) Dillner, U.; Kessler, E.; Meyer, H.-G. Figures of Merit of Thermoelectric and Bolometric Thermal Radiation Sensors. *J. Sensors Sens. Syst.* **2013**, *2* (1), 85–94. https://doi.org/10.5194/jsss-2-85-2013.

(80) Wang, K.; Xue, C.; Liang, T.; Jiao, B.; Zhang, W.; Chen, D.; Xiong, J. Thermopile Infrared Detector with Detectivity Greater Than 108 CmHz(1/2)/W. *J. Infrared, Millimeter, Terahertz Waves* **2010**, *31* (7), 810–820. https://doi.org/10.1007/s10762-010-9635-y.

(81) Zhou, H.; Kropelnicki, P.; Tsai, J. M.; Lee, C. Development of a Thermopile Infrared Sensor Using Stacked Double Polycrystalline Silicon Layers Based on the {CMOS} Process. *J. Micromechanics Microengineering* **2013**, *23* (6), 65026. https://doi.org/10.1088/0960-1317/23/6/065026.

(82) Salleh, F.; Asai, K.; Ishida, A.; Ikeda, H. Seebeck Coefficient of Ultrathin Silicon-on-Insulator Layers. *Appl. Phys. Express* **2009**, *2*, 71203. https://doi.org/10.1143/apex.2.071203.

(83) Fano, U. Effects of Configuration Interaction on Intensities and Phase Shifts. *Phys. Rev.* **1961**, *124* (6), 1866–1878. https://doi.org/10.1103/PhysRev.124.1866.

(84) Magidson, V.; Beserman, R. Fano-Type Interference in the Raman Spectrum of Photoexcited Si. *Phys. Rev. B* **2002**, *66* (19), 195206. https://doi.org/10.1103/PhysRevB.66.195206.

(85) Volodin, V. A.; Efremov, M. D.; Cherkov, A. G. Raman Investigation of the Electron-Phonon Interaction in n-Type Silicon Nanocrystals. *Phys. Solid State*

2008, *50* (5), 962–965. https://doi.org/10.1134/S1063783408050260.

(86) Geist, J.; Zalewski, E. F. The Quantum Yield of Silicon in the Visible. *Appl. Phys. Lett.* **1979**, *35* (7), 503–505. https://doi.org/10.1063/1.91187.

(87) Green, M. A. Self-Consistent Optical Parameters of Intrinsic Silicon at 300K Including Temperature Coefficients. *Sol. Energy Mater. Sol. Cells* **2008**, *92* (11), 1305–1310. https://doi.org/https://doi.org/10.1016/j.solmat.2008.06.009.

(88) Li, S. S. Excess Carrier Phenomenon in Semiconductors. In *Semiconductor Physical Electronics*; Li, S. S., Ed.; Springer New York: New York, NY, 2006; pp 134–170. https://doi.org/10.1007/0-387-37766-2_6.

(89) Kirkham, M. J.; dos Santos, A. M.; Rawn, C. J.; Lara-Curzio, E.; Sharp, J. W.; Thompson, A. J. Abinitio Determination of Crystal Structures of the Thermoelectric Material MgAgSb. *Phys. Rev. B* **2012**, *85* (14), 144120. https://doi.org/10.1103/PhysRevB.85.144120.

(90) Ying, P.; Liu, X.; Fu, C.; Yue, X.; Xie, H.; Zhao, X.; Zhang, W.; Zhu, T. High Performance α-MgAgSb Thermoelectric Materials for Low Temperature Power Generation. *Chem. Mater.* **2015**, *27* (3), 909–913. https://doi.org/10.1021/cm5041826.

(91) Zhao, H.; Sui, J.; Tang, Z.; Lan, Y.; Jie, Q.; Kraemer, D.; McEnaney, K.; Guloy, A.; Chen, G.; Ren, Z. High Thermoelectric Performance of MgAgSb-Based Materials. *Nano Energy* **2014**, *7*, 97–103. https://doi.org/https://doi.org/10.1016/j.nanoen.2014.04.012.

(92) Liu, Z.; Geng, H.; Mao, J.; Shuai, J.; He, R.; Wang, C.; Cai, W.; Sui, J.; Ren, Z. Understanding and Manipulating the Intrinsic Point Defect in α-MgAgSb for Higher Thermoelectric Performance. *J. Mater. Chem. A* **2016**, *4* (43), 16834–16840. https://doi.org/10.1039/C6TA06832D.

(93) Zheng, Y.; Liu, C.; Miao, L.; Li, C.; Huang, R.; Gao, J.; Wang, X.; Chen, J.; Zhou, Y.; Nishibori, E. Extraordinary Thermoelectric Performance in MgAgSb Alloy with Ultralow Thermal Conductivity. *Nano Energy* **2019**, *59*, 311–320. https://doi.org/https://doi.org/10.1016/j.nanoen.2019.02.045.

(94) Lei, J.; Zhang, D.; Guan, W.; Cheng, Z.; Wang, C.; Wang, Y. Engineering Electrical Transport in α-MgAgSb to Realize High Performances near Room Temperature. *Phys. Chem. Chem. Phys.* **2018**, *20* (24), 16729–16735. https://doi.org/10.1039/C8CP02186D.

(95) Dutta, S.; Narayan, K. S. Gate-Voltage Control of Optically- Induced Charges and

Memory Effects in Polymer Field-Effect Transistors. *Adv. Mater.* **2004**, *16* (23-24), 2151–2155. https://doi.org/10.1002/adma.200400084.

(96) Kim, Y. H.; Sachse, C.; Machala, M. L.; May, C.; Müller-Meskamp, L.; Leo, K. Highly Conductive PEDOT:PSS Electrode with Optimized Solvent and Thermal Post-Treatment for ITO-Free Organic Solar Cells. *Adv. Funct. Mater.* **2011**, *21* (6), 1076–1081. https://doi.org/10.1002/adfm.201002290.

(97) Bubnova, O.; Crispin, X. Towards Polymer-Based Organic Thermoelectric Generators. *Energy Environ. Sci.* **2012**, *5* (11), 9345–9362. https://doi.org/10.1039/C2EE22777K.

(98) Jäckle, S.; Liebhaber, M.; Gersmann, C.; Mews, M.; Jäger, K.; Christiansen, S.; Lips, K. Potential of PEDOT:PSS as a Hole Selective Front Contact for Silicon Heterojunction Solar Cells. *Sci. Rep.* **2017**, *7* (1), 2170. https://doi.org/10.1038/s41598-017-01946-3.

(99) Zhou, L.; Mao, J.; Ren, Y.; Han, S.-T.; Roy, V. A. L.; Zhou, Y. Recent Advances of Flexible Data Storage Devices Based on Organic Nanoscaled Materials. *Small* **2018**, *14* (10), 1703126. https://doi.org/10.1002/smll.201703126.

(100) Bahk, J.-H.; Fang, H.; Yazawa, K.; Shakouri, A. Flexible Thermoelectric Materials and Device Optimization for Wearable Energy Harvesting. *J. Mater. Chem. C* **2015**, *3* (40), 10362–10374. https://doi.org/10.1039/C5TC01644D.

(101) Kishore, R. A.; Nozariasbmarz, A.; Poudel, B.; Sanghadasa, M.; Priya, S. Ultra-High Performance Wearable Thermoelectric Coolers with Less Materials. *Nat. Commun.* **2019**, *10* (1), 1765. https://doi.org/10.1038/s41467-019-09707-8.

(102) Shi, H.; Liu, C.; Jiang, Q.; Xu, J. Effective Approaches to Improve the Electrical Conductivity of PEDOT:PSS: A Review. *Adv. Electron. Mater.* **2015**, *1* (4), 1500017. https://doi.org/10.1002/aelm.201500017.

(103) Kim, G.-H.; Shao, L.; Zhang, K.; Pipe, K. P. Engineered Doping of Organic Semiconductors for Enhanced Thermoelectric Efficiency. *Nat. Mater.* **2013**, *12*, 719.

(104) Wang, X.; Wang, H.; Liu, B. Carbon Nanotube-Based Organic Thermoelectric Materials for Energy Harvesting. *Polymers (Basel).* **2018**, *10* (11). https://doi.org/10.3390/polym10111196.

(105) Wang, Q.; Yao, Q.; Chang, J.; Chen, L. Enhanced Thermoelectric Properties of CNT/PANI Composite Nanofibers by Highly Orienting the Arrangement of Polymer Chains. *J. Mater. Chem.* **2012**, *22* (34), 17612–17618.

https://doi.org/10.1039/C2JM32750C.

(106) Kato, K.; Hagino, H.; Miyazaki, K. Fabrication of Bismuth Telluride Thermoelectric Films Containing Conductive Polymers Using a Printing Method. *J. Electron. Mater.* **2013**, *42* (7), 1313–1318. https://doi.org/10.1007/s11664-012-2420-z.

(107) Yao, Q.; Chen, L.; Zhang, W.; Liufu, S.; Chen, X. Enhanced Thermoelectric Performance of Single-Walled Carbon Nanotubes/Polyaniline Hybrid Nanocomposites. *ACS Nano* **2010**, *4* (4), 2445–2451. https://doi.org/10.1021/nn1002562.

(108) Lu, Y.; Song, Y.; Wang, F. Thermoelectric Properties of Graphene Nanosheets-Modified Polyaniline Hybrid Nanocomposites by an in Situ Chemical Polymerization. *Mater. Chem. Phys.* **2013**, *138* (1), 238–244. https://doi.org/https://doi.org/10.1016/j.matchemphys.2012.11.052.

(109) Zhang, B.; Sun, J.; Katz, H. E.; Fang, F.; Opila, R. L. Promising Thermoelectric Properties of Commercial PEDOT:PSS Materials and Their Bi2Te3 Powder Composites. *ACS Appl. Mater. Interfaces* **2010**, *2* (11), 3170–3178. https://doi.org/10.1021/am100654p.

(110) He, M.; Ge, J.; Lin, Z.; Feng, X.; Wang, X.; Lu, H.; Yang, Y.; Qiu, F. Thermopower Enhancement in Conducting Polymer Nanocomposites via Carrier Energy Scattering at the Organic–Inorganic Semiconductor Interface. *Energy Environ. Sci.* **2012**, *5* (8), 8351–8358. https://doi.org/10.1039/C2EE21803H.

(111) Yee, S. K.; Coates, N. E.; Majumdar, A.; Urban, J. J.; Segalman, R. A. Thermoelectric Power Factor Optimization in PEDOT:PSS Tellurium Nanowire Hybrid Composites. *Phys. Chem. Chem. Phys.* **2013**, *15* (11), 4024–4032. https://doi.org/10.1039/C3CP44558E.

(112) Coates, N. E.; Yee, S. K.; McCulloch, B.; See, K. C.; Majumdar, A.; Segalman, R. A.; Urban, J. J. Effect of Interfacial Properties on Polymer–Nanocrystal Thermoelectric Transport. *Adv. Mater.* **2013**, *25* (11), 1629–1633. https://doi.org/10.1002/adma.201203915.

(113) Singh, V.; Bougher, T. L.; Weathers, A.; Cai, Y.; Bi, K.; Pettes, M. T.; McMenamin, S. A.; Lv, W.; Resler, D. P.; Gattuso, T. R.; et al. High Thermal Conductivity of Chain-Oriented Amorphous Polythiophene. *Nat. Nanotechnol.* **2014**, *9*, 384.

(114) Liu, J.; Wang, X.; Li, D.; Coates, N. E.; Segalman, R. A.; Cahill, D. G. Thermal

Conductivity and Elastic Constants of PEDOT:PSS with High Electrical Conductivity. *Macromolecules* **2015**, *48* (3), 585–591. https://doi.org/10.1021/ma502099t.

(115) Beretta, D.; Barker, A. J.; Maqueira-Albo, I.; Calloni, A.; Bussetti, G.; Dell'Erba, G.; Luzio, A.; Duò, L.; Petrozza, A.; Lanzani, G.; et al. Thermoelectric Properties of Highly Conductive Poly(3,4-Ethylenedioxythiophene) Polystyrene Sulfonate Printed Thin Films. *ACS Appl. Mater. Interfaces* **2017**, *9* (21), 18151–18160. https://doi.org/10.1021/acsami.7b04533.

(116) Kirchmeyer, S.; Reuter, K. Scientific Importance{,} Properties and Growing Applications of Poly(3{,}4-Ethylenedioxythiophene). *J. Mater. Chem.* **2005**, *15* (21), 2077–2088. https://doi.org/10.1039/B417803N.

(117) Yan, H.; Okuzaki, H. Effect of Solvent on PEDOT/PSS Nanometer-Scaled Thin Films: XPS and STEM/AFM Studies. *Synth. Met.* **2009**, *159* (21), 2225–2228. https://doi.org/https://doi.org/10.1016/j.synthmet.2009.07.032.

(118) Pathak, C. S.; Singh, J. P.; Singh, R. Effect of Dimethyl Sulfoxide on the Electrical Properties of PEDOT:PSS/n-Si Heterojunction Diodes. *Curr. Appl. Phys.* **2015**, *15* (4), 528–534. https://doi.org/https://doi.org/10.1016/j.cap.2015.01.020.

(119) Culebras, M.; Gómez, C. M.; Cantarero, A. Review on Polymers for Thermoelectric Applications. *Materials (Basel).* **2014**, *7* (9), 6701–6732. https://doi.org/10.3390/ma7096701.

(120) Yue, R.; Xu, J. Poly(3,4-Ethylenedioxythiophene) as Promising Organic Thermoelectric Materials: A Mini-Review. *Synth. Met.* **2012**, *162* (11), 912–917. https://doi.org/https://doi.org/10.1016/j.synthmet.2012.04.005.

(121) Dimitriev, O. P.; Grinko, D. A.; Noskov, Y. V.; Ogurtsov, N. A.; Pud, A. A. PEDOT:PSS Films—Effect of Organic Solvent Additives and Annealing on the Film Conductivity. *Synth. Met.* **2009**, *159* (21), 2237–2239. https://doi.org/https://doi.org/10.1016/j.synthmet.2009.08.022.

(122) Chang, K.; Jeng, M.; Yang, C.; Chou, Y.; Wu, S.; Thomas, M. A. The Thermoelectric Performance of Poly (3 , 4-Ethylenedi- Oxythiophene)/ Poly (4-Styrenesulfonate) Thin Films. *J. Electron. Mater.* **2009**, *38* (7), 1182–1188. https://doi.org/10.1007/s11664-009-0821-4.

(123) Luo, J.; Billep, D.; Waechtler, T.; Otto, T.; Toader, M.; Gordan, O.; Sheremet, E.; Martin, J.; Hietschold, M.; Zahn, D. R. T.; et al. Enhancement of the Thermoelectric Properties of PEDOT:PSS Thin Films by Post-Treatment. *J.*

Mater. Chem. A **2013**, *1* (26), 7576–7583. https://doi.org/10.1039/C3TA11209H.

(124) Wei, Q.; Uehara, C.; Mukaida, M.; Kirihara, K.; Ishida, T. Measurement of In-Plane Thermal Conductivity in Polymer Films. *AIP Adv.* **2016**, *6* (4), 45315. https://doi.org/10.1063/1.4948447.

(125) Greppmair, A.; Stoib, B.; Saxena, N.; Gerstberger, C.; Müller-Buschbaum, P.; Stutzmann, M.; Brandt, M. S. Measurement of the In-Plane Thermal Conductivity by Steady-State Infrared Thermography. *Rev. Sci. Instrum.* **2017**, *88* (4), 44903. https://doi.org/10.1063/1.4979564.

(126) Zhu, Z.; Liu, C.; Jiang, F.; Xu, J.; Liu, E. Effective Treatment Methods on PEDOT:PSS to Enhance Its Thermoelectric Performance. *Synth. Met.* **2017**, *225*, 31–40. https://doi.org/https://doi.org/10.1016/j.synthmet.2016.11.011.

(127) Mengistie, D. A.; Chen, C.-H.; Boopathi, K. M.; Pranoto, F. W.; Li, L.-J.; Chu, C.-W. Enhanced Thermoelectric Performance of PEDOT:PSS Flexible Bulky Papers by Treatment with Secondary Dopants. *ACS Appl. Mater. Interfaces* **2015**, *7* (1), 94–100. https://doi.org/10.1021/am507032e.

(128) Ràfols-Ribé, J.; Dettori, R.; Ferrando-Villalba, P.; Gonzalez-Silveira, M.; Abad, L.; Lopeand\'\ia, A. F.; Colombo, L.; Rodr\'\iguez-Viejo, J. Evidence of Thermal Transport Anisotropy in Stable Glasses of Vapor Deposited Organic Molecules. *Phys. Rev. Mater.* **2018**, *2* (3), 35603. https://doi.org/10.1103/PhysRevMaterials.2.035603.

(129) Alemu Mengistie, D.; Wang, P.-C.; Chu, C.-W. Effect of Molecular Weight of Additives on the Conductivity of PEDOT:PSS and Efficiency for ITO-Free Organic Solar Cells. *J. Mater. Chem. A* **2013**, *1* (34), 9907–9915. https://doi.org/10.1039/C3TA11726J.

(130) van de Ruit, K.; Katsouras, I.; Bollen, D.; van Mol, T.; Janssen, R. A. J.; de Leeuw, D. M.; Kemerink, M. The Curious Out-of-Plane Conductivity of PEDOT:PSS. *Adv. Funct. Mater.* **2013**, *23* (46), 5787–5793. https://doi.org/10.1002/adfm.201301175.

(131) Wei, Q.; Mukaida, M.; Naitoh, Y.; Ishida, T. Morphological Change and Mobility Enhancement in PEDOT:PSS by Adding Co-Solvents. *Adv. Mater.* **2013**, *25* (20), 2831–2836. https://doi.org/10.1002/adma.201205158.

(132) Palumbiny, C. M.; Heller, C.; Schaffer, C. J.; Körstgens, V.; Santoro, G.; Roth, S. V; Müller-Buschbaum, P. Molecular Reorientation and Structural Changes in Cosolvent-Treated Highly Conductive PEDOT:PSS Electrodes for Flexible

Indium Tin Oxide-Free Organic Electronics. *J. Phys. Chem. C* **2014**, *118* (25), 13598–13606. https://doi.org/10.1021/jp501540y.

(133) JIANG, F.-X.; XU Jing-Kun; LU Bao-Yang; XIE Yu; HUANG Rong-Jin; LI Lai-Feng. Thermoelectric Performance of Poly(3,4-Ethylenedioxythiophene):Poly(Styrenesulfonate). *Chinese Phys. Lett.* **2008**, *25* (6), 2202–2205.

10. List of Publications

- Ferrando-Villalba, P.; D'Ortenzi, L.; Dalkiranis, G. G.; Cara, E.; Lopeandia, A. F.; Abad, L.; Rurali, R.; Cartoixà, X.; De Leo, N.; Saghi, Z.; et al. Impact of Pore Anisotropy on the Thermal Conductivity of Porous Si Nanowires. *Sci. Rep.* **2018**, *8* (1). https://doi.org/10.1038/s41598-018-30223-0.
- Gonçalves Dalkiranis, G.; Ferrando-Villalba, P.; Lopeandia-Fernández, A.; Abad-Muñoz, L.; Rodríguez-Viejo, J. Thermoelectric Photosensor Based on Ultrathin Single-Crystalline Si Films †. *Sensors* **2019**, *19* (6). https://doi.org/10.3390/s19061427.
- Ferrando-Villalba, P.; Pérez-Marín, A. P.; Abad, L.; Dalkiranis, G. G.; Lopeandia, A. F.; Garcia, G.; Rodriguez-Viejo, J. Measuring Device and Material ZT in a Thin-Film Si-Based Thermoelectric Microgenerator. *Nanomaterials* **2019**, *9* (4). https://doi.org/10.3390/nano9040653.